The Design and Performance of Muon Scattering Tomography Reconstruction Algorithms for Applications in Nuclear Waste Identification

Ahmad F. ALRHELI

Supervisor: **Prof. Lee Thompson**

Department of Physics and Astronomy

The University of Sheffield

A thesis submitted in partial fulfilment of the requirements for the degree of Doctor of Philosophy in Physics

August 3, 2023

"Since when have you enslaved people, when their mothers gave birth to them as free human beings?"
Ummar ibn Al-Kattab

Declaration

I hereby declare that the contents of this thesis is my own work, except where specific reference is made to the work of others, the contents of this thesis are original and have not been submitted in whole or in part for consideration for any other degree, qualification or academic reward in this, or any other university.

Chapter 3 describes the CHANCE muon scattering tomography system. This system was built in collaboration with CHANCE members from the University of Sheffield, University of Bristol and Warsaw University of Technology. The CHANCE members from the universities mentioned above are: Lee Thompson, Jaap Velthuis, Daniel Kikoła, Patrick Stowell, Anna Kopp, Micheal Weekes, Mohammed Mhaidra, Ahmad Alrheli. Then, Domnic Barker (the university of Sheffield) and Chiara De Sio (University of Bristol) joined CHANCE project and contributed in the operation of the system. I declare that all the results presented in this thesis are based on my own work using Monte Carlo simulations of the CHANCE muon detector in Bristol and do not use any empirical data from the detector system. I declare that the development of the Hybrid (HB) and the High Angle Statistics Reconstruction (H-ASR) algorithms presented in this thesis are my own work.

Ahmad Alrheli
January 2023

Acknowledgements

First and foremost, I would like to express my gratitude to my supervisor Professor Lee Thompson for his endless support, guidance, effort, and time throughout the development and writing of this thesis. Professor Lee is always around and happy to answer my endless questions with a great amount of patience and respect throughout all. Lee has consistently encouraged me and presented new ideas to investigate in the research field. Without Lee, as a "kind person", and as a research supervisor, this thesis would not have been possible. I would like to thank my personal tutor Dr. Rhoda Hawkins for her supports on answering many enquires during my PhD journey. I also would like to thank all the professional staffs in the Hicks building for providing me supports and helps during my work in the Hicks building.

I also would like to thank Dr.Patrick Stowell for his endless support and patience throughout the early years of my Ph.D. journey. I have had the greatest honor and pleasure of working with Patrick in the laboratory and also during traveling down to Bristol for the decommissioning process of the muon detector. A special thank you goes to my colleague Michael weekes, I have had a great time working alongside the last few years. Michael is a great colleague as we always exchange knowledge and exciting new concepts about muon tomography. Special and many thanks go to the current and past colleagues of the D36a office: Celeste Pidcott, Jordan McElwee, Samuel Fargher, Matthew Thiesse, Andrew Scarff, Liam O'Sullivan, Sam Jenkins, and Nicola McConkey. It has been a pleasure to work with these people who helped make my Ph.D. journey enjoyable. I also would like to thank people in the CHANCE project across all Europe, especially Jaap Velthuis, Daniel Kikola and Holger Tietze-Jaensch, for all their helps during regular meetings and assemblies.

Most of all, I would like to express deep gratitude to my amazing wife, Fiazah Alrehaili, for her endless and unconditional support and unbelievable patience. I would like to say that I am very lucky to be your husband. I also extend my gratitude to my mother, Aesha Salem, and my father, Faraj Lafi for providing unconditional support. I

also would like to thank my brothers, sisters, nieces, nephews, and all my friends back in Saudi Arabia. Finally, a great thank goes to my sponsor "Taibah University" and Saudi Arabia Cultural Bureau, and the Royal Embassy of Saudi Arabia in London, for their helps during my stay in the united kingdom.

Abstract

Characterisation of nuclear waste in the current time is well organised and each radioactive waste is disposed of or stored in an interim facility depending on the type of the waste. Characterised nuclear waste is expected to be documented and kept for records to be checked regularly according to the IAEA regulations. However, uncharacteristic nuclear waste is still found, especially, old nuclear waste that was stored at a time when documentation of the materials was not required. Moreover, some historical nuclear waste might contain heterogeneous contents of different types of radioactive materials. This dictates an efficient technique to resolve these issues by characterising disposed and/or stored unrecorded nuclear waste. Such techniques to investigate these nuclear waste drums without opening them are valuable to reduce the cost and the hazard of being contacted with unidentified radioactive materials. Muon Scattering Tomography (MST) technique has significantly increased in importance as a non-destructive imaging method of nuclear waste. In the past few decades, a significant amount of research has shown the efficacy of MST as an imaging method. However, there are still several areas that require further development in MST technique to contribute to nuclear waste management. An efficient imaging algorithm is requested to image and identify nuclear waste in a few hours. This thesis shows a method of optimising imaging performances of the common algorithms. This thesis shows that dividing the volume of interest by rectangular voxels with a side length of 10 mm and height of 30 mm improves the discrimination power of the imaging method. The ASR algorithm performance increased in the ability to distinguish between a 10 cm side length of uranium cube from an equally-sized lead cube with a contrast-to-noise ratio (CNR) value of 3.2 ± 0.1, compared to the CNR value of 2.2 ± 0.07 when using cubic voxels with a side length of 10 mm. Following localising high-Z materials inside nuclear waste drums, identifying these materials in a few hours is possible. It was shown that this thesis introduces two new algorithms for material classification applications which are the Hybrid (HB) and the High Angle Statistics Reconstruction (H-ASR) algorithms. It was shown that the H-ASR algorithm is able to identify 10 cm and 5 cm cubes of

uranium from lead in 3 and 4.5 hours, respectively.

Table of Contents

List of Figures

List of Tables

Chapter 1

Introduction

Imaging and scanning techniques are some of the most popular methods for investigating objects, especially hidden ones located in inaccessible places, such as volcanos and pyramids. Historically, imaging has been efficiently used in the medical field as a diagnostic tool to scan the interior of the human body by applying computed tomography (CT) or X-rays [1]. Recently, imaging has led to the discovery of a hidden chamber inside the great pyramid of Khufu using cosmic muon radiography [2]. Additionally, cosmic muon radiography has been applied to monitor and study large bodies (e.g. active volcanoes' internal structures) [3]. In the past decade, several applications, such as archaeological, infrastructural and nuclear waste management applications, have applied non-destructive assay methods to investigate objects in various industrial fields.

In nuclear waste management, the non-destructive assay of nuclear waste makes is a highly valuable technique for characterising radioactive materials inside well-shielded nuclear waste packages. It significantly reduces the cost and the risk of exposure to ionising radiation that might occur when opening nuclear waste packages manually for investigation. It is necessary to characterise nuclear waste carefully to keep records of radioactive waste and dispose of it safely. The challenges of characterisation of complex conditioned radioactive waste include the possibility that conditioned waste comprises parts from various sources, the potential presence of a shield matrix and the potential for the physical structure of conditioned waste to change because of incineration or corrosion.

Many non-destructive imaging techniques can be used for studying nuclear waste packages contents. These techniques can be divided into two main categories: passive

and active scanning/imaging. Passive scanning measures heat or radiation emissions originating from radioactive materials inside a waste drum. For instance, calorimetry is a passive technique in which the heat produced by radioactive materials is calculated quantitatively to estimate the total radioactivity inside the investigated waste drum. Calorimetry also detects neutrons and gamma rays as signs of the presence of materials that emit gamma rays and neutrons during nuclear decay (e.g. uranium). However, gamma rays and neutrons can be stopped and absorbed by the shielding material; hence, a shield can prevent the classification of materials.

Active scanning usually involves external artificial particle sources that travel through the volume of interest to measure the beam's absorption or scatter on the other side of the object. For example, X-ray imaging is an active technique in which high-energy photon sources are placed on one side of the object of interest, and detectors are placed on the other side to detect the photons' flux rate. Thus, when relatively higher absorption rates are detected, they can be interpreted as photon beams encountering high-density materials. Using artificial radiation sources can be expensive, and this radiation can be stopped by the shielding matrix in a nuclear waste drum.

Muon scattering tomography (MST) is classified as a passive technique because it does not require an artificial source to scan the volume of interest. This technique employs cosmic muons, which are naturally occurring particles originating from cosmic rays. These particles reach the Earth's surface and have the extraordinary ability to penetrate both small and large structures. This method will be used in this thesis to address several challenges in the imaging and classification of heterogeneous materials stored in nuclear waste packages. The volume of interest is usually placed between two muon tracking systems to register incoming and outgoing muons. When muons travel through dense materials, they undergo multiple Coulomb scattering (MCS), which results in deflecting in their directions. The scattering information is then used to generate a 3D image of the volume of interest. Moreover, cosmic muons have a high penetration level that gives them the ability to travel through several hundred metres of rock before being absorbed, which is far beyond the penetration levels of both gamma rays and X-rays.

Several studies have demonstrated the feasibility of using MST to produce a 3D density map of well-shielded high-Z materials [4, 5]. However, it could be challenging to distinguish between materials with similar characteristics, such as uranium and lead. Uranium and lead have similarities in their atomic numbers, which are 92 and 82, respectively. Moreover, MST does not rely on a focused beam of muons directed to the object of interest, so they cannot be controlled by a human. Accordingly, imaging hidden objects may require a long period (weeks) of exposure to muons. This thesis

addresses many of these limitations as contributions to the development of the use of MST to investigate and monitor nuclear waste packages and for other applications.

Chapter 2 introduces the characteristics of cosmic muon particles and the benefits of exploiting them as an imaging source in muon tomography. The chapter also introduces the theory regarding muon particles interactions with matter. Then, the chapter summarises the current state of theoretical and experimental knowledge regarding the muon tomography technique, expounding on the interpretation of detecting cosmic muons in particle detectors. After that, the chapter presents a brief history of the muon tomography method use in various fields. Chapter 3 presents and discusses the state of the art of muon tomography as a technique in several applications. Chapter 4 describes muon detectors and the simulation method in detail, including simulation of cosmic muons arriving from the atmosphere and muon trajectory track fitting. It also describes the simulations of two types of nuclear waste packages. Chapter 5 describes the principles of the reconstruction algorithms most commonly applied to produce 3D density maps of volumes of interest. It also discusses each algorithm's strengths and limitations, leading to an optimisation of these already developed algorithms.

Then, chapter 6 covers the development and optimisation of the reconstruction algorithm covered in chapter 5, leading to the development of a novel reconstruction algorithm. The new developed algorithms are then used in machine learning applications to classify materials inside nuclear waste drums in Chapter 6. Finally, chapter 7 concludes the thesis by summarising the findings and contributions.

Chapter 2

Cosmic ray and theory

This chapter provides an overview of the characteristics of cosmic muons and the theoretical justification for the feasibility of using cosmic muons in imaging techniques. Moreover, it briefly explains the theoretical background of how cosmic muons interact with matter via MCS. Finally, it summarises the history of cosmic muons use in the investigation of small and large bodies and how the properties of muons have been exploited in the development of scanning/imaging technology.

2.1 Cosmic rays

Cosmic muons are naturally occurring particles that originate from cosmic rays and belong to the lepton family. Most cosmic rays that interact with the upper atmosphere of the Earth are protons (85%), alpha particles (12%) and electrons (2%), and the remainder comprises heavy nuclei [6]. This primary flux interacts with atoms in the Earth's atmosphere, consequently creating mesons and baryons that either continue interacting or decay into muons (μ), neutrinos (ν) and electrons. However, muons are mainly produced from pion (π) decay [6].

$$\pi^+ \longrightarrow \mu^+ + \nu_\mu \tag{2.1}$$

$$\pi^- \longrightarrow \mu^- + \bar{\nu}_\mu \tag{2.2}$$

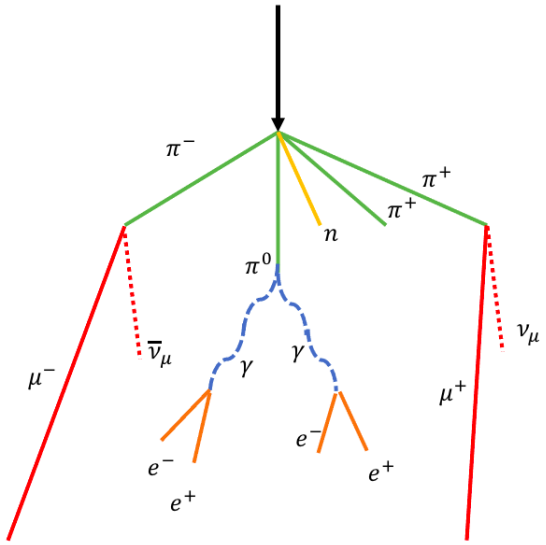

Figure 2.1: Schematic of a particle shower originating from cosmic rays. This shows several charged pions (π^+ and π^-) and neutral pions (π^0). The charged pions decay into muons and their associated neutrino or antineutrino.

2.2 Muon Particles

A muon is an elementary leptonic particle that is a part of the lepton family. Like other leptonic particles, muons participate only in the weak interaction and not in the strong interaction. Muons also are unstable fermions particles that have a spin of $\frac{1}{2}$, and decay through the weak interaction into an electron (e^-) or positron (e^+) along with associated neutrinos as follows:

$$\mu^+ \longrightarrow e^+ + \nu_e + \bar{\nu}_\mu \tag{2.3}$$

$$\mu^- \longrightarrow e^- + \nu_\mu + \bar{\nu}_e \tag{2.4}$$

where ν_e is an electron neutrino, ν_μ is a muon neutrino, $\bar{\nu}_\mu$ is a muon antineutrino, and $\bar{\nu}_e$ is an electron antineutrino. At sea level, the muon flux is approximately 1 muon per cm^2 per min [7]. Cosmic muons have a relatively large mass (207 times that of an electron): 105.6583745 $\pm$ 0.0000024 MeV [7]. Because of their long lifetime (2.1969811 $\pm$ 0.0000022 μ sec) compared to other unstable particles, muons have the highest probability of passing through the atmosphere and reaching the Earth's surface with high energy [7]. According to classical physics laws, muons with relativistic speed can

travel a distance of only approximately 660 m, which means that muons cannot reach the Earth's surface. However, the special theory of relativity supports the argument that muons can survive and reach the ground and beyond. Time dilation allows muons to travel a distance much longer than 660 m in the Earth's reference frame. This also explains muons' ability to travel through several hundred metres of rock before being absorbed, which is far beyond the penetration level of both gamma rays and X-rays. In practise, a muon's range in a body of standard rock is measured in units of kilometre-water-equivalent (km.w.e.), which 1 km.w.e. is equal to 10^5 g/cm^2 of standard rock. Figure 2.2 indicates the vertical muon intensity as a function of the depth in the rock.

At an energy loss level, muons deposit approximately 2 GeV of their energy into the air during the journey to the Earth's surface. Muons reach sea level with a mean energy of around 4 GeV, with angular distributions approximately proportional to $\cos^2\theta$ where θ is the zenith angle [7]. Figure 2.3 shows the spectrum of muons at sea level at a zenith angle 75° (opened-diamond points) and 0° (all other points). This figure shows that muons with low energy at higher zenith angles are most likely to decay before reaching the Earth's surface; hence, it is expected to see few muons with low energy at high zenith angles. The muon flux for applications like overburden measurements can be approximated by Gaisser formula [8]:

$$\frac{dI_\mu}{dE} \simeq \frac{0.14E_\mu^{-2.7}}{cm^2\ s\ sr\ GeV}\left[\frac{1}{1+\frac{1.11\ E_\mu\ cos\theta}{115\ GeV}}+\frac{0.054}{1+\frac{1.11\ E_\mu\ cos\theta}{850\ GeV}}\right] \tag{2.5}$$

where the factor of 115 GeV parameterises the contribution of pions (π), and the factor of 850 GeV parameterises the contribution of kaons (k). This equation assumes that both muons decay and the curvature of the Earth are negligible and only valid for muons with $E > \frac{100}{cos\ \theta}\ GeV$ and θ (zenith angle) less than 70 degrees.

2.3 Muon Interactions In Matter

The concept of detecting high-energy charged particles is based on the fact that charged particles deposit some of their energy into the detector materials. This means that charged particles passing through matter continuously interact with the matter's medium, leading to a loss of energy. This loss of energy is primarily caused by inelastic collisions between the charged particles and the electrons present in the atoms of the detector material. These collisions lead to the transfer of some of the particles' energy into a form of ionisation or excitation processes within the matter's medium.

In principle, the mechanisms of energy loss could vary depending on the nature of

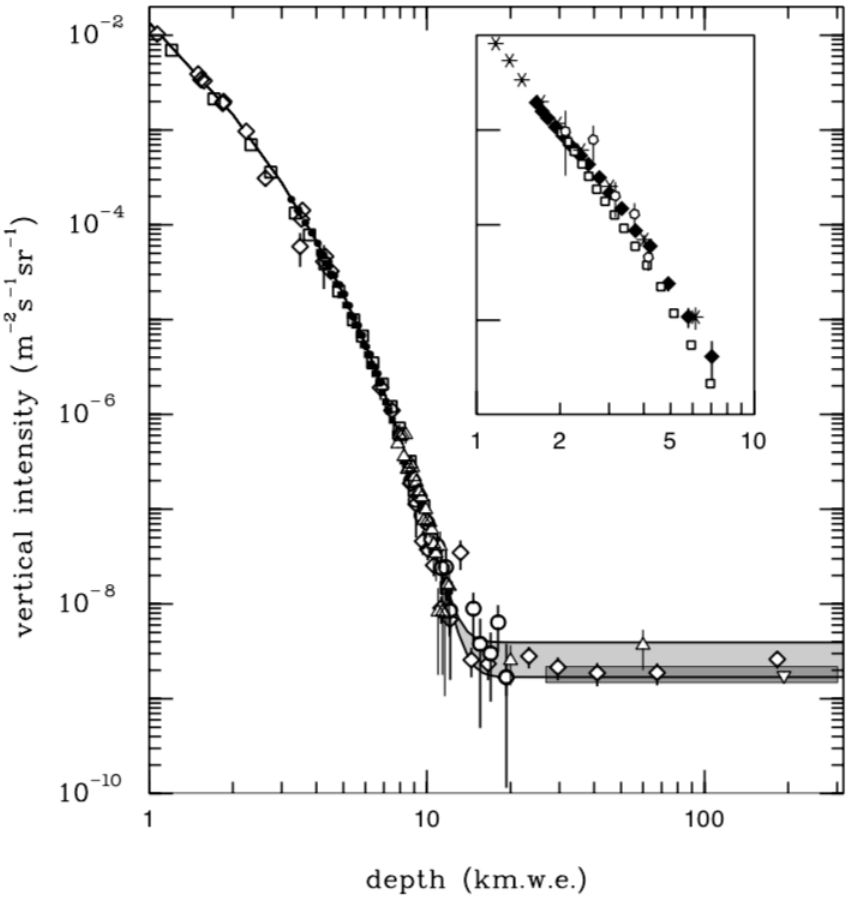

Figure 2.2: Muon flux versus depth in rock (measured in km in water; 1 km.w.e = 10^5 g cm^{-2} of standard rock). The inset represents muons' intensity in ice and water [7].

the incident particle and the matter's physical properties. The mean stopping power for heavy particles (e.g. high-energy cosmic muons) travelling through matter is provided by the following equation [7]:

$$\langle -dE/dx \rangle = a(E) + b(E) \tag{2.6}$$

where E is the total energy, a(E) represents the ionisation energy loss, and b(E) is the sum of contributions from Bremsstrahlung, pair production and photo-nuclear effects to the energy loss of a particle in matter. When $E \lesssim 100$ GeV, the b(E) is $\lesssim 1\%$ of $a(E)$ [17].

Energetic cosmic muons are like other charged particles that lose some or all of their energy when passing through matter. This loss of energy, or the material's stopping power, is described as a mean rate in a unit of MeV g^{-1} cm^2 for muons and

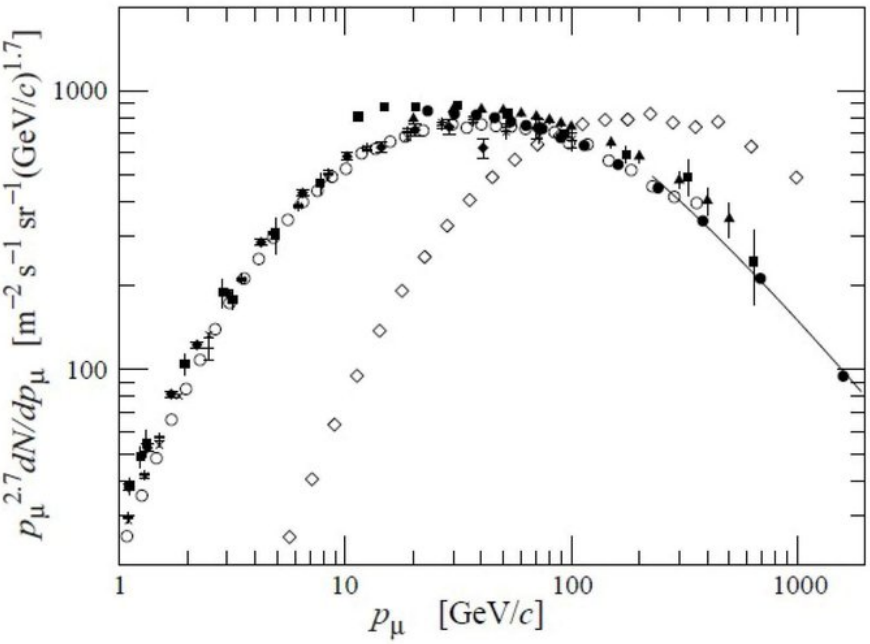

Figure 2.3: Muon spectrum at sea level, weighted by the momentum at two different angles. The diamonds (♢) represent θ= 75° [9], and the rest are for θ= 0° (♦ [10], ■ [11], ▼ [12], ▲ [13], ×, + [14], ∘ [15], • [16])[7].

other heavy particles by the Bethe–Bloch equation [18]:

$$\left\langle -\frac{dE}{dx} \right\rangle = Kz^2 \frac{Z}{A} \frac{1}{\beta^2} \left[\frac{1}{2} ln \frac{2m_e c^2 \beta^2 \gamma^2 W_{Max}}{I^2} - \beta^2 - \frac{\delta(\beta\gamma)}{2} \right] \tag{2.7}$$

For particles in the range of $0.1 \lesssim \beta\gamma \lesssim 1000$, this equation provides the mean rate of energy loss with an accuracy of a few percent [18]. Where K is equal to $4\pi N_A r_e^2 m_e c^2$ ($\simeq 0.307075$ MeV mol^{-1}cm^2), N$_A$ is Avogadro's number, r_e is the electron's radius, $m_e c^2$ is the electron's mass × c^2 (~ 0.510998928 MeV), where c is the speed of light, $\beta = v/c$ where v is the muon speed, γ is the Lorentz factor which is equal to $1/\sqrt{1-\beta^2}$, z is the charge number, Z is the atomic number, A is the mass number and I is the mean excitation energy. The expression $\delta(\beta\gamma)$ is the density effect correction for the ionisation energy loss. The variable W_{Max} represents the maximum energy transfer to an e (electron) occurring in a single collision [18]. For a particle with mass (M), W_{Max} is provided by the following equation:

$$W_{Max} = \frac{2m_e c^2 \beta^2 \gamma^2}{1 + 2\gamma m_e/M + (m_e/M)^2} \tag{2.8}$$

Figure 2.4 indicates the stopping power for positive muons in copper as a function of

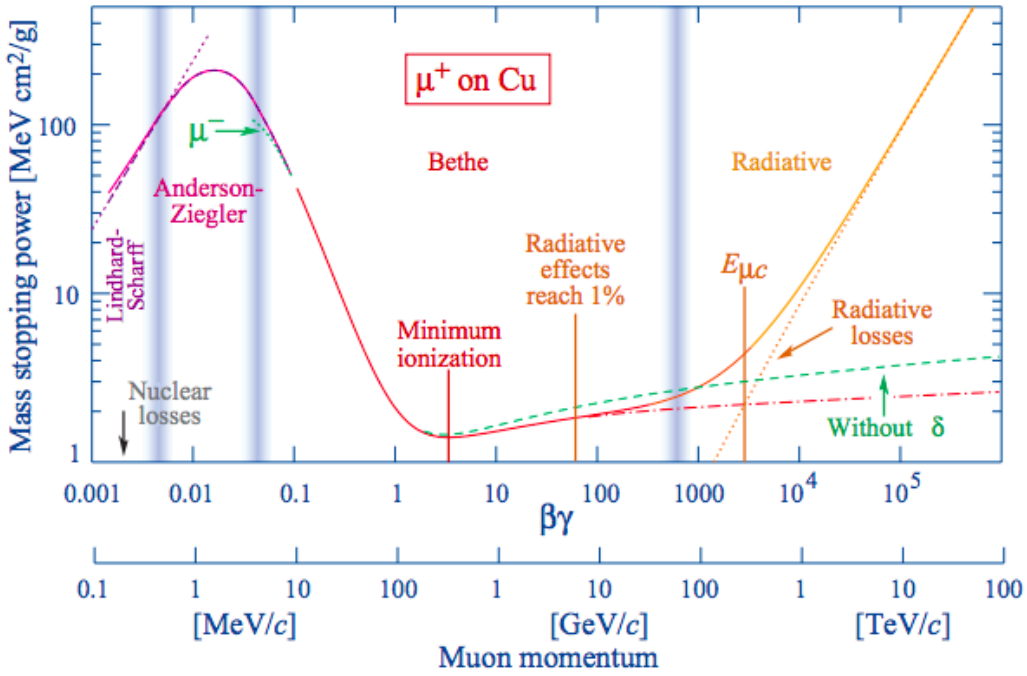

Figure 2.4: Muon energy loss as a function of their momentum is given by ($\beta\gamma = p/Mc$) for positive muons in copper. The solid curves represent the total stopping power, which reaches a minimum in the region labelled "Minimum ionisation". The mass stopping power in this region is about 1.4 MeV cm^{2}g^{-1}. [7].

muon momentum. Cosmic muons are minimum-ionising particles, as are most relativistic particles which have rates of mean energy loss close to the minimum [7]. The energy loss rate in the "minimum ionising" region is almost constant and varies based on the absorber materials (see Figure 2.5), e.g. for copper is approximately 1.4 MeV cm^{2}g^{-1}. Since muons are charged particles, they are likely to accelerate or decelerate when passing through the electric fields created by the atomic nuclei and atomic electrons of the material. Hence, muons emit radiation known as (Bremsstrahlung), and consequently lose energy when travelling through matter. Regardless, Bremsstrahlung effects contribute to the muons' energy loss; nevertheless, their contributions are not significant because the muon has a large mass compared to electrons [7].

In theory, a cross-section (emission probability (σ)) of the bremsstrahlung effect is proportional to the particle's radius (r_p). For example, an electron's cross-section is

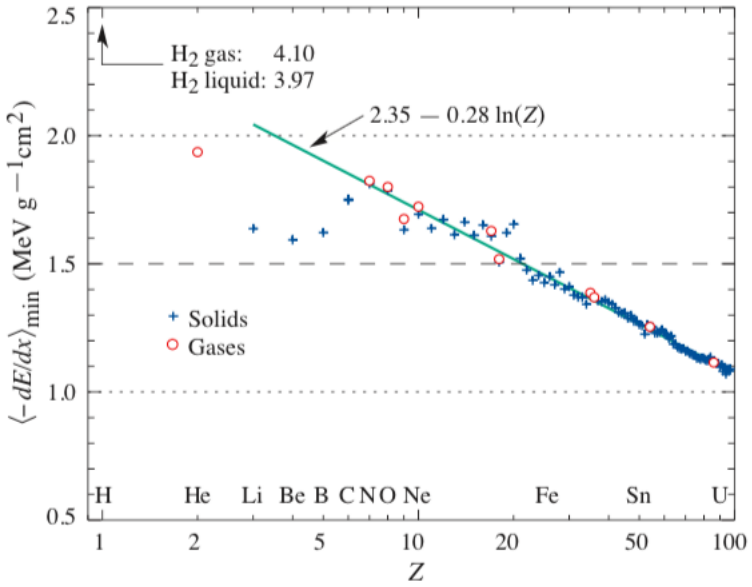

Figure 2.5: The mass stopping power, as a function of the atomic number Z, in the region of minimum ionisation is plotted for several materials with atomic numbers ranging from 7 to 100 [7].

calculated as follows:

$$\sigma \propto r_e^2 \tag{2.9}$$

where r_e is inversely proportional to the square of the electron's mass [7]:

$$r_e^2 \simeq (\frac{e^2}{4\pi\varepsilon_0 m_e c^2})^2 \tag{2.10}$$

Therefore, the large mass of the muon compared to that of electrons ($\backsim$ 207 m_e), explains that cosmic muons lose much less energy in the matter they traverse through than electrons do. However, for high-energy particles, including cosmic muons, ionisation becomes less important, and radiative processes become dominant in the contribution of the loss of energetic cosmic muons energy. Figure 2.6 shows the radiative process's significant contributions to muons energy loss in iron [7].

In summary, cosmic muons lose a small portion of their energy when traversing through matter, mostly due to electronic stopping power (ionisation and excitation). In principle, the sum of all contributions of all muon inelastic scatterings in matter is used to calculate a material's electronic stopping power.

Moreover, in addition to inelastic scattering with the atomic electrons, cosmic muons interact with nuclei in matter via Coulomb scattering as they travel through it.

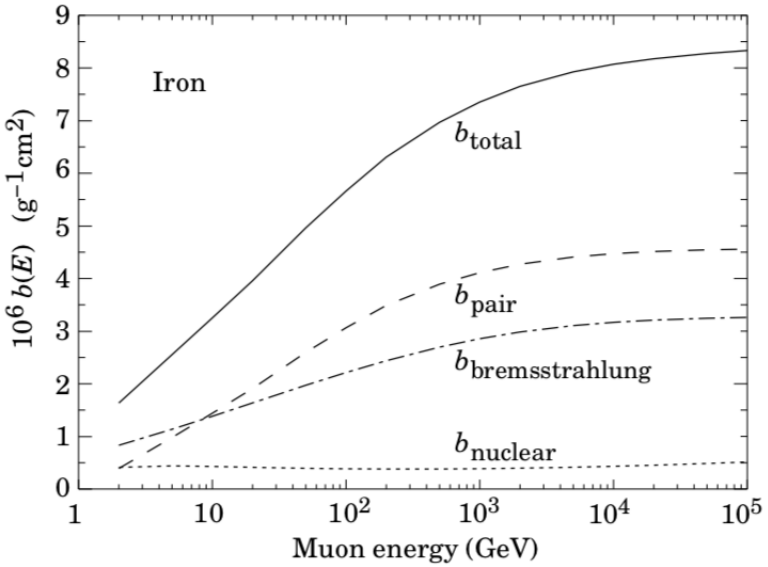

Figure 2.6: The contributions of bremsstrahlung, pair production and photo-nuclear interactions in muon energy loss in the material of iron [7].

The scattering that occurs because of this interaction is considered elastic scattering because the energy loss due to Coulomb scattering is negligible. However, this interaction can lead to high proportions of muons experiencing deflections because of the effects of elastic collisions. These deflections, even when very small, have been exploited by muon tomography to image objects of interest (detailed in the next section). The next section also explains the theoretical background of using cosmic muon scattering to extrapolate information about the matter through which muons pass using the MST technique.

2.4 Muon Tomography Techniques

Generally, muon tomography can be classified into two types: muon scattering tomography and muon radiography. Muon scattering tomography uses muon scattering information to produce a 3D image of the investigated object, whereas muon radiography uses information regarding the muon flux before and after travelling through an object to understand the investigated object's physical structure. Figure 2.7 shows an example of the experimental set-up for both methods.

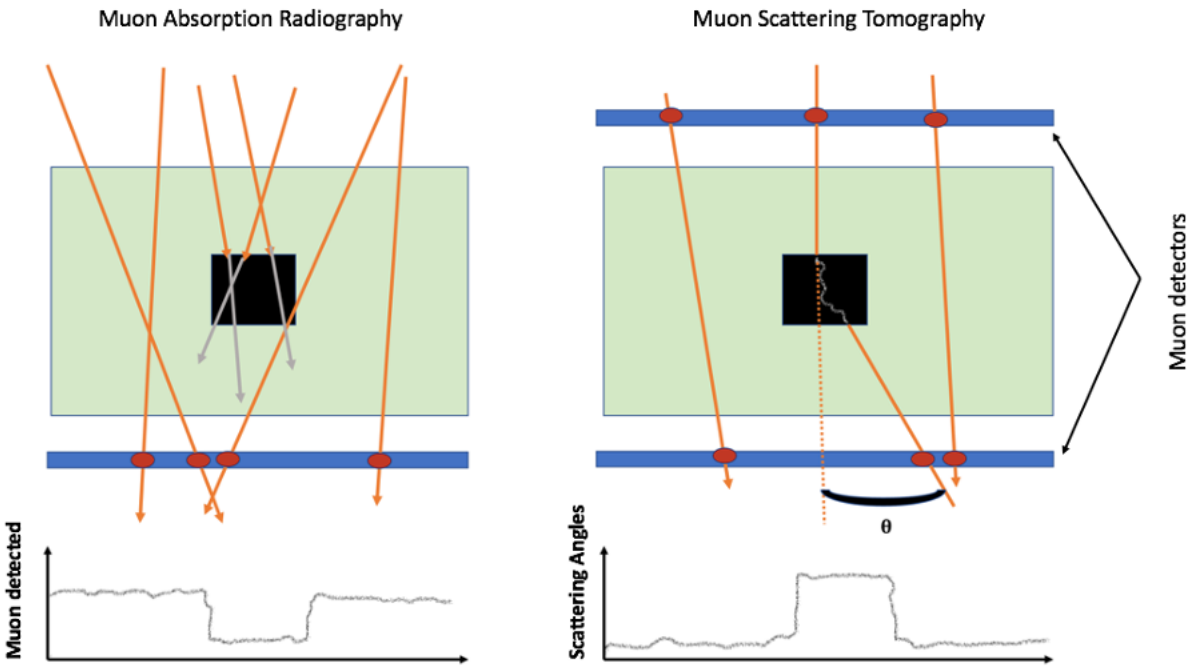

Figure 2.7: Schematic visualisation of both methods of muon tomography. The orange arrows represent cosmic muons passing through a volume of interest that contains a high-Z material (the black box). In the illustration of muon absorption radiography, the grey arrows represent the absorbed or attenuated cosmic muon.

2.4.1 History of Muon Tomography

In 1955, the early days of using cosmic muons to investigating object's properties, the absorption information of muons was studied by E. P. George [19] to estimate the thickness of the overburden above an underground tunnel in Australia. A few years later, a new approach of using cosmic muons in an actual imaging technique using the same technology as X-ray radiography was introduced and called muon radiography. The first attempt at using muon radiography as an imaging technique was in 1970 during the search for a possible hidden chamber in the pyramid of Chephren [20]. The images produced in muon radiography, reflect the increases or decreases in numbers of muons after passing through investigated objects. These numbers are usually compared to some simulation-based ("Monte-Carlo") expectation. A brief background of the concept of muon radiography will be explained in section (2.4.2).

At the beginning of the twenty-first century, Los Alamos National Laboratory (LANL) introduced the imaging method of muon scattering tomography [21]. Unlike muon radiography, muon scattering tomography uses information about muon scatter-

ing angles to produce a 3D image of the volume of interest. The first reconstructed 3D image of an object produced experimentally by MST is shown in Figure 2.8. It also shows a Monte Carlo simulation output of the same object simulated and reconstructed, and it successively agrees with the experimental output [21]. The test object was a tungsten cylinder with a radius and height of 5.5 and 5.7 cm, respectively.

Since then, the muon tomography technique has been shown to be an effective technique in many different applications, such as civil infrastructure, volcanology, archaeology and nuclear waste identification. In the last decades, many applications across the globe have proposed the use of muon radiography or muon scattering tomography for imaging purposes. Several examples of both methods of muon tomography applications that have justified the feasibility of the muon tomography technique will be presented in the next chapter.

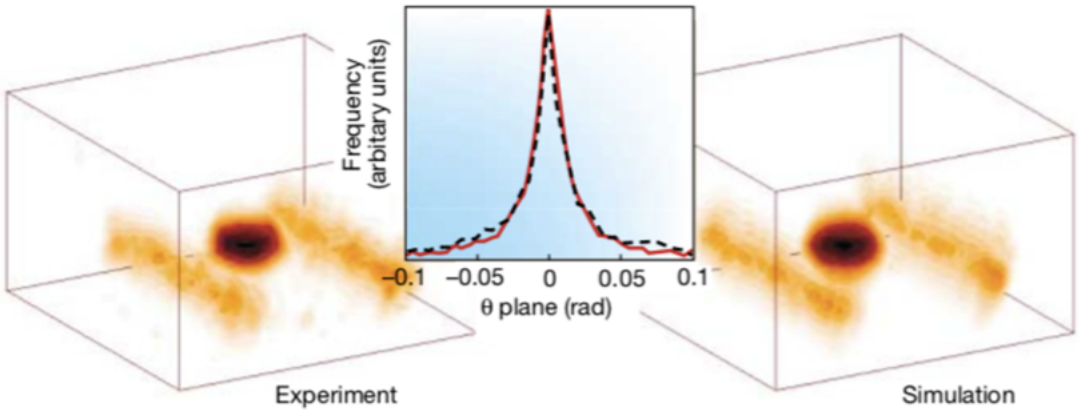

Figure 2.8: The reconstructed images of a tungsten cylinder with a radius of 5.5 cm and a height of 5.7 cm. The outputs also show images of two supporting steel rails. The inset plot shows almost identical width distributions of scattering angles for muons passing through the tungsten cylinder for the experimental and simulation data [21].

2.4.2 Muon Absorption Radiography

In theory, muon radiography works similarly to the principle of X-ray radiography. The imaging set-up for an X-ray works by placing an X-ray source on one side of the object of interest (e.g., patient) and an X-ray detector on the other side. Then, the transmitted X-rays are measured after passing through the patient's body [22]. X-rays are more likely to be absorbed in varying degrees by different parts of the human body, e.g. dense bones absorb more X-rays than soft tissue [22]. This reveals

the presence of a high-absorber material inside the inspected object. However, X-rays cannot pass through all objects because they can be stopped by shielding materials of small thickness.

The limitations of imaging shielded objects by X-rays can be avoided by using cosmic muons, which have a higher level of penetration through matter. For example, they can pass through approximately 10–100 metres of rock. The muon absorption or transmission imaging method is based on the energy loss of muons when they interact with the matter through which they travel. When a muon passes through matter, it might be absorbed because of the loss of its energy (explained in section 2.3). The transmission level is defined as the ratio between the muons flux detected by the muon detectors after passing through the object of interest and the detected flux when the detectors are free from the object. A one-sided detector system is placed behind or in the shadow of the inspected object to measure the attenuated muon flux distributions passed through the object. The muon flux interacts with the investigated object depending on the object's thickness (x) and density (ρ). The number of muons that manage to pass through the investigated object is the object's opacity (ϱ). Opacity is defined as the amount of matter that muons encounter during their travel throughout the object of interest. The opacity is expressed in units of $[\mathrm{g} \cdot \mathrm{cm}^{-2}]$ and can be calculated using the integrated object's density and the length of the muon's path through the object:

$$\varrho = \int \rho \, dx \tag{2.11}$$

The number of muons that pass through an object is higher if they travel through an object with low opacity. To reconstruct a 3D image of the inspected structure, the detectors can be moved around the object to collect data from several points of view. The transmission imaging mode uses a single muon detector placed downstream of the object of interest to detect the muons that pass through the object. An example of a muon radiography set-up is illustrated in Figure 2.9.

The attenuation level of muons inside an object depends on the object's physical and chemical properties. For instance, the inspected object's thickness and density can influence the number of muons that successfully pass through the object. Thus, it is possible to generate a density map for the inspected structure by measuring the transmitted muon flux through the structure. Muon radiography exploits the free availability of cosmic muons with high penetration levels to image and study large bodies, such as volcanoes.

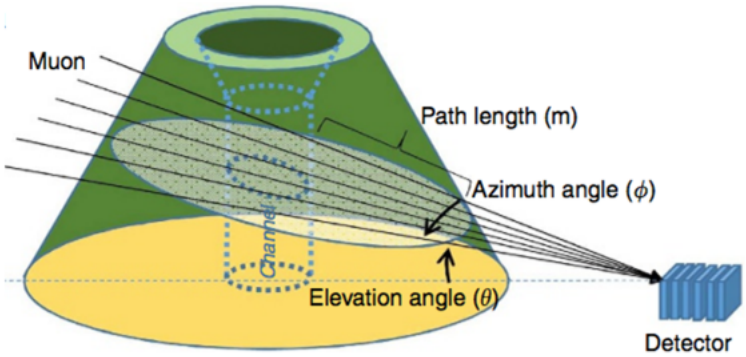

Figure 2.9: A depiction of the muon absorption radiography concept for imaging volcanoes [23].

2.4.3 Muon Scattering Tomography

Despite the fact that cosmic muons have a large mass, they can undergo multiple scattering events as they travel through matter. These scattering events are interpreted according to the fact that muons are charged particles; hence they interact with the nuclei present in the medium of matter via Coulomb's law. This results in MCS, the scattering of muons through the matter. The multiple scattering of muons throughout the matter leads to the creation of a random walk pattern, where the muon changes its directions several times. A representation of an incident particle random walk is indicated in Figure 2.10. It also shows that when a muon travels through matter, it might exit the matter in a different direction from its direction when it entered the matter. Thus, the scattering angle here is defined as the angle between the entry and exit points.

In principle, a muon's scattering angle is inversely proportional to the radiation length (X_o) of the material through which the muon passes. Statistically, the distribution of the projected scattering angles of the muons through a material with a thickness of X is approximately Gaussian, with width σ given by the following equation:

$$\sigma \approx \frac{13.6MeV}{\beta cp} z\sqrt{X/X_o}(1 + 0.038\ ln(X/X_o)) \tag{2.12}$$

where βc is the muon velocity, p is the muon momentum [24, 25], z is the muon's charge, and X_o is the mean distance through a material that an electron must traverse to reduce its energy by a factor of $1/e$, and it is determined in units of $(\mathrm{g} \cdot \mathrm{cm}^{-2})$ using the following equation:

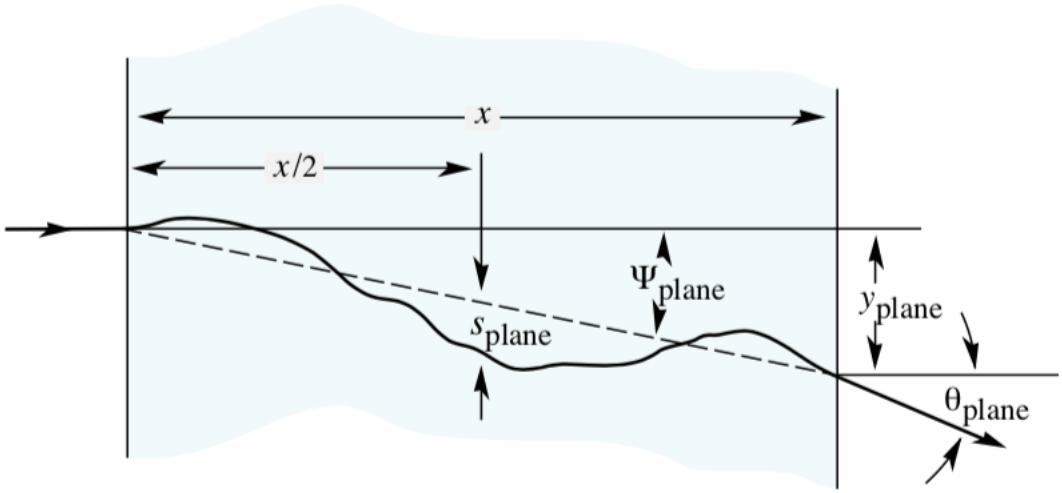

Figure 2.10: A representation of the random walk due to MCS events, where s, ψ and y are random variables [7].

$$X_o \approx \frac{716.4\ A \quad \text{g cm}^{-2}}{Z(Z+1)ln(287/\sqrt{Z})} \tag{2.13}$$

where Z is the atomic number, A is the mass number and ρ is the density [7]. Unlike other imaging techniques, such as CT, which employ a focussed narrow beam aimed at a target, MST simply places the volume of interest between two tracking systems to reconstruct the muon's trajectories as they enter and exit the object (see Figure 2.11). To produce a 3D density map of the investigated volume, multiple layers of the muon tracking system are arranged in the X–Z and Y–Z planes to register the muon hit positions. Reconstruction of the 3D trajectories of the muons entering and exiting the volume of interest can be obtained. Hence, by using the information on the muon trajectories to calculate their scattering angles across the volume of interest, a 3D density map of the volume can be produced.

Regardless of a material's thickness, according to equations 2.12 and 2.13, cosmic muons are highly sensitive to the proprieties of the materials through which they pass, specifically the radiation length of the material. Consequently, the radiation length is inversely proportional to the atomic number, which explains the importance of using cosmic muon as a source in MST. Different elemental properties are listed in Table 2.1, which clearly shows that the radiation length (g$\cdot$ cm^{-2}) of materials decreases as atomic numbers increase. Theoretically, a large scattering angle of muons passing through a volume might be caused by the presence of a high-Z material in the volume. Thus, all regions containing high-, medium- and low-Z materials inside a volume of interest can

be identified.

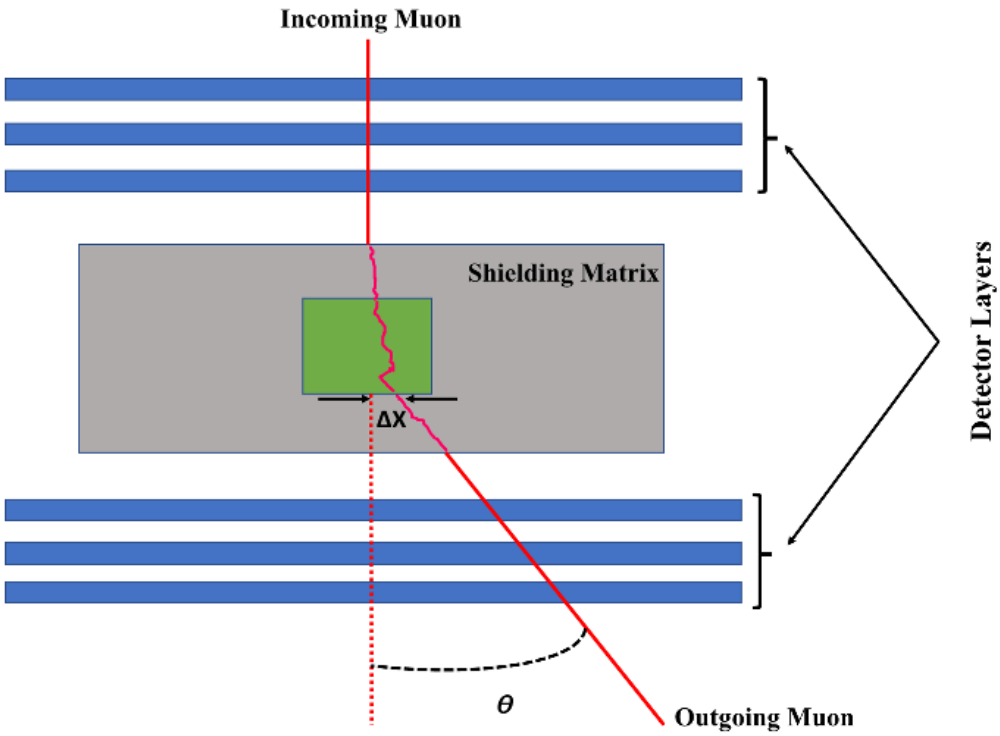

Figure 2.11: Schematic depicting a generic muon scattering tomography system comprising tracking chambers placed above and below a volume of interest containing a cube of high-Z material in green. The solid red lines represent the trajectories of the incoming and outgoing cosmic muons.

2.5 Summary

Non-destructive imaging techniques are classified into two main types: passive and active. Muon tomography is a passive technique that does not require an artificial radioactive source. The current state of knowledge about muon tomography as an imaging/scanning technique has developed significantly since its first use in 1970. The characteristics of cosmic muons with high-penetrating power that are naturally available everywhere make them a valuable resource for investigating well-shielded large and small bodies.

The theoretical background explained in this chapter includes the fundamental and general background of cosmic muons interactions with matter. More detailed

Material	**Z**	ρ **(g/cm^3)**	X_o **(cm)**	X_o **(g $\cdot$ cm^{-2})**
H_2 (gas)	1	8.376×10^{-5}	7.527×10^5	63.04
B	5	2.370	22.23	52.68
Na	11	0.9710	28.56	27.74
S	16	2.000	9.748	19.50
Ca	20	1.550	10.42	16.14
Cu	29	8.960	1.436	12.86
Sr	38	2.540	4.237	10.76
Ag	47	10.50	0.8543	8.97
Cs	55	1.873	4.434	8.31
Tb	65	8.230	0.8939	7.36
W	74	19.30	0.3504	6.76
Pb	82	11.35	0.5612	6.37
U	92	18.95	0.3166	6.00
Pu	94	19.84	0.2989	5.93

Table 2.1: Atomic number, density and radiation length for different materials. The radiation length values are provided in both (cm) and in (g$\cdot$ cm^{-2}), and X_o is weighted by density for the first case [7, 26].

information is available that explains cosmic particles interactions with matter in depth [7, 18]. Muon radiography has exploited the principle of muon energy loss in matter that leads to muon flux attenuation. Additionally, muon scattering tomography has exploited the nature of the MCS theory regarding the interactions of muons with matter and used muons to identify materials.

Chapter 3

Applications of Muon Tomography

The applications of muon tomography can be classified into two main types depending on the imaging mode: muon absorption/transmission (explained in section 2.4.2) and muon scattering (explained in section 2.4.3) applications. This chapter reviews previous studies using muon tomography as an imaging tool in both modes for different applications. The strengths and limitations of both imaging modes are also briefly highlighted.

3.1 Applications of Absorption Radiography

Since the 1950s, the muon absorption radiography has shown potential as a non-destructive method to view the inside of large structures by producing a density map of the structure of interest. The basic concept of muon radiography with the powerful characteristics of cosmic muons has prompted researchers and commercial establishments to use this method in imaging and monitoring large structures. This section highlights some of the recent applications that have resulted in promising conclusions regarding the feasibility of applying muon radiography as an imaging and scanning technique.

3.1.1 Archaeological and Volcanology Applications

The high-penetrating level of cosmic muons through objects gives archaeologists and volcanologists the opportunity to study the inside of ancient large pyramids and to mon-

itor active volcanoes, respectively. In 1970, the first attempt to use muon absorption radiography was made when scanning the second pyramid of Chephren, searching for an unknown chamber [20]. The measurement of cosmic muons that travelled through the pyramid were compared to the data obtained from simulations, as the pyramid had been simulated without any unknown chamber. The presence of the unknown chamber was not suggested as there were no differences observed between the experimental and simulated data. It was expected that more muons would cross the pyramid if there was a region with a lower density (unknown chamber) compared to the surrounded rock density. In the study by [27], the measurement of cosmic muon flux was applied to investigate the roof of the Grotta Gigante, a natural cave located near Trieste in Italy. The muon detector was positioned inside the cave, and then the measured muon flux obtained inside the cave was compared to a computed expected muon flux. The expected muon flux was calculated for zenith angles ranging from $\theta \geq 0^\circ$ to $\theta \leq 70^\circ$, and for azimuth angles spanning from $\phi \geq 0^\circ$ to $\phi \leq 360^\circ$. The study revealed several anomalies in the rate between the measured and expected muon flux, suggesting that a variation in density in the region defined by $\phi > 210^\circ$ to $\phi < 230^\circ$ and $\theta > 55^\circ$ to $\theta < 60^\circ$ [27].

Recently, a similar study was conducted in 2017 to scan/image the inside of the pyramid of Khufu in Egypt [2]. The discovery of a large void in this pyramid was achieved using three different muon detectors: nuclear emulsion films, scintillator hodoscopes and micro-pattern gaseous detectors. Information regarding the detector characteristics is summarised in Table 3.1. The nuclear emulsion and the scintillator hodoscope detectors were placed inside a known chamber in the pyramid (Queen's chamber), while the gaseous detector was placed outside the pyramid near the pyramid's base.

The outputs of the nuclear emulsion detector are shown in Figure 3.1, indicating the 2D histograms (a and b) of the muon flux that were detected at two positions, NE1 and NE2, in the Queen's chambers and in a narrow corridor called Niche, respectively. The density maps showed an increase in the detected muons that passed through known chambers, e.g. the King's chamber (A) and the Grand Gallery (B), as well as the newly discovered void highlighted by a white rectangle. Figures (c) and (d) show the results of Monte Carlo simulations showing the known chambers. The figures labelled in (e) and (f) are the slices of the angular regions of $0.4 \leq \tan\theta_y < 0.7$, indicating the newly detected void with an excess of number of muons in two regions: the new void and the known Grand Gallery corridor, labelled in B.

Characteristics	Nuclear Emulsion	Hodoscopes	Gaseous Detector
Developer	Nagoya University	KEK[1]	CEA[2]
Spatial Resolution	1 μm	10 mm	450 μm
Height	0.2 mm	$\sim$ 1 to 1.5 m	60 cm
Active Area	75 cm $\times$ 60 cm (NE1) 90 cm $\times$ 50 cm (NE2)	1.2 m $\times$ 1.2 m	50 cm $\times$ 50 cm
Power Supply	No	300 W	35 W

[1] **High Energy Accelerator Research Organisation.**
[2] **Commissariat a l'Energie Atomique et aux Energies Alternatives .**

Table 3.1: The general properties of the muon detectors contributing to the discovery of the new void in Khufu's pyramid. NE1 and NE2 are the chosen positions of the nuclear emulsion films in the Queen's Chamber [2].

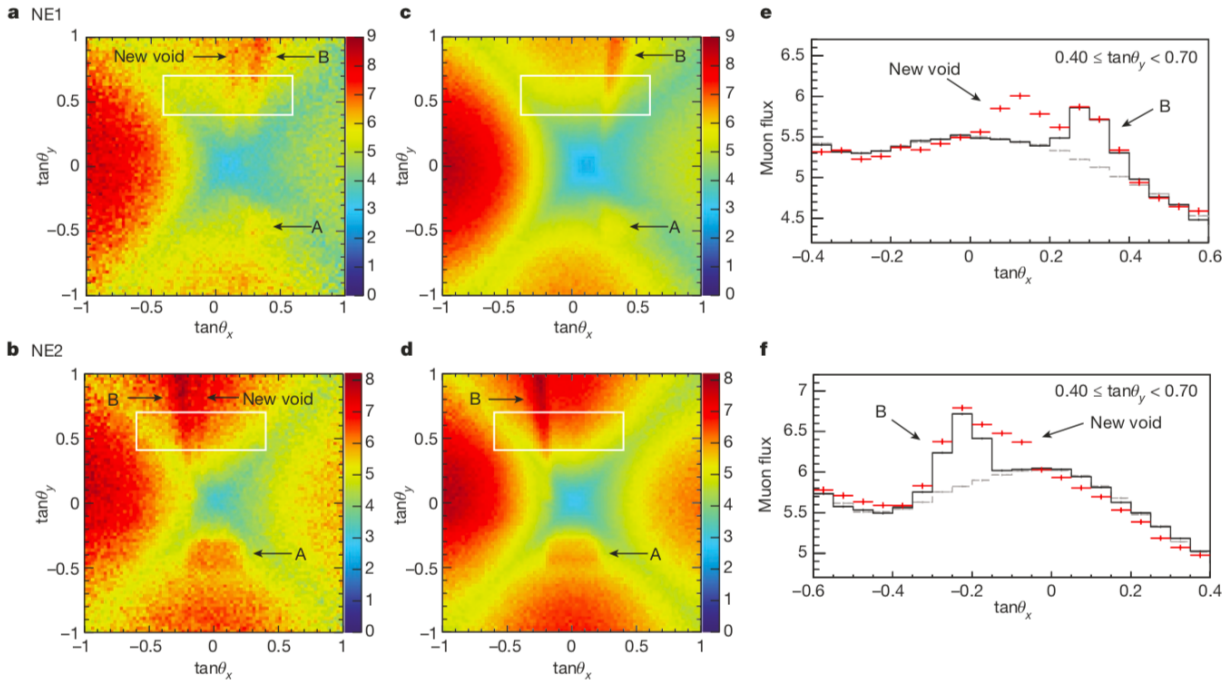

Figure 3.1: Nuclear emulsion outputs from imaging Khufu's pyramid. Figures (a) and (b) are the 2D histograms of the detected cosmic muon flux, the Z axis represents the muon count with the units of muon per cm^2 per day per steradian at two positions, the Queen's chamber (NE1) and the 'Niche' (NE2), which are both known chambers. Figures (e) and (f) indicate the excess of the detected muons flux within the highlighted angular regions of $0.4 \leq \tan\theta_y < 0.7$ [2].

Meanwhile, two gaseous telescopes were placed in front of the north side of the

pyramid facing the direction of one of the known chambers (the Grand Gallery). The two telescopes ('Alhazen' and 'Brahic') were placed close to each other to combine the muon flux data detected by both detectors. The results of using gaseous detectors confirmed the presence of an unknown void in the same place claimed by the University of Nagoya. Statistically, a significant excess in the number of muons was detected in two regions inside the pyramid: the known Grand Gallery and the new void. The statistical excess of muon flux was found to be 8.4 σ and 5.8 σ for the Grand Gallery and the new void, respectively [2]. Figure 3.2 shows the density maps (in a and d) of the muon flux that traversed through a part of the suspected region in the pyramid. The regions of interest are highlighted in black-dotted rectangles within the density maps, and then they have been horizontally sliced. Figures (b) and (c) indicate the excess of muon flux in the upper and lower highlighted regions in the density map (a), respectively.

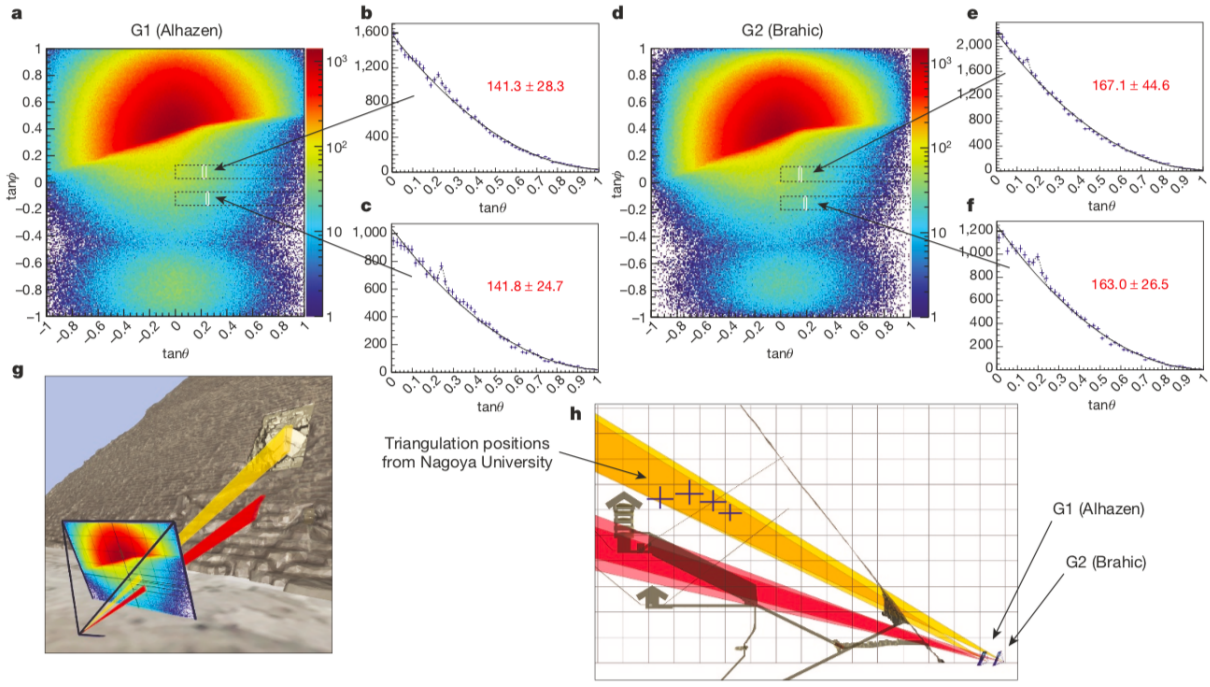

Figure 3.2: The gaseous detector outputs from imaging of the Khufu pyramid. Figures (a) and (d) are the 2D histograms of the detected cosmic muon flux in a logarithmic scale at two positions: by Alhazen (G1) and by Brahic (G2). Figures (b) and (c) are the slices of the upper and lower highlighted regions, respectively, in (a), showing the excess of the detected muon flux by Alhazen. Figures (g) and (h) show the detector positions and the angular area of the observed muon flux excess through the Grand Gallery in red cones and through the new void in yellow cones [2].

Muon radiography has also been shown to be a possible technique to image or monitor the internal structure of volcanoes. In the last decade, several research groups in geo-science have applied muon radiography to investigate volcanoes across the world, e.g. [28, 29, 30, 31] and more recently in [32]. In 2012, the muon radiography method was used to investigate a famous active volcano in Guadeloupe, which is called La Soufrière [33]. A telescope made of three scintillator matrices was used. The telescope was installed on the southern side of the lava dome, which is called Ravine Sud (location 1), and was then moved to a place called Roche Fendue on the eastern side of the dome (location 2). Figure 3.3 shows the average density as density anomalies relative to a reference density obtained from the muon flux detected at the two locations. The 2D density maps show that the structure of the lava dome is a combination of low-, medium- and high-density regions. The massive lava appeared in the higher density regions with an average density of $\backsim$ 1.9 g $\cdot$ cm^{-3} (labelled RF1 and RF5). The regions labelled RF4 and RF2 have low densities, which correspond to a known void (cave) and a hydrothermal area, respectively, with an average density of $\backsim$ 1.1 g $\cdot$ cm^{-3}. There is also a visible dense rock with intermediate density in the region of RF3, situated between the two low-density regions of RF4 and RF2 [33].

Recently, the results of three years of monitoring the largest active volcanic mountain in Italy, Mount Etna, have been published [34]. Muon detectors were used to observe any possible anomalies within the internal structure of Etna mountain. The muon telescope used in this study consisted of three positions-sensitive modules, each module built with 99 scintillating bars with a dimension of 1 cm $\times$ 1 cm $\times$ 100 cm and with a total active area of 1 m^2 [34]. The telescope was placed northeast of the volcanic crater to detect the muon flux that managed to cross the structure of the volcano. Simultaneously, the telescope also registered the muon flux coming from the opposite direction without any obstacle and then registered it as open-sky data. The alteration of densities in the inspected volcano over three years of exposure time was observed, as shown in Figure 3.4. The results were plotted in a scale of R values obtained from the daily average of the ratio between the muon flux that crossed the volcano structure and the data of the muon flux of the open-sky setup. This research led to an early observation of a cavity under the roof of the northeast crater in 2017 before its collapse at the end of the year. This void can be observed in the 2017 figure with higher R values compared to the surrounding regions. This abnormality resulted in an excess of muon flux travelling through a structure with a low density (the new void).

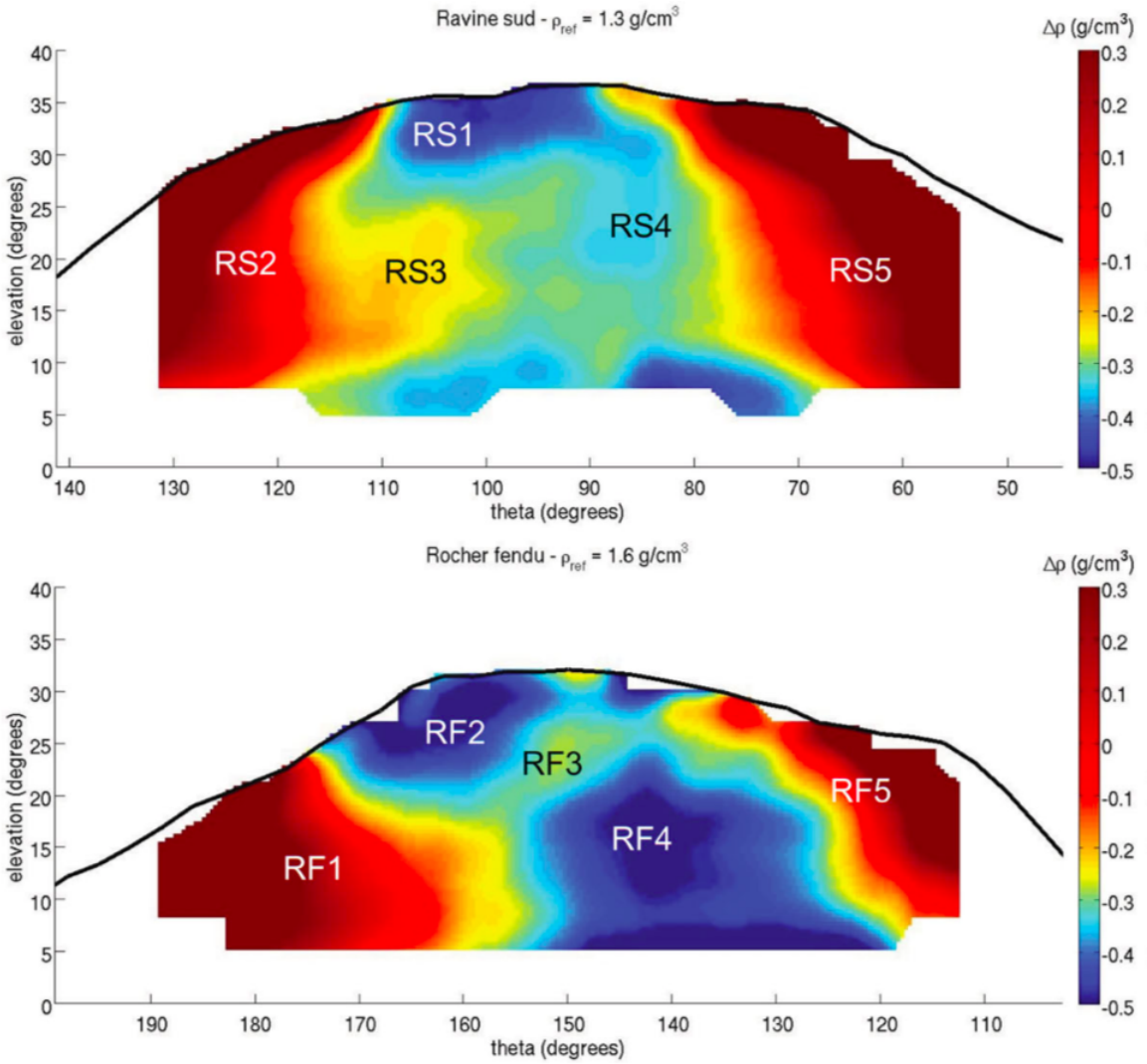

Figure 3.3: The density maps obtained from the muon flux detected by the muon telescope at two designated locations: Ravin sud (above) and Roche Fendue (bottom). Both maps show the heterogeneity in the density structure of the inspected volcano. The Z bar represents the average density relative to the determined reference density of each figure (stated in the title of the figure). RF2 and RF4 regions correspond to structures with low densities, which are the hydrothermal area and the large known cave, respectively [33].

3.1.2 Civil Engineering Applications

Muon radiography has also contributed to monitoring and imaging large structures in civil engineering fields, such as tunnels, towers and mining sites. It is necessary to regularly monitor civil infrastructures, especially historical sites that people still

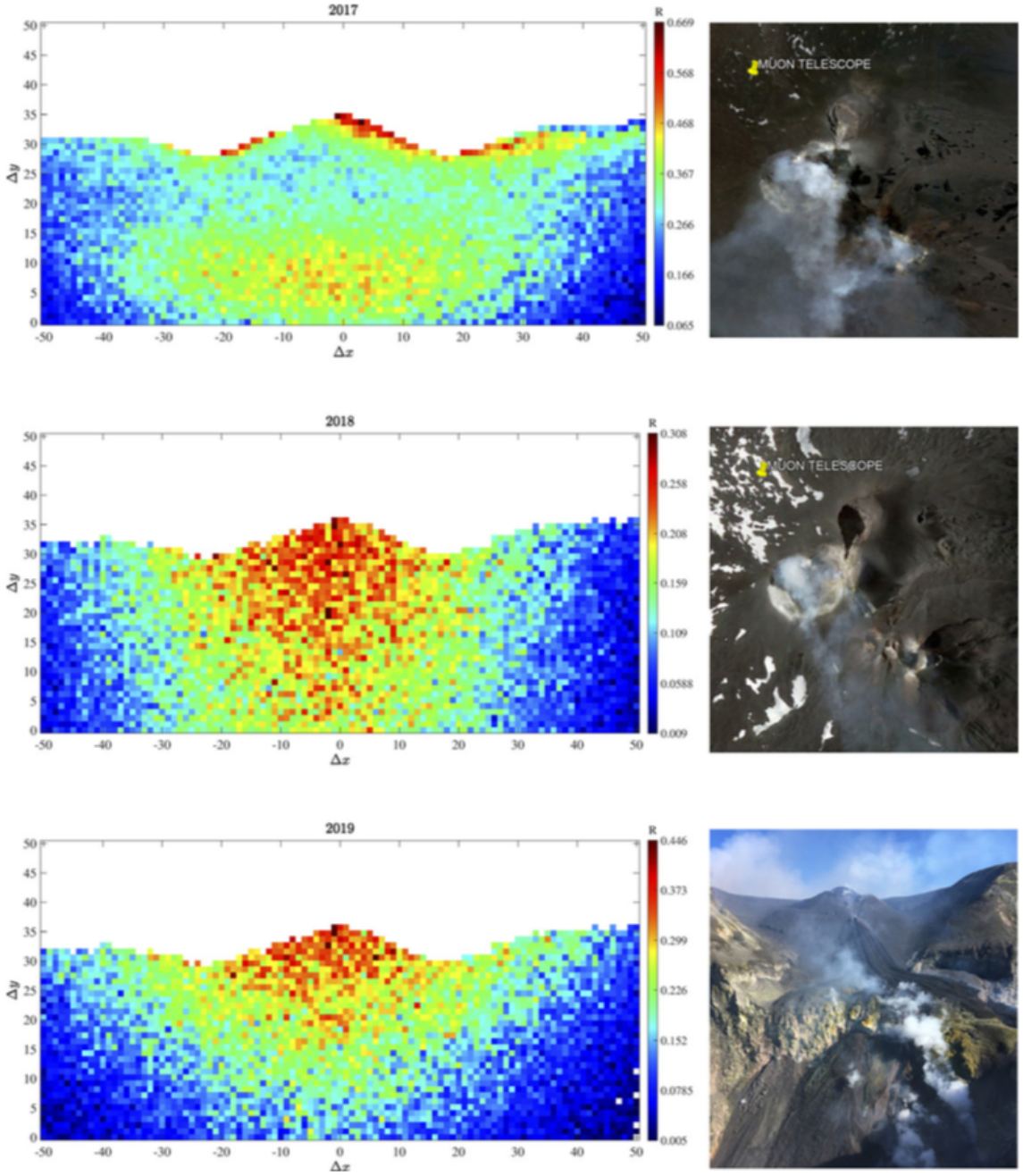

Figure 3.4: Comparison of the 2D muographic images of the Etna volcano produced in 2017 (upper), in 2018 (middle) and in 2019 (bottom). The density maps represent a scale of R values that were calculated from the muon flux information before and after travelling through the volcano structure. The abnormality of high R values in 2018 compared to 2017 correspond to the roof structure, which collapsed at the end of 2017. The pictures on the right-hand side are birds-eye views of the crater [34].

visit, to avoid any potential hazard. In recent years, many experiments have yielded promising results of using muon radiography in this field, e.g. imaging water towers in [35], an ancient mine in [36] and Carbon Capture and Storage (CCS) reservoir monitoring [37]. More recently, in 2020, a study was performed to check a railway infrastructure of a disused tunnel called Alferton Old Tunnel in Nottinghamshire [38]. The tunnel was built in the 19^{th} century with a total length of 770 m. The muon radiography technique was applied using two layers of plastic scintillators with an active area of 30 cm $\times$ 90 cm. The detector system was installed in the back of a van, and the muon flux data were taken in ten-metre interval patterns alongside the tunnel. The muon flux information was obtained by summing the triggers recorded by the detector system and was then converted to muon rate values (muon per 30 minutes) [38]. The information of the typical muon flux in the area was measured without any obstacles several times before recording the data inside the tunnel.

Figure 3.5 shows the results of the measured, expected and inferred muon rate per 30 minutes as a function of distance along the tunnel. As shown by the figure, the muon rate significantly dropped after entering the tunnel from either entrance. This is expected as the information from the topographical survey stated that the overburden increases gradually into the tunnel; however, despite the broad agreement of the measured muon rate with the expected rate, the regions between (150-200 m) and (600-700 m) showed an unexpected measurement rate compared to the expected rate. This is due to the limitations of the topographic data that had been collected in a straight line above the whole tunnel [38]. Because the detection method of the muon detector was based on an angular range, the detected muons might have encountered a larger or smaller overburden away from the straight line, leading to an inaccurate estimation of the muon flux information. This abnormality was corrected by estimating the overburden thickness using the open-sky measurements and the muon flux that crossed a particular region.

As a result, the inferred muon rate showed excellent agreement with the measured muon rate, except for the three known open shaft regions. The statistical excess of the muon rate in the regions of the open shafts was found to be about 10.0 σ [38]; however, the main finding of this study is the observation of a significant excess of the muon rate between 75 m and 80 m when compared to the inferred rate. This abnormality in the muon rate could be a sign of changes in the overburden structure of this region, which then was identified as a hidden shaft (see Figure 3.6).

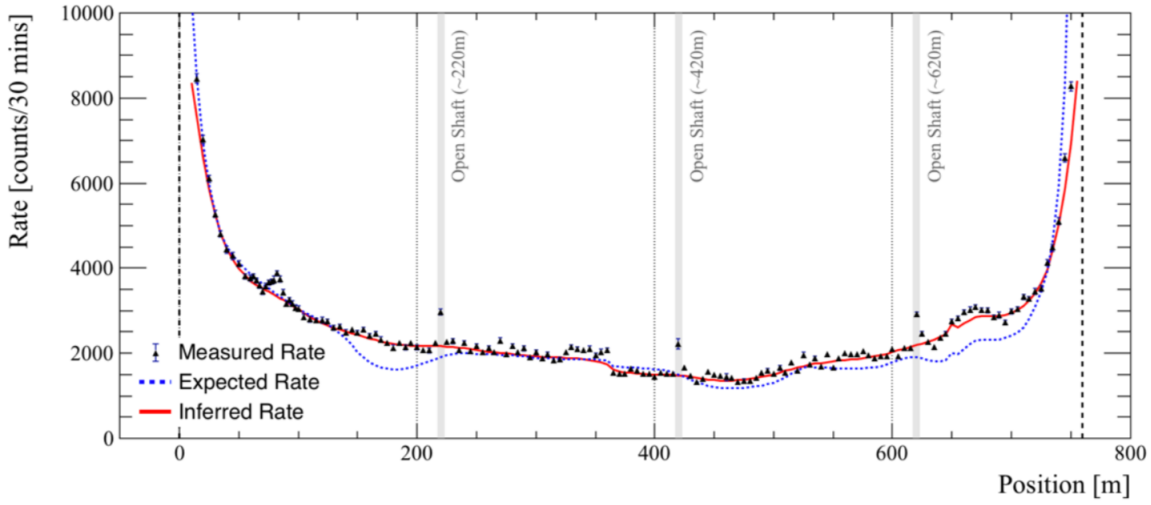

Figure 3.5: Comparisons between the measured muon rate (in the black triangle) and both the expected and inferred muon rates in blue-dashed and red-solid lines, respectively. The excess of the measured muon rate between 75 m and 80 m was identified as a hidden shaft. The anomalies in the measured muon rate at 350 m do not represent any change in the overburden in this region and were reported to be due to a fault in the detectors' system cables [38].

3.2 Applications of muon scattering tomography

The technique of muon scattering tomography (MST) was first introduced in 2003 by [21]. Since then, it has been shown to be an effective method in several applications, such as safeguarding and nuclear waste characterisation applications. Unlike muon radiography, the MST method is designed to investigate small- and medium-sized bodies placed between two tracking systems. This setup limits the size of the volume of interest to the gap between the tracking systems. This also means that the volume of interest is more controlled and does not require the further information that is needed for muon radiography, e.g. muon flux information. Furthermore, the concept of muon scattering method does not significantly rely on the count of muons crossing the volume under investigation. Thus, the inspection time can be much faster compared to the muon radiography method. This section highlights the state-of-the-art of MST technique. Examples of different studies across the globe that have applied MST as an imaging tool have proved the feasibility of the MST method for several applications, which are briefly presented in this section.

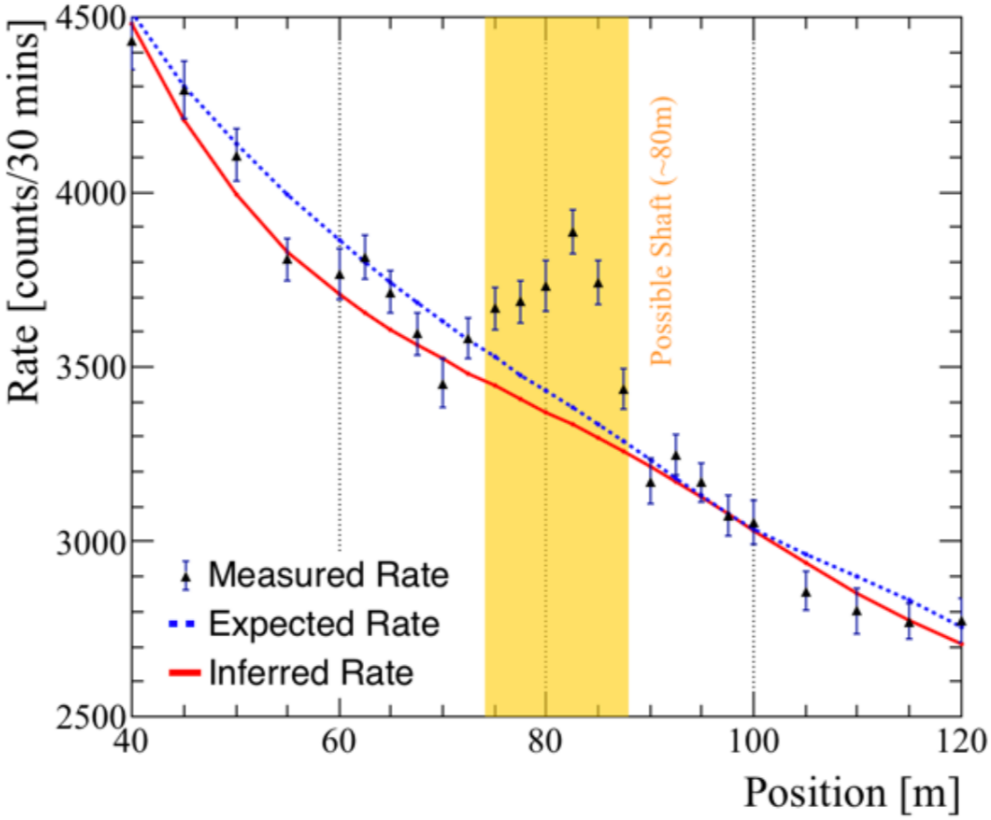

Figure 3.6: Comparisons between the measured muon rate and both the expected and inferred muon rates at the region of interest between 40 m and 120 m. The excess of the measured muon rate between 75 m and 80 m is highlighted by a yellow rectangle, which has been identified as a hidden shaft [38].

3.2.1 Safeguards applications

Globally, the safeguards security system works against any potential misuse of special nuclear materials (SNM) and spent nuclear fuel (SNF) for nuclear weapon purposes [39]. Scanning thousands of shipment containers that cross borders requires a quick and reliable method to prevent any smuggling of SNM. In 2003, the MST technique was first used by Los Alamos National Lab (LANL) to scan commercial objects, such as containers and cars [21]. The study showed promising results of using MST to detect high-Z materials hidden inside a large volume of low-Z materials. This technique has attracted the attention of several research groups across the world. Examples of studies in which muon tracking systems and reconstruction algorithms in the scanning/imaging field were developed include [5, 40], and more recently, [41, 42]. A few years later, the LANL built a large muon tracker consisting of 12 layers of a muon tracking system with

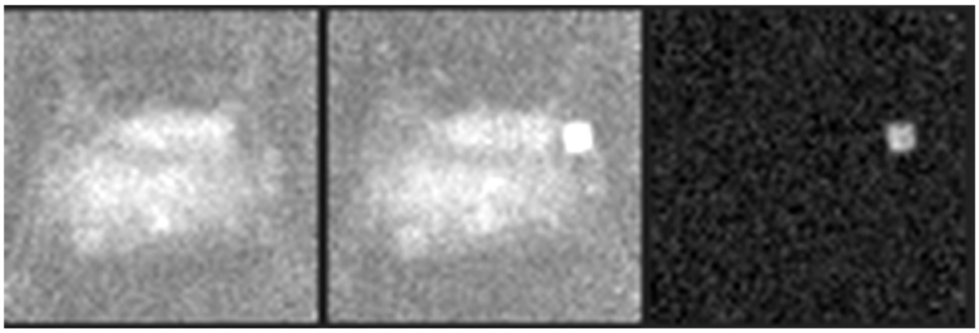

Figure 3.7: Comparisons between the X-Y slice from the mean scattering angles output images of the clean engine (left), the engine with a 10 cm side-length cube of Pb (middle) and the subtraction (right) [43].

six layers above the volume of interest and six layers below it. The system consists of long drift tubes with a length, diameter and spatial resolution of 365 cm, 5 cm and 450 μm, respectively. The detectors were arranged to provide information related to muon trajectories crossing through the system in the X-Z and Y-Z planes [43]. Figure 3.7 shows the results of testing the MST detector system to locate a high-Z material (Pb) hidden inside an engine of a small passenger car. The volume of interest was divided into a cubic-voxel with a side-length of 20 mm, and then each voxel was weighted by the mean scattering angle of each muon crossing the given voxel. After less than three hours of muon exposure time, the lead cube was located inside the engine using the scattering information of muons travelling through the inspected engine; however, hours of exposure time is not efficient for safeguard inspection purposes.

Additional Monto Carlo simulations were performed to understand the timescale of muon exposure needed to identify any threat embedded inside a cargo van. Several scenarios were simulated for a cargo van carrying a tungsten cube with side-length of 10 cm embedded between different non-hazardous materials. A 3D density map of the van's contents was obtained using the Maximum Likelihood/Expected Maximisation (ML/EM), which is detailed in [44]. The results of all scenarios were compared by using Receiver Operating Characterisation (ROC) curves, which plot the true positive (detection rate) against the false negative rate. On a statistical level, the ROC curves help to understand the capability of the detector system to locate the tungsten cube at several scanning times (see Figure 3.8). Statistically, this study showed that the MST detector system is able to identify the tungsten cube in 90 seconds.

In 2018, a prototype of a large portal muon detector was built by [45] to scan a whole standard 20-foot commercial container. Figure 3.9 shows the design of the detector setup suggested for the large muon portal project. The system consists of

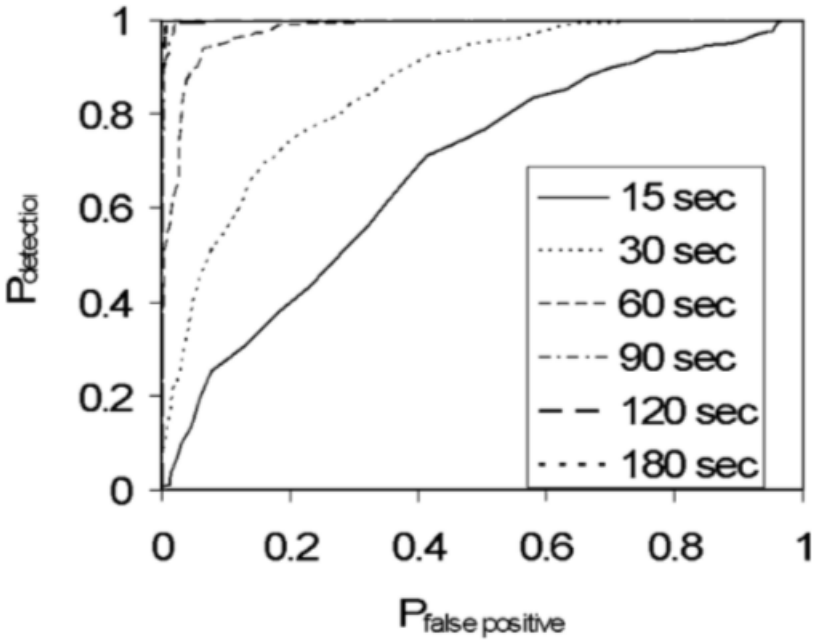

Figure 3.8: Comparison between ROC curves obtained from average scattering density information to detect a 10 cm side-length tungsten cube inside a cargo van for several hours of muon exposure time. The curves for 90, 120, and 180 seconds overlap, with an area under the curve almost equal to 1.0, indicating a very good identification level [43].

eight layers of position-sensitive modules that provide the muon hit positions in the X and Y planes. Each layer consists of six modules with a dimension of (1×3 m^2) and total active area of 18 m^2. The ability of the system to detect high-Z materials inside a large six-foot container was tested by placing a set of lead blocks with total size of 10 cm $\times$ 10 cm $\times$ 40 cm at $Z = 215$ cm. The scattering density information was calculated using the Point of Closest Approach algorithm (PoCA), which is explained in chapter 5 (see Section 5.1). Figure 3.10 shows the 2D tomographic images of the container's content at different planes along the vertical direction (Z). The lead cubes are clearly detected at the expected locations between 205 and 225 cm. For safeguard applications, it is important to determine how much data are needed to detect high-Z materials embedded inside an inspected container. Figure 3.11 indicates that 200,000 muon tracks is enough to flag the contents of the container with a density higher than expected. According to this study, the number of tracks can be achieved in $\backsim$ 4 hours of muon exposure time, which is too much time to scan a single container.

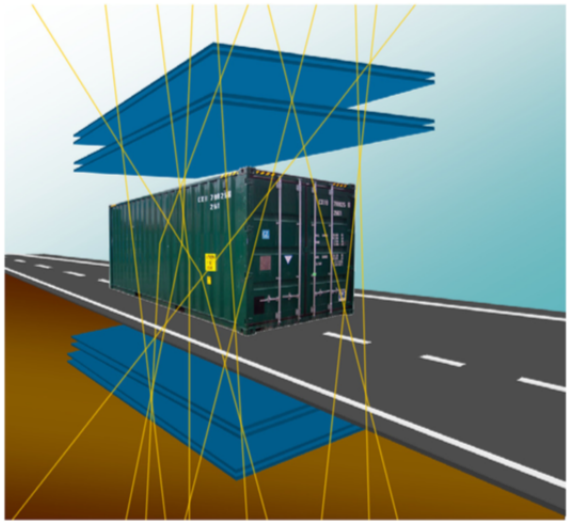

Figure 3.9: Schematic of the suggested design of MST for the muon portal project to scan shipment containers [45].

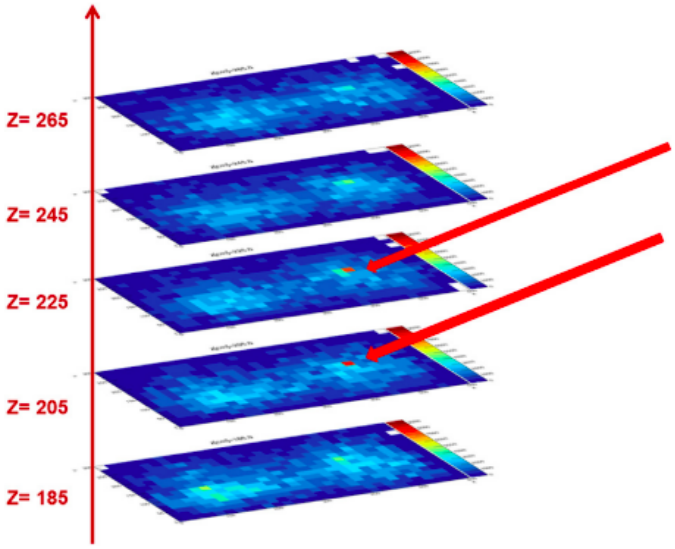

Figure 3.10: Comparisons between the 2D tomographic images of the container's contents in sections for the regions inside the container between 185 cm and 265 cm with a total of 80 cm in the vertical direction [45].

3.2.2 Building maintenance applications

The maintenance of civil construction is necessary to keep facilities safe and to mitigate any disturbance or issues in the future. For instance, defects in parts of steelwork configurations within Reinforced Cement-Concrete (RCC) bodies could cause disasters

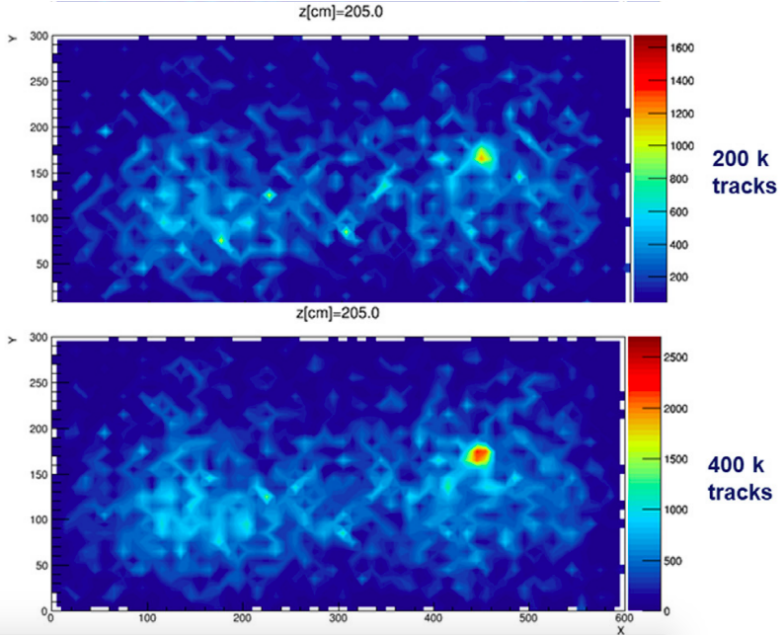

Figure 3.11: Comparisons between the X-Y slice of the reconstructed 2D images of the container's contents using 200,000 tracks (above) and 400,000 tracks (below) [45].

over time. Several non-invasive technologies have been applied to image/assess civil infrastructure bodies, such as the ultrasound method [46] and Ground Penetrating Radar (BPR) [47]; however, the penetration ability of these conventional methods through materials can be limited to a few centimetres. Recently, several research groups have applied the MST technique to scan rebars within RCC bodies, e.g. in [48].

In [49], simulations studies were performed to investigate the capability of the MST method to detect several common issues that might occur in RCC bodies. A few cases have been considered in this study, such as internal degradation within the concrete (voids) and corrosion of the iron rebars. Two identical muon tracking systems with a spatial resolution of 0.2 mm were placed above and below the volume of interest. Each tracking system consisted of multiple layers of a gaseous detector with an active area of 600 mm $\times$ 600 mm, providing muon trajectories in the X-Y planes.

Figure 3.12 shows the simulated module of the RCC structure, which was made of rebar with a length and diameter of 24 cm and 3 cm, respectively, embedded along the X-axis inside a concrete body with a dimension of 25 cm$\times$ 10 cm$\times$ 10 cm. The rust in the model was a composition of Fe_2O_3 with a density of 5.25 g/cm^3 and was placed in three regions as rings with a thickness that varied from 2.25 to 4.5 mm around the rebar. The density of the concrete and the normal steel rebar was 2.3 and 7.87 g/cm^3, respectively. This results in $\Delta\ \rho\ \backsim 2.6$ g/cm^3 between the normal rebar and the rusted

one.

The scattering densities within the volume of interest were reconstructed using the PoCA algorithm, which will be discussed in chapter 5 (see Section 5.1). The scattering densities were projected along the X- and Y-axis, and then each pixel in the 2D plane was weighted using the information of the projected angles (θ_x and θ_y). Figures 3.13 and 3.14 show the 2D reconstructed images of the normal rebar in (a) and the rusted bar in (e). The colour-scale bar represents the discriminator values of each pixel. Hence, these values were used to apply the Pattern Recognition Method (PRM) algorithm to generate scores of filtered discriminator values, called the PRM score.

A high PRM score of the inspected region means that the reconstructed image is more likely to be different from that of the normal image (a reference image). The PRM scores were produced by comparing the discriminator values of all regions in the reconstructed image of the inspected rebar (figure (e)) to the discriminator values of all regions of the reference image (figure (a)). Consequently, all pixels containing fewer discriminator values compared to the reference image were neglected by PRM. The image of the rebar was re-reconstructed according to the PRM scores, as can be seen in (figures (b) and (f)), and the neglected and approved pixels are shown in grey and red, respectively. The PRM scores of the rusted regions show the ability of the MST to detect any abnormality in the rebar, with a score of 1.48 and 4.45 when imaging defected rebars by corrosion with a thickness of 2.25 and 4.5 mm, respectively.

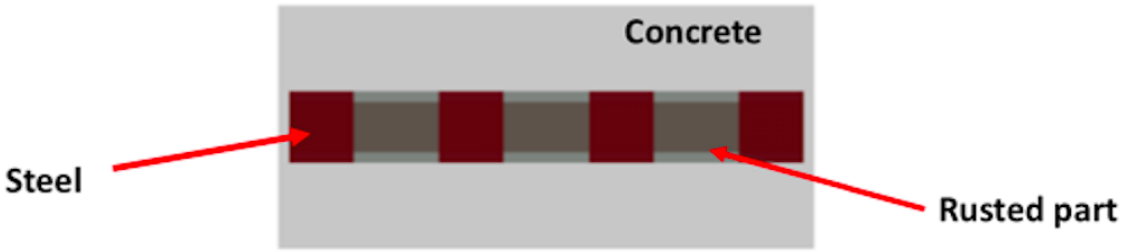

Figure 3.12: The module of the defective rebar was simulated and placed in the centre of a Reinforced Cement-Concrete (RCC) body, aligning it with its central axis [49].

3.2.3 Nuclear waste imaging and characterisation applications

Globally, radioactive waste materials come from different kinds of facilities, such as nuclear reactors, research and medical facilities. The chemical proprieties of radioactive waste can vary in terms of concentrations of radionuclides as well as in its physical form [50]. According to the safety rules of radioactive waste disposal and management, it is

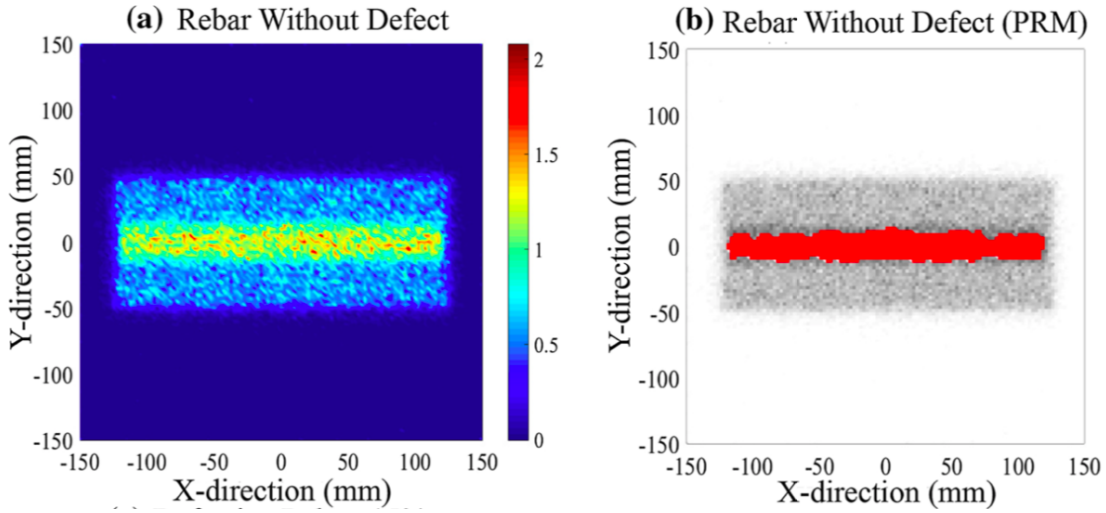

Figure 3.13: (left) the reconstructed image of a normal rebar inside a concrete matrix, (right) the PRM-filtered image of the normal rebar [49].

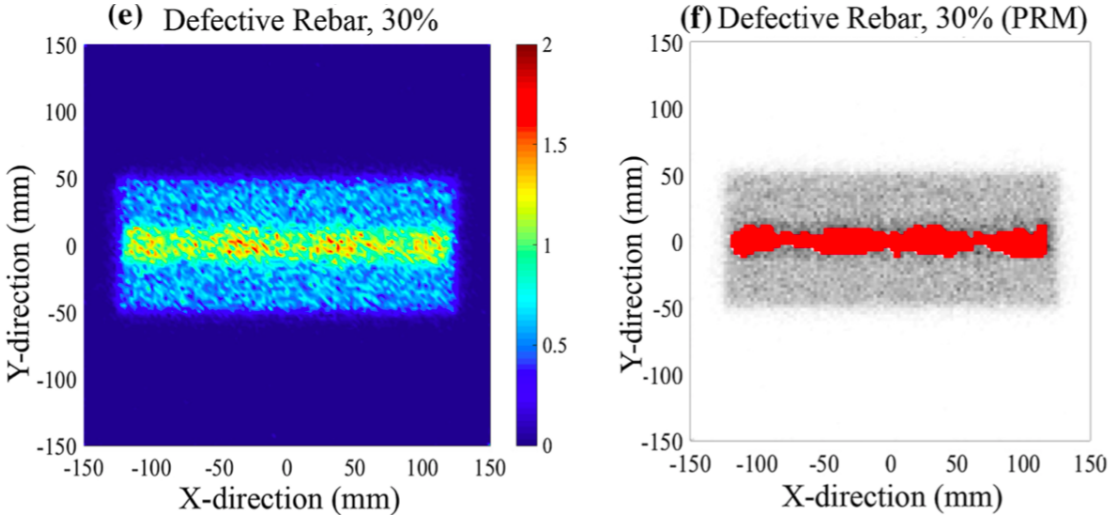

Figure 3.14: (left) the reconstructed image of a defective rebar with corrosion with a thickness of 4.5 mm, (right) the PRM-filtered image of the defective rebar [49].

required that radioactive waste should be characterised and classified before disposing of it in short or long term storage facilities [51]. The International Atomic Energy Agency (IAEA) has classified radioactive waste into six classes depending on the level of radioactivity. Hence, radioactive waste can be high-level waste (HLW), intermediate-level waste (ILW), low-level waste (LLW), very low-level waste (VLLW), very short-lived waste (VSLW) and exempt waste (EW) [50].

HLW composites have a large number of radionuclides and have a level of activity

($>$ 104-106 TBq/m^3) that is high enough to produce a significant amount of heat due to the radioactivity decay process [50]. For example, spent nuclear fuel and any other by-products of waste from nuclear fuel reprocessing are considered HLW. While, ILW is classified as any waste composites of long-lived radionuclides in an amount that requires a high degree of shielding to be isolated from the biosphere, such as alpha-emitting radionuclides. It also classifies any highly contaminated waste as ILW, such as parts of a reactor core, resins and filters that are used to treat the reactor water system. LLW composites of limited quantities of long-lived radionuclides have a relatively low level of activity or short-lived radionuclides with high levels of activity. LLW also contains contaminated materials that have been used during routine clean-up and maintenance operations at nuclear reactor plants, e.g. protective clothing, plastics and mops.

VLLW does not require high shielding, such as materials with low levels of activity that come from dismantling nuclear sites (soils, bricks, steel items and rubble) [50]. VSLW mainly contains radionuclides with very short half-lives, and they can be stored until their radioactivity decreases to the level of clearance. For instance, such materials come from research and medical facilities, e.g. ^{192}Ir. EW can be any waste that achieves the criteria for clearance and an exception from the regularity control of radiation protection rules, and they can be handled without protection.

Radioactive materials are usually disposed of and stored depending on the regulations and their class of radioactivity. In general, there are many nuclear waste packages designed to store or transfer specific classes of nuclear waste, and they can be either dry or wet storage. The wet storage facilities are usually contain water pools to cool down heat generated from HLW, while dry storage facilities use the natural air to dissipates heats [52]. Furthermore, nuclear waste packages vary in size, shape, shielding and thickness. Examples of typical small packages are shown in Figure 3.15, and they are used to accommodate LLW and ILW within concrete shielding. These small drums are usually made of stainless steel or carbon steel with a height and a diameter of 850 mm and 570 mm, respectively, for a 200-litre drum.

Larger nuclear waste packages have also been designed for safe transportation or the interim storage of HLW, such as spent fuel assemblies. As HLW generates heat, it might undergo cooling procedures ($\backsim$ years) before moving to dry storage facilities [50]; however, this procedure can be avoided with the availability of a self-cooling cask, such as CASTOR® (Cask for Storage and Transport Radioactive Material) [53]. Several CASTOR casks are designed and built in Germany by Gesellschaft für Nuklear-Service (GNS). Figure 3.16 shows three different designs of the CASTOR cask, namely V/19, V/52 and HAW28M, with a cylindrical body made of ductile iron. The V/52 Castor has been designed for the transport and storage of SNF assemblies that come from a

Figure 3.15: Examples of cylindrical drums with a capacity of 200 litres (left) with an internal diameter of 560 mm and a capacity of 400 litres (right) with an internal diameter of 770 mm used to store LLW and ILW. The 200-litre drum is made of stainless steel, and the 400 litre is made of carbon steel [51].

boiling water reactor (BWR) with a height of 455 cm and a total diameter of 244 cm.

The standards and modern regulations for disposing of and storing radioactive waste are well-understood. These regulations have been established to control and mitigate any potential hazard to the environment and public that might be posed by nuclear waste facilities; however, in the early nuclear era, the development of nuclear reactor technologies was dominant, and concerns about nuclear waste were considered insignificant [54]. Many old disposal sites have issues, such as poorly documented data about the disposed materials. This could include a lack of information about the concentrations and the form of the disposed radionuclides at the site. Moreover, it is possible that old packages could have a heterogeneous mixture of waste forms or classes. Hence, the retrieval of old nuclear waste packages is necessary to re-classify this waste appropriately according to modern regulations [54].

Several techniques can be used to characterise unknown radioactive or non-radioactive materials in old nuclear waste. The basic method of examining old waste packages is by opening them and examining the materials chemically and physically to

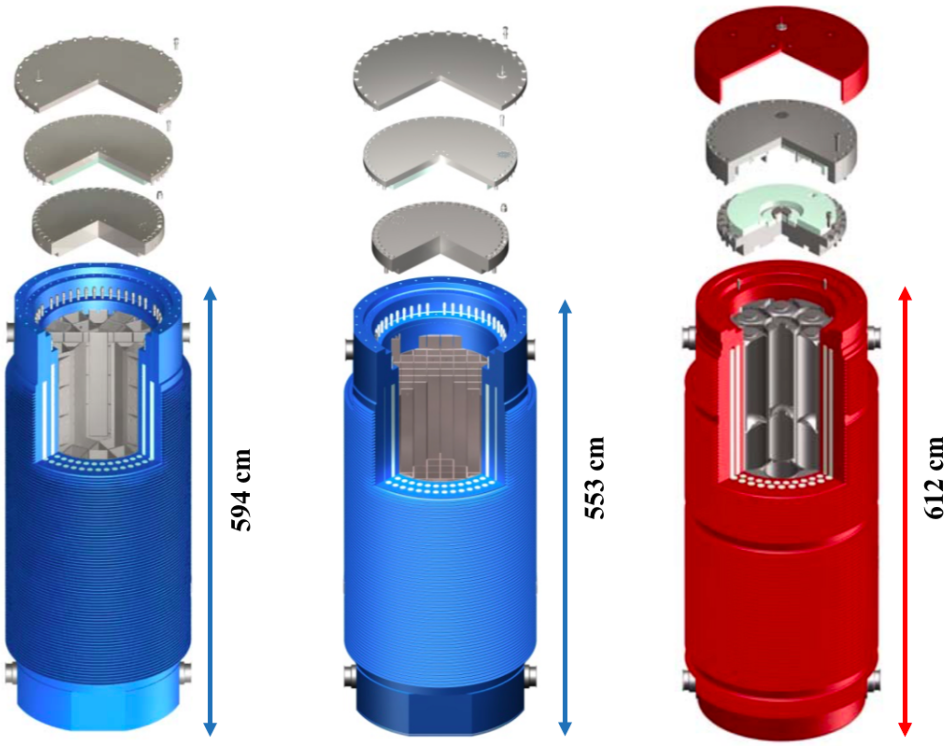

Figure 3.16: CASTOR casks are designed for specific types of fuel assemblies and HLW: a V/19 CASTOR cask (left) with a cavity diameter of 148 cm designed to accommodate up to 19 fuel assemblies from pressurised water reactors (PWR). In the middle, a V/52 CASTOR with a cavity diameter of 148 cm designed to accommodate 52 fuel assemblies from BWR. On the right is the high-active waste (HAW) CASTOR for HLW from the reprocessing of SNF with a cavity diameter of 135 cm [53].

measure their activity. This method is classified by IAEA as destructive assay (DA) [55]. To avoid the risk of exposure to radioactive materials and the cost of opening nuclear waste packages, non-destructive techniques are more practical in the characterisation of well-shielded nuclear waste. The ways to check nuclear waste packages non-destructively could be either a non-destructive examination (NDE) or a non-destructive assay (NDA) [55]. The NDE method is used to examine the mechanical and physical structures of the package. NDA is a characterisation system applied to determine the concentration of radionuclide activity in a waste package.

NDA systems can be either active or passive techniques. Active techniques involve artificial particle sources to probe the inspected object, e.g. X-ray radiography and the neutron induced-fission imaging technique. X-ray radiography is sensitive to the thickness and the density of the object it is crossing. Hence, a high-energy source is used that is placed close to the inspected object, and a detector is placed on the

opposite side to detect the photons that manage to cross the object. By using the information of transmitted/attenuated photons, a dense or high-Z material can be located inside nuclear waste packages [56]. Induced-fission imaging can also be used to identify specific materials, such as plutonium and uranium, as the neutrons could induce fission in both materials. Gamma-rays are emitted as a result of the nucleus fission process with a unique energy for each material. Thus, depending on the energy of the emitted gamma rays, the material can be identified; however, these techniques are less efficient due to high costs, in addition hazard might occur due to exposure to the artificial source used.

A passive technique uses information of radiation and/or heat emitted by the object and does not require any artificial particle sources, e.g. calorimetry. Briefly, the calorimetry technique exploits the fact that HLW generates heat inside the package, and the amount of heat can be used to estimate the total radiation rate of the disposed HLW. Measuring radiation information produced as a result of the natural decay of uranium and plutonium is another example of passive techniques. For example, the energies of detected gamma-rays can be used to determine the material; however, these techniques are less efficient, especially with the presence of high-shielding materials, as gamma-rays could be absorbed by the shielding material. The MST technique is considered to be a passive method as it uses cosmic muons to scan the inspected object. In addition, MST can overcome the limitations of the conventional methods because cosmic muons can cross through the high-shielding of nuclear waste packages. Moreover, MST is sensitive to high-Z materials, such as uranium, plutonium and lead, so it can locate well-shielded materials.

In the past decade, there has been an increase in the number of research groups and commercial companies that develop and commercialise the technology of MST system in nuclear waste imaging. On a commercial level, Lynkeos Technology Ltd developed Muon Imaging System (MIS) for imaging services like nuclear waste containers [57]. Lynkeos Technology based on the UK and it was started as a spin-out by a group of nuclear researchers at the University of Glasgow. Figure 3.17 illustrates the commercial Lynkeos MIS system, which is composed of four detector modules. Two modules are positioned above the volume of interest, while two modules are placed below it. These detectors are used to reconstruct the trajectories of muons as they pass through the volume of interest. Each detection plane consists of a single layer of plastic scintillating fibers arranged in orthogonal directions. In each direction, there are two overlapping layers of fibers, with each layer containing 512 fibers, resulting in a total of 1024 fibers for each detection layer. Each module provides information about the muon signals in the X-Z and Y-Z directions, resulting in a total of 8 muon

Figure 3.17: The MIS system, constructed and installed at the Lynkeos facilities, consists of four detector modules, each with an active area of 106.6 cm × 106.6 cm [57].

hit trajectories corresponding to the 4 detector modules. An example of imaging high-Z materials embedded inside a 500-liter ILW waste drum using the MIS is shown in Figure 3.18. In the experimental setup, the system utilized a total of approximately 25 million cosmic muons to image a small cylinder of uranium with a diameter and height of 2 cm and 3 cm, respectively (see Figure 3.18 (a)). Additionally, the system was tested using small pieces of lead with dimensions of about 9 cm × 4 cm × 2 cm (see Figure 3.18 (b)). In both cases, the system successfully reconstructed an image of the 500-liter drum, providing a clear image of the internal structure containing the small pieces of lead and uranium [57].

In [58], a simulation study was performed to investigate the ability of the MST method to image high- and low-Z materials inside small steel drum (26 litres). A variety of several materials with different shapes and sizes was embedded within concrete shielding inside the drum. Figure 3.19 shows the simulated drum containing a cylindrical uranium rod with a radius and height of 1 cm and 10 cm, respectively. A sheet of uranium was also simulated with a dimension of 0.5 cm × 10 cm × 10 cm. Several tungsten coins with different sizes were embedded within the concrete matrix between

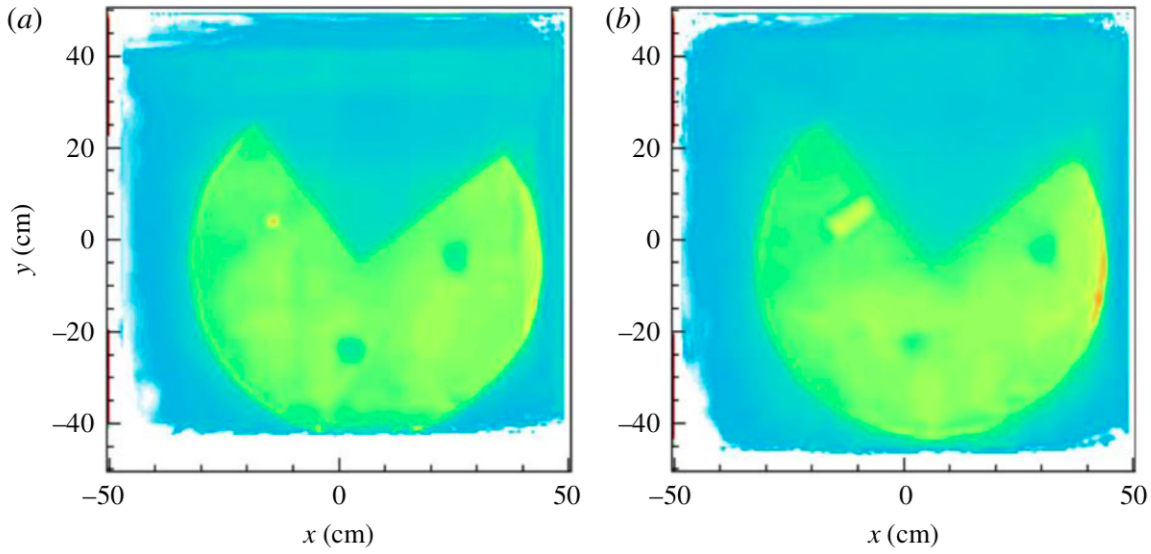

Figure 3.18: The X-Y slice outputs of the uranium cylinder (left), and the lead pieces (right) inside a 500-litre ILW drum using the Lynkeos MIS system [57].

the uranium rod and an enclosure filled with air. The simulated muon detector system used in this study consisted of two tracking systems with a total of 12 layers of Resistive Plate Chambers (RPCs), six layers above the inspected drum and six layers below it. Each system provides six muon trajectories positioned in the X-Y plane, three positioned in the X-axis and three positioned in the Y-axis.

The RPCs have an intrinsic spatial resolution of 450 μm and total active area of 100 cm $\times$ 100 cm. Figure 3.20 shows a 3D reconstructed image of the inspected drum, indicating all the hidden objects except the smallest coin of tungsten (1 cm radius and thickness). The 3D image was reconstructed using data collected over a span of 2 weeks. During this time, the drum was scanned in four distinct positions: its default orientation and three subsequent rotations around the x-axis, each separated by 90°. The image of the drum content was reconstructed using the binned clustering algorithm (BC), which is explained in detail in chapter 5 (see Section 5.1). Additional simulations of uranium sheets with a thickness of 0.5 cm and several side-lengths ranging from 4 to 10 cm were performed to understand the ability of MST to reconstruct the target objects [58]. An edge finding method was applied to measure the size of the reconstructed uranium sheets. Hence, the ability of MST to reconstruct the hidden object can be measured in terms of size resolution. This study showed that a 5 mm thickness of uranium sheets could be reconstructed with a resolution of 1.2 ± 0.37 mm. Figure 3.21 shows the reconstructed sizes of the uranium sheets with a thickness of 0.5 cm and side-lengths ranging from 4 to 10 cm as a function of the

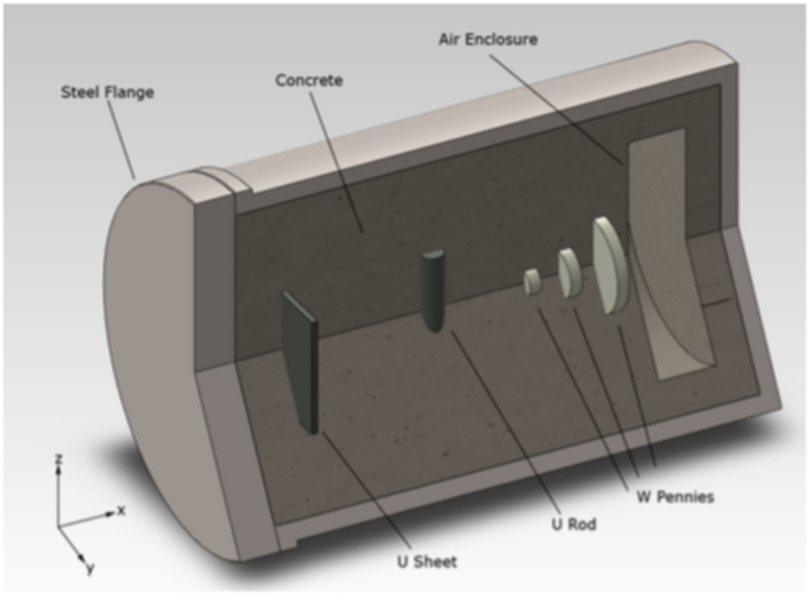

Figure 3.19: A simulated drum of a standard ILW nuclear package with a length and a diameter of 50 cm and 26 cm, respectively. The drum contents are a variety of simulated high-Z and low-Z materials. The high-Z materials are simulated in different shapes (coins, sheets and rods). All the drum contents are embedded in concrete shielding [58].

real simulated sizes. After 32 days of muon exposure time, the results showed a good agreement between the reconstructed and the real sizes of the target uranium sheets.

In some cases, many countries store LLW and ILW in steel packages with added pure bitumen to fill the empty volume, or sometimes, they mix the waste with bitumen. When bitumen is irradiated by the radioactive materials, this leads to the production of hydrogen inside the drum [59]. Hydrogen combines to form gas bubbles, leading to the swelling of the drum's contents with a possibility of leaking radioactive waste to the environment. In [60], the ability of the MST technique to locate low-density materials (gas bubbles) inside nuclear waste packages was tested. Various sizes of cylindrical gas bubbles were simulated and placed in the centre of a smulated waste drum. The dimensions of the simulated gas bubbles were between 50.27 and 21237.17 cm^3, with a radius and length of 2 cm and 4 cm, respectively, for the smallest bubble.

The gas bubbles were simulated with a density of 0.0012 g/cm^3, and the bitumen was replaced with concrete with a density of 2.3 g/cm^3. The muon detector used in this study consisted of two identical tracking systems with six layers of RPCs above the simulated drum and six layers below it. Each tracking system consisted of three layers providing muon trajectory information in the X-plane and three layers providing

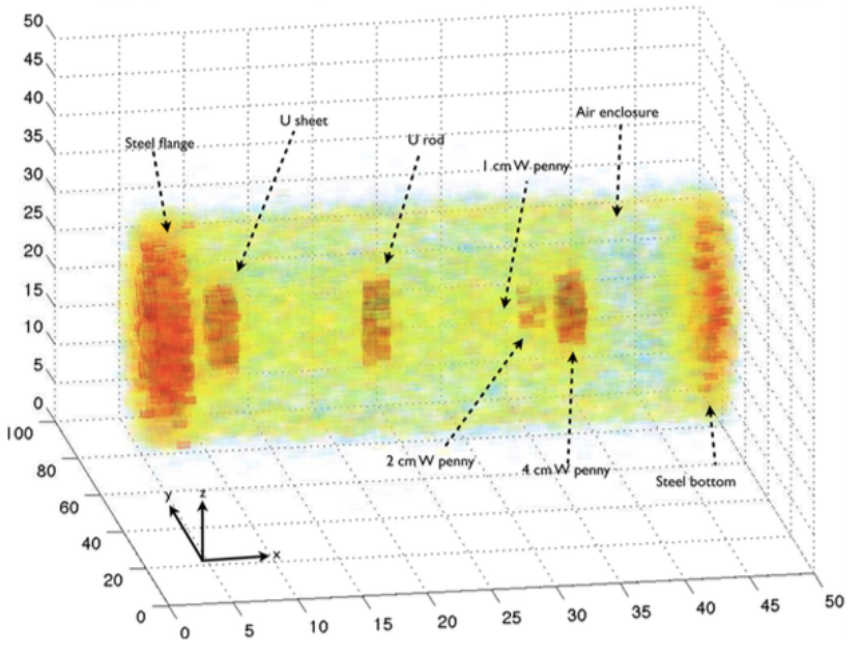

Figure 3.20: A 3D reconstructed image of the simulated nuclear waste drum. The contents of the drum are clearly visible apart from the tungsten coin with a thickness and radius of 1 cm. The light-yellow regions represent the concrete matrix [58].

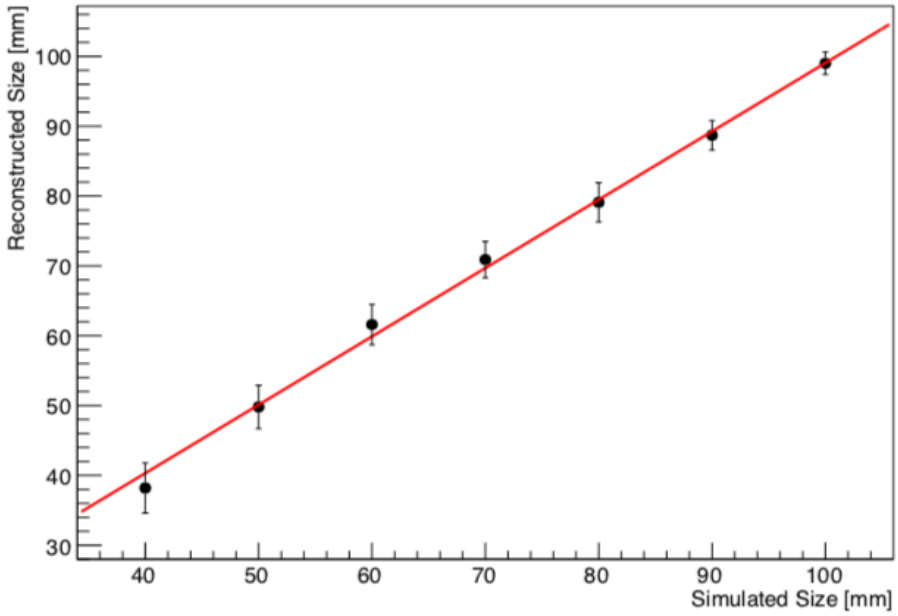

Figure 3.21: The reconstructed sizes of uranium sheets with a thickness of 0.5 cm versus the real simulated sizes with a thickness of 0.5 cm and side-lengths between 4 cm and 10 cm. The muon exposure time was equivalent to 32 days [58].

muon trajectory information in the Y-plane [60].

The drum's contents were reconstructed using the BC algorithm, which will be discussed in section 5.1.3, as can be seen in Figure 3.22, in which higher discriminator values correspond to low-Z materials. The distributions in Figure 3.22 represent the average discriminator of the drum's contents when filled with gas and concrete with values of $\mu_{discr} = 10.244 \pm 0.003$ and $\mu_{\text{discr}} = 10.069 \pm 0.003$, respectively [60]. These results were produced using 159 million simulated muons, and their momentum was considered as known and without any smearing.

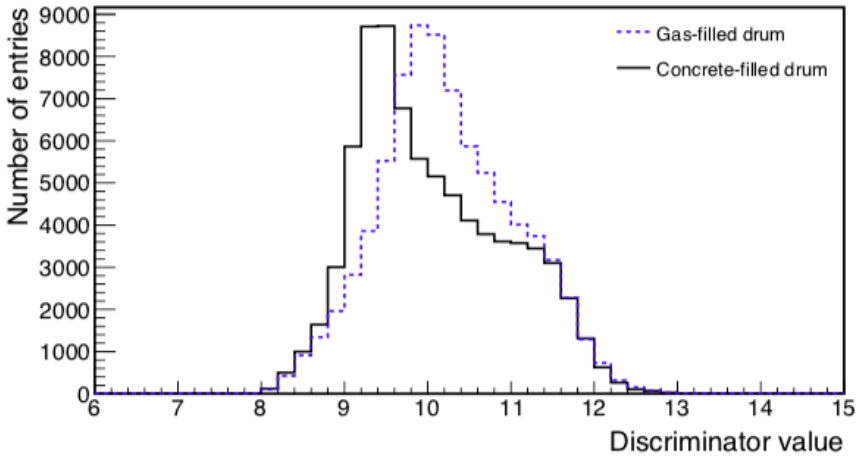

Figure 3.22: The discriminator distributions obtained using the BC algorithm of the drum contents. The black solid line represents the discriminator output when the drum is filled with gas, and the blue-dashed line represents the discriminator when the drum is filled with concrete. The higher discriminator corresponds to the lower density material [60].

On a quantitative level, comparing the mean discriminator values of the drum contents with gas bubbles to the drum contents without bubbles helps to locate low-Z materials inside the drum. Figure 3.23 shows the results of three studies assuming the presence of gas bubbles in two scenarios and one scenario with the absence of gas bubbles. The mean discriminator values when locating 4.4 litres of gas bubbles in the centre of the drum exceeded the discriminator values of the concrete matrix [60]. There was an increase in the discriminator values in the regions that contained two bubbles with a volume of 2.2 litres inside the drum. The study showed that measuring the volume of gas bubbles of 2.0 litres or more using MST is possible with a relative uncertainty of 1.55 ± 0.77 [60].

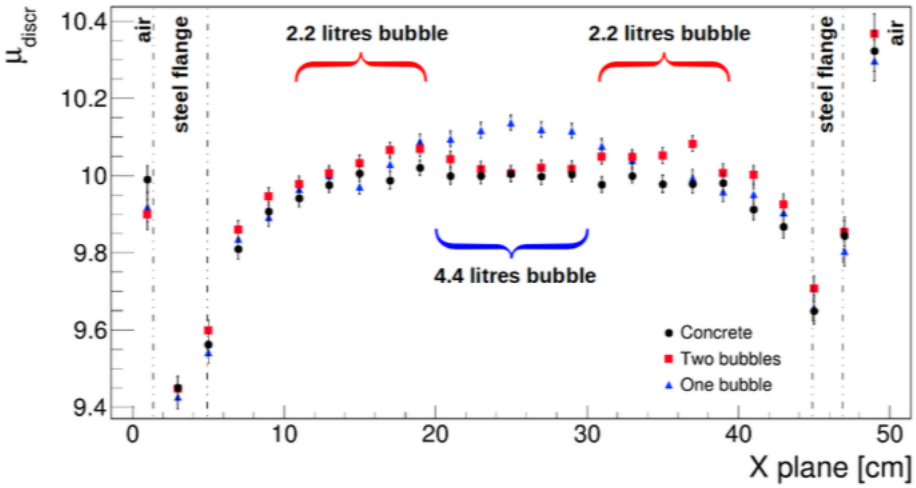

Figure 3.23: The mean discriminator values as a function of the position along the x-axis of three simulations of drums containing: an empty concrete-filled drum, a concrete-filled drum with a 4.4-liter gas bubble placed in the centre of the drum, and a concrete-filled drum with two equally-sized gas bubbles placed in different positions inside the drum [60].

3.3 Summary

Many limitations of conventional imaging methods have been overcome with the development of MT technology. Within the last decade, MT has been extensively used in the applications of archaeology, volcanology, civil engineering and nuclear waste characterisation. Investigating well-shielded objects ideally requires a non-destructive method, especially when dealing with hazardous materials, such as radioactive materials in nuclear waste packages. Using a non-invasive technique to assay nuclear waste packages could reduce the cost involved in opening the investigated packages as well as could mitigate any potential risk of being exposed to ionising radiation. MST is a non-destructive imaging method that has proven valuable for imaging hidden objects in many applications, such as nuclear safeguards and nuclear waste characterisation. Muon radiography has also contributed on the understanding of the structural densities of inaccessible structures, e.g. volcanoes. In 2017, a large void was discovered inside the pyramid of Khufu through muon radiography using the muon flux information that crossed through the pyramid.

Many studies have already shown the possibility of using the MST method to overcome challenges in the field of nuclear waste management. Even when using the

current state-of-the-art muon tomography, many aspects of this technology still require development and research to overcome the current limitations of MST. In particular, in classifying nuclear waste and imaging low-Z materials.

Chapter 4

Simulations and data analysis

As it is difficult to have access to real nuclear waste, all data presented in this chapter is based on Monte Carlo (MC) simulations. These data have been taken using a simulated muon scattering tomography (MST) system. This system is simulated with a detector setup that matches the physical properties of a real mobile MST detector. The mobile MST system, briefly described in section 4.1, was built for the CHANCE Horizon-2020 project [61] to address unsolved issues related to the characterization of nuclear wastes inside a different types of waste packages. The CHANCE project applied several non-destructive assay (NDA) techniques, including muon scattering tomography. Thus, performing simulations is useful to show feasibility studies before spending efforts on the MST system.

This Chapter describes the simulation method in detail (section 4.2), including simulation of cosmic muons arriving from the atmosphere, tracking systems, and muon trajectory track fitting. This section will also describe the simulations of two types of nuclear waste packages, a small-steel drum and a large nuclear waste cask, namely, a CASTOR V/52.

4.1 Muon detectors: The CHANCE system

The principle of muon scattering tomography requires measuring the space coordinates of muon trajectories that cross the volume of interest. Hence, a set of muon detectors is positioned above and below the volume of interest. As cosmic muons are charged particles, they can be detected by several kinds of detectors, including gaseous de-

tectors. The detection setup in the CHANCE system is based on multiple layers of gaseous detectors with a total sensitive area of approximately 1.8 m× 1.8 m. The gaseous detectors used in the system are a combination of Drift Chambers (DCs) [62], and Resistive Plate Chambers (RPCs) [63]. Additional polystyrene scintillator panels are used as triggers, indicating a signal when muons cross through the tracking system.

4.1.1 Resistive plate chamber

The RPC module used in the CHANCE system was built by the University of Bristol, with a spatial resolution of $\backsim$ 0.35 mm [63]. It designed in a rectangular shape with dimensions of a 180 cm × 58 cm. The main detection unit in the detector is a glass resistive plate chamber which contains a gas-mixture with a gap of 2 mm. The gas gap is protected by two sheets of glass placed above and below the glass spacer, (see Figure 4.1). The chamber is flushed with a gas mixture consisting of $\backsim$ 95% of Tetrafluoroethane (Freon), and $\backsim$ 5% of Iso-butane. A printed circuit board (PCB) containing 320 strips with 1.5 mm pitch is glued on the top of the chamber to provide the readout position information in one direction. The RPC contains two electrode plates above and below the gas volume, high-voltage is applied between the two electrodes. As muons are charged particles, they hence ionise the gas mixture inside the RPC. This results in a signal induced on the strips due to electrical charge drifting to an electrode plate. The position of the crossed muons through the RPC can be extracted by collecting the signal on several strips.

4.1.2 Drift chamber

The DC module used in the CHANCE system was built by the Atomic Weapon Establishment (AWE) in collaboration with University of Manchester, and operated by the University of Sheffield, with a spatial resolution of $\backsim$ 2 mm. The drift chamber was designed in a rectangular-shape with dimensions of a 180 cm × 60 cm. The main unit of the drift chamber consists of two PCB boards with cathode strips, separated by a 15 mm gap. The PCB boards are attached to an aluminum support frame with thickness of 12.5 mm. In the centre of the unit, a single anode wire is positioned along the length of the DC, which makes a 625 mm horizontal distance between the anodes of the neighbouring DCs. The anode wire is operated at voltage of $\backsim$ 6000 V, while the cathodes are operated at voltage of $\backsim$ 4000 V. The gas gap between the PCB boards is flushed with a gas mixture consists of mainly argon (92.5%), carbon dioxide (5%), and methane (2.5%). An interaction within the gas mixture medium occurs when a

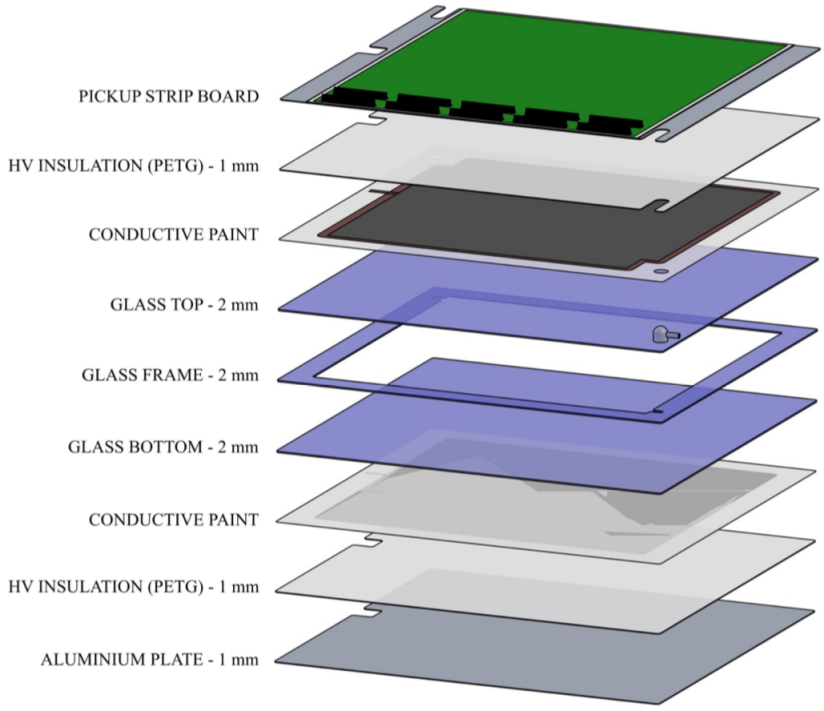

Figure 4.1: A disassembled diagram indicating the structure of the RPC detector [63].

muon passes through the DC, resulting in the liberation of electrons. The liberated electrons drift toward the anode, leading to an induced signal within the anode that can be detected by the system's electronics. The drift time is defined as the time difference between the trigger signal and the time taken for the electrons to reach the anode, (see Figure 4.2). The information of the drift time (T_d), and the drift velocity (V_d) can be used to determine the muon hit position (x) in one direction $x = T_d \times V_d$. It is expected that interactions of muons occurring close to the wire will have a short drift time, given that the electric field near the anode is strong and the velocity is at its maximum, (see Figure 4.2).

4.2 Monte Carlo Simulations

In muon tomography/radiography applications, imaging structures located in inaccessible or hazardous sites using computational simulations is a very useful tool to understand both the efficacy of the detectors and the feasibility of the project. Additionally, accurate computational simulations of proposed experiments reduce the cost and minimise exposure to potential hazards that might occur during the real experi-

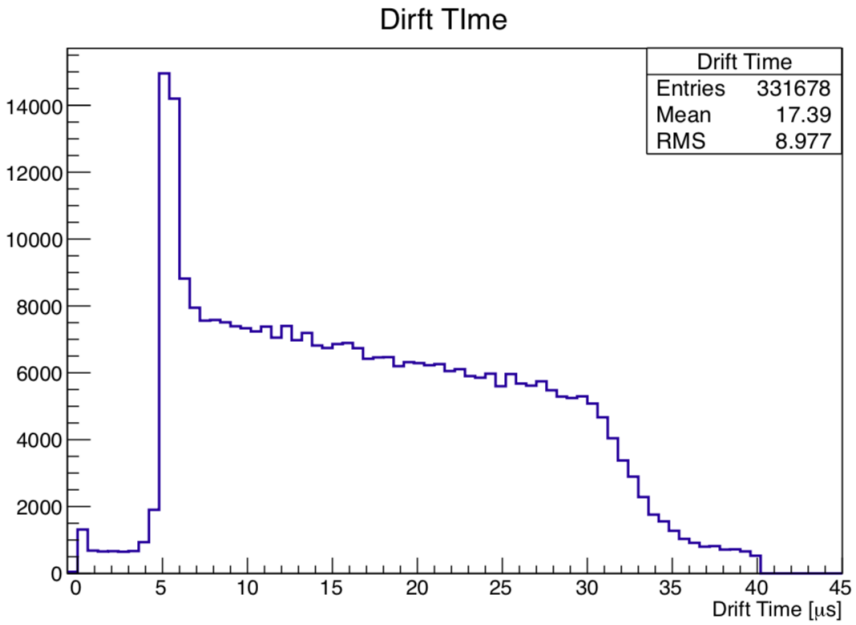

Figure 4.2: From [62], an example of the drift time distribution across multiple layers of drift chambers. The distribution peaked after 5.1 μ s, representing a delay time from the triggers, was set to electronic readout [62].

ment. Cosmic muons simulated using MC simulation start by considering the characteristics of muons at specific coordinates, such as altitude and latitude. This results in determination of the distributions for muon trajectories and energies, and from these distributions the initial state for each muon can be drawn randomly. This can be established using many available cosmic ray libraries in high-energy physics tools, (see below). Then, the subsequent phase of the simulation involves transporting the initialized muons in which this process is managed by common transport software, (see below).

Simulations of the MST system were performed using a cosmic ray simulation platform (CRESTA) [64] built on the Geant4 high-energy particle physics simulation toolkit [65]. The Geant4 toolkit is developed for the simulation of the interactions of particles with matter, including scattering, Bremsstrahlung, ionisation, and pair production processes. Geant4 can be used to design complex structures for experimental prototypes by combining many simple geometrical shapes. For example, any material can be placed with chosen volume at any position in space with its characteristics parameters being defined such as density and atomic number. Based on the material data, the differential cross-sections for several muon interactions, e.g. ionization,

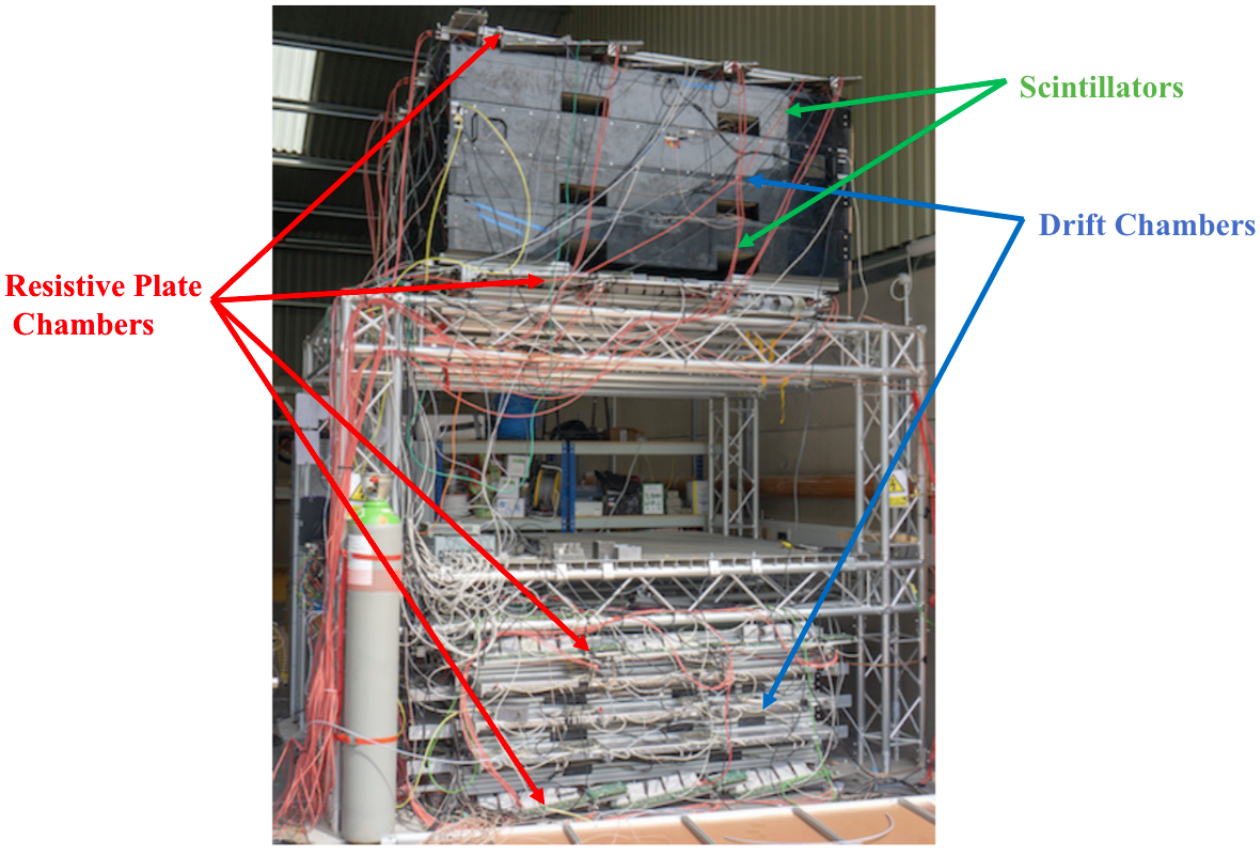

Figure 4.3: The CHANCE muon scattering tomography system. Two tracking systems are shown above and below the volume of interest. Each tracking system consists of 4 layers of RPCs, and 6 layers of DCs. The plastic scintillator panels are also shown in the upper system.

can be computed for muons with different energy levels in matter. Hence, tables representing the average energy loss can be generated by integrating the cross-sections. Subsequently, the energy loss during transport can be derived from these tables.

A simulated detector is configured to capture charged particles, such as muons. The design of a charged particle-sensitive detector can be constructed to mirror the actual detector and positioned at any point in space. The actual detector properties such as the spatial resolution can be set by adding a smearing factor to the MC truth. To simulate a detector with an efficiency that matches the real detector, a fraction of the detected muons in the detector structure is discarded.

In this thesis, cosmic muons were generated by the cosmic-ray shower library (CRY) [66]. The CRY software developed a model of the Earth's atmosphere and used

MCNPX [67] to simulate primary protons with an energy range between 1 GeV and 100 TeV at the top of the atmosphere. These simulations generate a shower of secondary particles, including cosmic muons. The energy distributions of the simulated cosmic muons were benchmarked against data of published cosmic muon measurements, see Figure 4.4. Since the distributions of cosmic ray particles depend on the elevation, the particle showers are provided in the CRY library at three specific altitudes. The available altitudes are at sea level, 2.1 km, and 11.3 km. All the distributions of the cosmic muon in this thesis were chosen to be at sea level elevation.

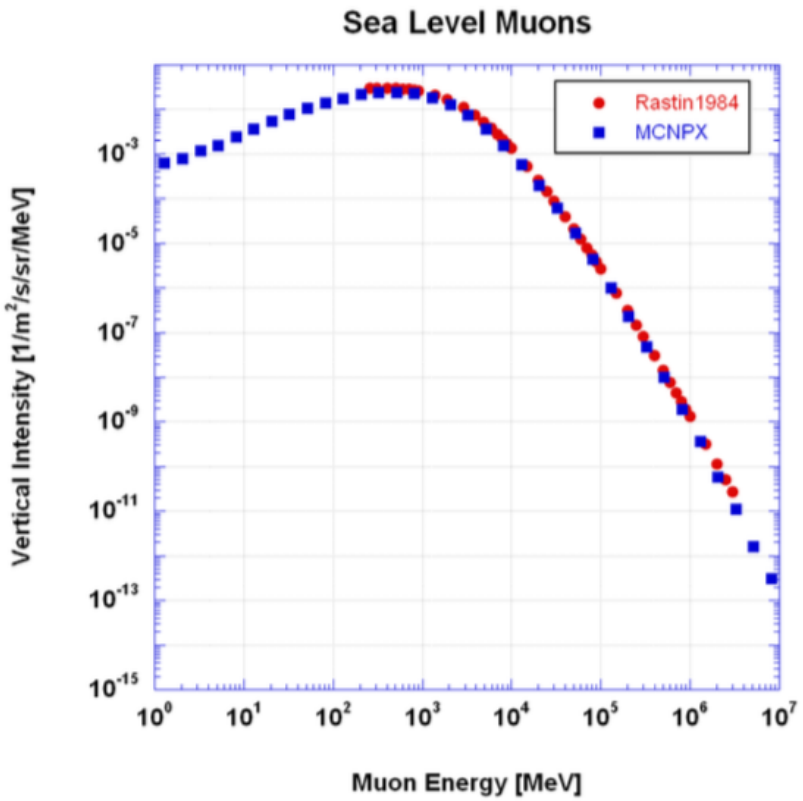

Figure 4.4: The muon spectrum, as obtained by using Monte Carlo simulations in blue squares. The red squares show the data muon spectrum measured by [12]. Both data show the muon spectrum at sea level [66].

4.2.1 The MST detector system

As explained in section 2.4.3, muon scattering tomography requires two tracking detectors to register the incoming and outgoing muons. The system consists of two identical

detector systems placed above and below the volume of interest with a gap of 105 cm when investigating the small cemented-matrix drum. The two tracking systems are placed with a gap of 580 cm apart when investigating the large CASTOR cask.

Each tracking system is arranged in 10 layers: six layers of Drift Chambers (DC) and four layers of Resistive Plate Chambers (RPC) with spatial resolutions of ~ 2 mm and $\sim$ 0.35 mm, respectively (see Figure 4.5). The 10 layers detectors are arranged to provide muon trajectories in the x and y planes: five layers placed in the X-Z plane and five layers are rotated by 90 degrees to provide muon hits in the Y-Z plane. The RPCs layers were placed in two pairs, with a vertical distance of 1151.6 mm, and the spacing between the X-Y planes was 50.8 mm in each pair. The DCs layers were placed in three pairs with vertical distance of 325 mm, and the spacing between the X-Y planes was 65 mm in each pair.

The detectors record muon hit position information, while the scintillator detectors provide a trigger of when a muon has passed through the system. The RPCs and DCs detectors were simulated with structures and dimensions that match the actual sizes of the real detectors. The structures of the real RPCs and the DCs detectors are briefly described in this chapter (see Section 4.1). This simulated system will be used to reconstruct a variety of materials which have different atomic numbers embedded inside two different types of nuclear waste packages with different shielding types and sizes.

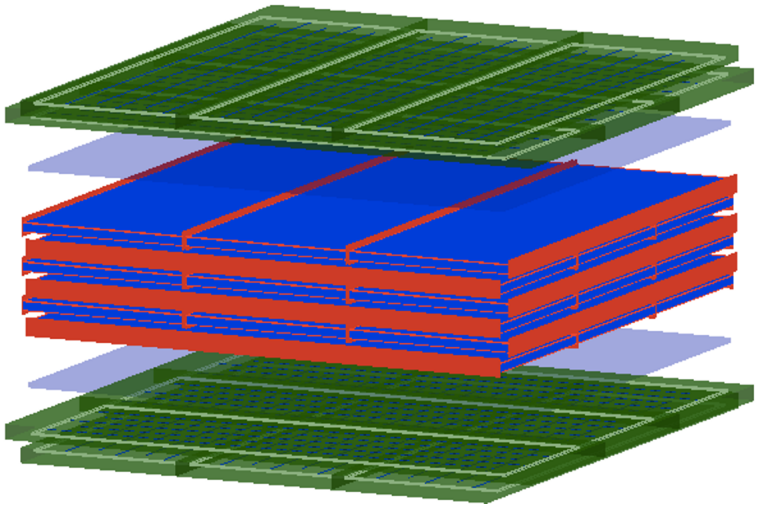

Figure 4.5: Diagram of the simulated tracking system with active area of approximately 2 m $\times$ 2 m, indicating 4 layers of RPCs (in green) and 6 layers of DCs (in blue and red). The light blue panels represent the scintillator triggering system.

4.2.2 Track fitting

Since cosmic muons arrive at the detector from different angular directions, there is the possibility to detect multi-muon events, in which multiple muons might be detected after a single trigger event. In reality, these multiple muon tracks can be identified by doing all possible linear fits of the hit positions in the detector layers. The best track fits can be then distinguished as the most likely real muon tracks. At the simulation level, multi-muon events are not created, therefore, each event in simulation corresponds to a single muon. It is possible that muons experience a few scatters with the detector structures, however, these scatters are neglected. Therefore the muon tracks that cross through the detector layers are approximated as straight lines. Consequently, a straight line is fitted between the muon hit positions in the detector layers, thus the incoming and outgoing muon tracks can be reconstructed. The tracks of incoming and outgoing muons are used to measure variables like muon scattering angle and offset of the muon path after traveling through the investigated volume.

The hit positions of muons in the detector layers were stored and analyzed using a ROOT program [68]. The track fitting method is used in [69] for fitting 3 muon hit points in a smaller muon detector system. The detector system described in section 4.2.1 provides 10 points on X-Z and Y-Z planes of the muon hit positions for the upper detectors (4 points on RPCs and 6 points on the DCs). For each muon, the total hit points obtained by the whole system is 20 points in the X-Z and Y-Z planes. In order to verify that a correct muon track is present, a straight line fit is performed through each 5 hit points in the upper detectors in the x-direction. Similarly, the muon track in the y-direction was also checked by performing a straight line fit through every 5 points in the y-direction in the upper detectors. This step is also repeated separately for the 5 muon hits in the x and y directions for the lower detectors. A further condition on the fit is applied to confirm the muon track which only considers 5 points fits with a χ^2 value lower than a cutoff value (2000). The cutoff value of 2000 is associated with the chance detectors system. The default cutoff of 2000 was chosen based on graphs that plot the differences between the MC true and the reconstructed direction or location. Then, all the combined 20 hit points in the x and y directions for both upper and lower detectors are fitted simultaneously. The condition of χ^2 of the final fit between the upper and lower hit points was also applied, in which all tracks with χ^2 value greater than the cutoff are neglected. The combined tracks work according to the assumption that the upper and lower tracks share a point called a vertex.

The hit positions are fitted with 7 parameters which are: 3 positions of the vertex in 3D coordinates, 2 parameters for the track slopes for the upper and lower tracks

in the x directions, and 2 parameters for the track slopes for the upper and the lower tracks in the y-direction. This is obtained by defining an energy function (E) as follows:

$$E = E_x + E_y \tag{4.1}$$

Where E_x and E_y the energy function in the x-plane and y-plane, respectively. The (E_x) is given by:

$$E_x = \sum_{i=1}^{5} \frac{(h_i - (v_x + k_{u,x} \cdot (z_i - v_z)))^2}{\sigma_{h_i}^2} + \sum_{i=6}^{10} \frac{(h_i - (v_x + k_{l,x} \cdot (z_i - v_z)))^2}{\sigma_{h_i}^2} \tag{4.2}$$

where i is the number of muon hit positions, h_i is the measured hit positions, $k_{u,x}$ and $k_{l,x}$ are the track slopes in the x-plane for the upper and lower detectors, respectively, v_x, v_y, v_z are the vertex positions in 3D dimension. While z_i, and σ_{h_i} are the detector position in the z-plane and the error in the measurement of h_i, respectively.

Despite the inaccuracy in the assumption of the single scattering vertex between the upper and lower tracks, this was seen as a useful approximation. Figure 4.6 indicates the principle of this assumption (single vertex) and is detailed in section (5.1.1).

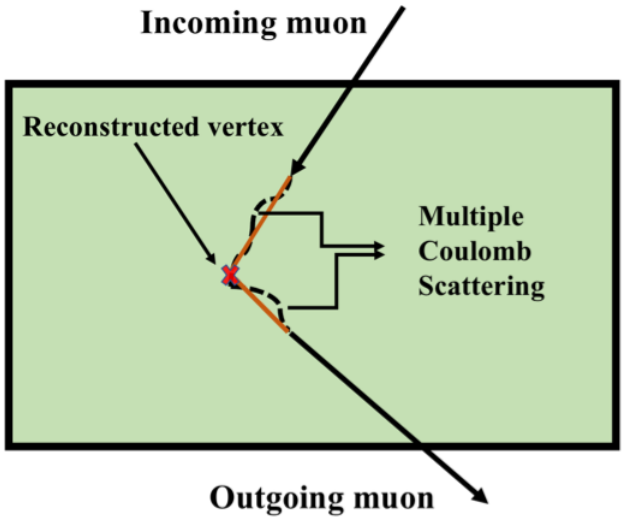

Figure 4.6: Schematic showing the principle of reconstructing the common point (vertex) between the incoming and outgoing tracks.

4.2.3 Simulation of Nuclear Waste Packages

The algorithmic methods detailed in section 5.1 are applied to the MC simulations to investigate their performance in distinguishing high-Z materials stored inside different

shielding matrices. Two nuclear waste packages were considered in this study: a small cemented-matrix nuclear waste drum and a large ductile-iron shielded V/52 CASTOR cask.

The small waste drum simulates the disposal of a mixture of radioactive wastes surrounded by a concrete matrix. The drum is made of steel ($\sim$ 92% iron and 2% carbon) of 96 cm length and 57.4 cm diameter. It is filled with concrete to a total diameter of 52.4 cm (see Figure 4.7). The density of simulated stainless steel and concrete are 8.05 g/cm^3, and 2.3 g/cm^3, respectively. The properties of the materials used to build the drum were taken from the Geant4 database.

To understand the effects of shielding thickness on the algorithmic outputs, a large V/52 CASTOR cask with denser shielding type has also been simulated (see Figure 4.8). The cylinder-shaped V/52 cask is made of ductile-iron ($\sim$ 94% iron, 0.033% carbon, 0.004% copper) with a density of 7.1 g/cm^3, a height of 5.54 m and a total diameter of 2.44 m. A cavity of 1.42 m diameter and 4.55 m height inside the centre of the cask is designed to accommodate the baskets for the fuel assemblies, which are surrounded by nearly 1 m of ductile-iron shielding. The cavity is designed to store 52 baskets that accommodate UO_2 ($\sim$ 88.2 % uranium and 11.8 oxygen) fuel assemblies that originate from Boiling Water Reactors (BWR). The simulated box-shaped baskets have a length of 4.48 m and are arranged across a grid of eight columns and eight rows. A pair of trunnions is also simulated at the top and the end bottom of the CASTOR. These trunnions are bolted and only be used for the attachment of handling equipment.

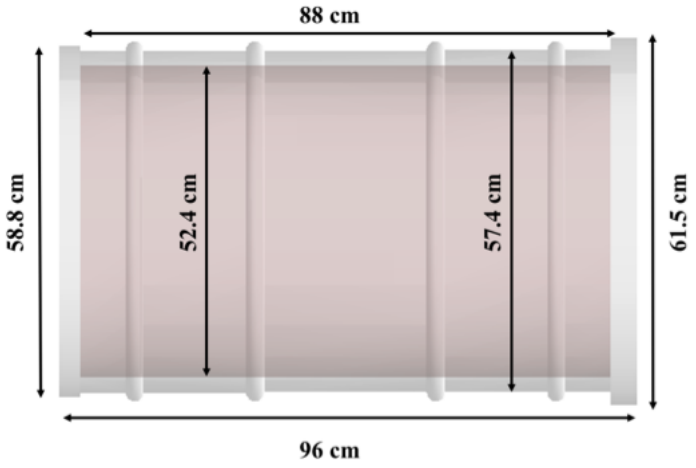

Figure 4.7: The simulated cement-matrix steel drum. The thickness of the cap and the base are 4.5 cm and 3.5 cm, respectively.

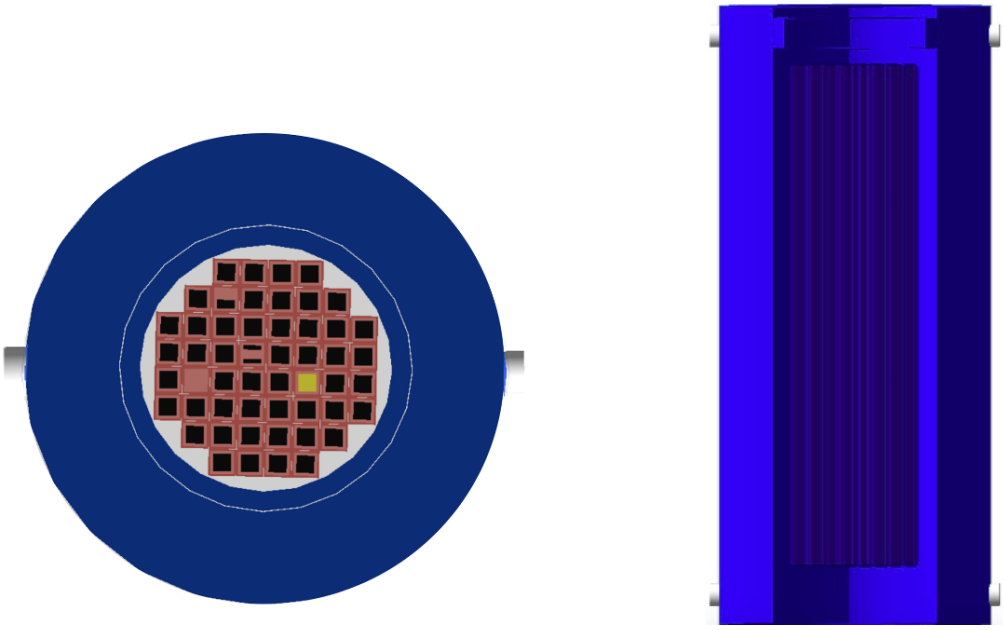

(a) (b)

Figure 4.8: (a) top and (b) side views of the simulated V/52 CASTOR cask accommodating the 52 waste baskets. Examples of various baskets accommodating various contents are showed, such as uranium oxide fully-loaded, uranium oxide half-loaded, empty and non-standard contents (in yellow). The lid and the base removed for visualisation purposes.

4.3 Muon momentum measurement

In MST imaging technology, the muon momentum plays a crucial role and is often used in muon reconstruction algorithms as a normalization factor for the scattering angle of muons. This normalization in simulation setup is performed to prevent the misinterpretation of the presence of high-Z materials when, in reality, low momentum muons significantly scatter in low-Z materials. Experimentally, it is not directly possible to measure muon momentum using the Time of Flight (TOF) method, as this demands alternative, high-precision, and expensive detectors with excellent time resolution. Alternatively, the muon momentum might be estimated in the future using a Cherenkov detector [70]. In recent years, several studies proposed methods of measuring muon momentum on simulated or experimental data. For example, for MST technique, a method that exploits the mechanism of Multiple Coulomb Scattering (MCS) to measure muons momentum that crosses through known materials, e.g. the detector structure materials. Subsequently, radiation length information is used

to calculate the scattering angles of muon between two or multiple consecutive detector layers (see Figure 4.9). Then the muon momentum can be calculated using the width of the scattering angles. However, the momentum is poorly estimated using this method, and it can be improved by adding several layers of dense materials to increase the scattering events, this is for example explained in [71]. As this thesis is based

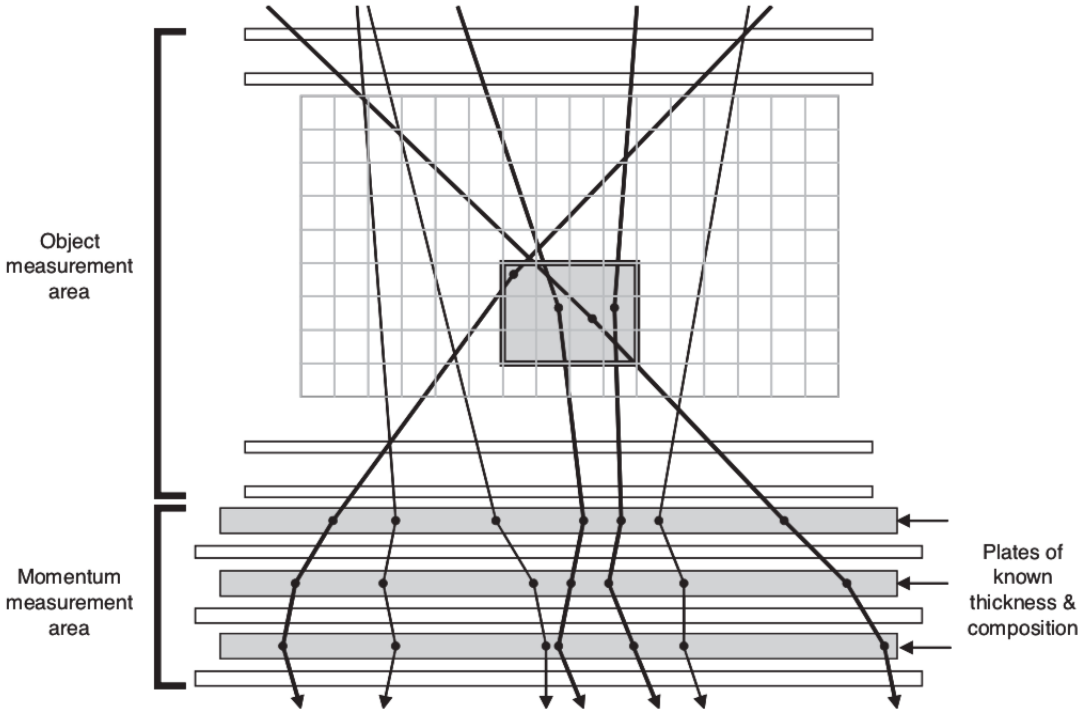

Figure 4.9: Schematic of the muon momentum measurement method showing the principle of estimating muon momentum using multiple Coulomb scattering across the detector materials (known materials) [71].

on simulation studies, and for investigating the effects of muon momentum in all the reconstruction algorithms (explained in detail in the next chapter), the default setup of the momentum information used in this thesis involves adding a 50% Gaussian smear to the MC truth momentum. Based on the findings in [43], this thesis opted for this method because it suggests that the muon momentum can be estimated with about 50% precision using residuals from a detector with three-layer track fit . Additional approaches include comparing the results using the MC truth momentum to the results obtained from the default setup of muon momentum information, as well as removing the momentum information.

4.4 Summary

This chapter described the simulations performed on MST systems using cosmic muons and nuclear waste packages. The structure of the MST detector was described and the track fitting process of each muon between the upper and the lower track systems is also explained. The detectors were simulated with physical structure, dimension, and spatial resolutions that match the RPCs and DCs which make up a real experimental tracking system. Moreover, the default setup of using muon momentum information for this thesis is briefly demonstrated. These simulations will be applied to investigate the ability of MST system and several reconstruction algorithms to image and classify well-shielded materials in chapters 5, and 6, respectively.

Chapter 5

Muon reconstruction algorithms

Performing Monto Carlo (MC) simulation studies to image nuclear waste using the Muon Scattering Tomography (MST) technique and associated algorithms can help to identify materials that disposed/stored within the shielding matrix. Reconstructing a 3D image of the volume of interest can be adversely affected by several factors, such as a thicker and/or higher-density shielding matrix. Detailed simulation studies are required to extract information about the roles of each variable, and how it enhances or degrades the performance of the MST technique.

Section 5.1 describes the techniques of three common reconstruction algorithms, as well as a statistical analysis method which is described in 5.2 to evaluate the performances of the MST and the algorithms used quantitatively using the contrast-to-noise ratio (CNR) method [72]. This helps to to evaluate the efficacy of the feature resolution outputs when imaging different materials with different atomic numbers inside different nuclear waste packages. It also helps to understand the limitations of the previous reconstruction algorithm methods in the characterization of nuclear waste materials. Section 5.4 demonstrates the performance results of the chosen algorithms in differentiating between two regions inside the volume of interest. Specifically, regions inside a small cemented-matrix drum in section 5.4.1, and regions inside the large-scale V52 CASTOR in section 5.4.2.

5.1 Muon reconstruction algorithms

The muon trajectories are reconstructed using dedicated algorithms. In this chapter, we consider three frequently-used algorithms; the simple Point of Closest Approach (PoCA) algorithm [73] (see section 5.1.1), the Angle Statistics Reconstruction (ASR) algorithm [74] (see section 5.1.2), and the Binned Clustering (BC) algorithm [69] (see section 5.1.3). In MST, it is common that the reconstruction algorithms divide the volume of interest into a 3D cubic-voxel grid with a side length of typically 10 mm for each voxel. However, multiple alternative approaches in the shape of the 3D voxels were investigated in addition to the default cubic-voxels, (see section 5.2). These approaches were considered depending on the size of the volume of interest (the distance between the upper and the lower muon tracker). Finally, a discriminator score for each voxel is then extracted from all the muon trajectories that have traversed through the volume of interest. Subsequently, all regions containing high-Z, medium-Z, and low-Z material inside the volume of interest can be identified.

This section will explain in detail the methods used by the three reconstruction algorithms considered in this work. In addition, an example of imaging a tungsten cube with a side length of 10 cm embedded inside a small nuclear waste drum will be used to compare the performance of each algorithm (see Figure 5.1). In order to visualise the tungsten cube inside the drum, the 3D map produced by each algorithm is sliced into a 2D projection in a plane through the centre of the cube. Examples of the 2D projected outputs of all algorithms will be shown when using cubic and rectangular voxel grids, with dimension of (10 cm $\times$ 10 cm $\times$ 10 cm, and 10 cm $\times$ 10 cm $\times$ 30 cm, respectively).

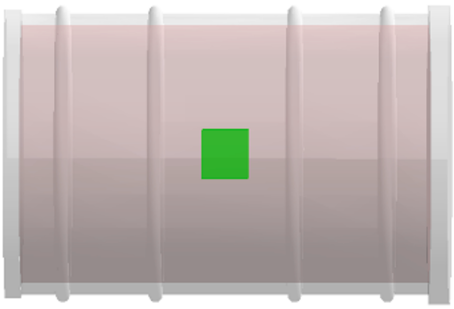

Figure 5.1: a 10 cm side length tungsten cube placed in the centre of a simulated cement matrix nuclear waste drum.

5.1.1 Point of closest approach

As an algorithmic reconstruction imaging method, the Point of Closest Approach (PoCA) algorithm is a straightforward method that offers less analytical complexity and hence faster imaging times, which makes it commonly used in MST techniques. PoCA assumes that when a muon travels through the voxellized volume (a 3D voxel grid), it undergoes multiple scatterings, which are then approximated to a single scattering at a single position (vertex). This single scattering position is located by extrapolating the entrance and exit points of muon tracks through the volume of interest, see Figure 5.2. The voxel containing the minimum distance between the tracks is defined as the single scattering occurrence voxel as follows:

- Define 3D grid voxels in the volume of interest, which are used to store the 3D image values.
- For each muon, the trajectories are determined using linear interpolation of the detector hits from both the incoming and outgoing muon paths.
- The calculated muon trajectories are extrapolated within the 3D cubic voxel grid.
- The distances between the two trajectories are calculated, and the point at which both trajectories become the closest is considered as the position where the single scatter occurs.
- The voxel containing this single vertex is weighted by the scattering angle of that muon.

In theory, the muon is likely to have a large scattering angle when it encounters high-Z material inside the investigated volume. Inside the 3D cubic voxel grid, a value is attributed to each voxel which is determined by weighting the average angle for all muon trajectories whose point of closest approach is located in that voxel, this value will be referred to henceforth as the PoCA discriminator. Using this PoCA discriminator, materials with a high Z can be distinguished from other materials with a lower Z (see Figure 5.3). However, the PoCA method is susceptible to introducing noise as a result of the assumption that a single large scatter has taken place (see, e.g., Figure 5.4(a)). This assumption has a number of weaknesses, e.g., some muon tracks might be incorrectly extrapolated and some PoCA points may occur outside the volume of interest. Such instances of muon track mis-reconstruction within the volume of interest can lead to inaccurate information which may be interpreted as an extreme scattering vertex inside a voxel.

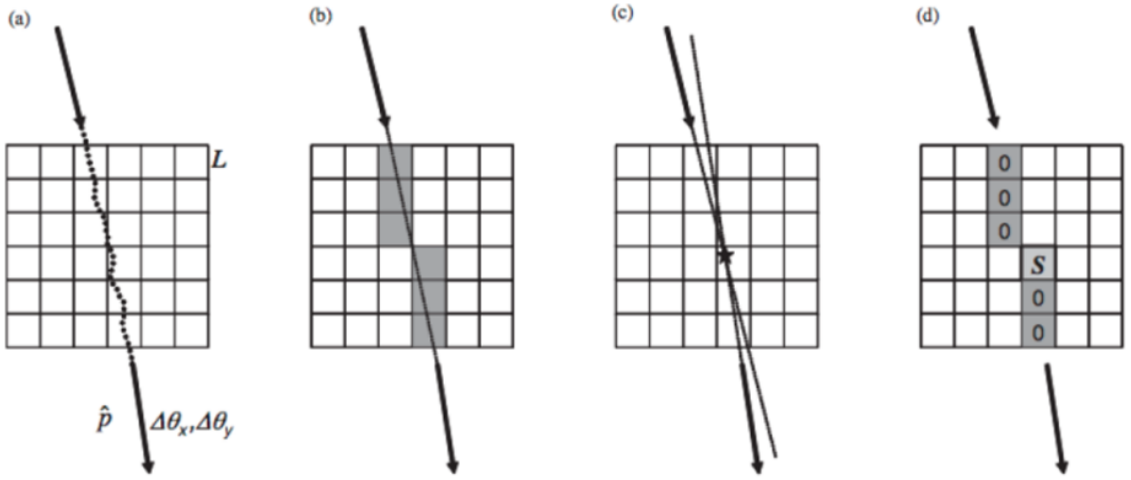

Figure 5.2: 2D representation of the PoCA method concept: (a) illustrates the stochastic path of a muon through the volume of interest. (b) depicts a straight line as an approximation of the muon's path crossing through selected voxels. (c) demonstrates the extrapolation of incoming and outgoing muon trajectories through the voxels, identifying the voxel that contains the point of closest approach (PoCA). (d) highlights the selected voxel containing the PoCA, assigning a signal to this voxel and zero to all other voxels [71].

Statistically, the smearing noise on the vertical direction inherited from the misreconstruction of the scattering vertex can be slightly reduced by using a rectangular voxel grid (see Section 5.2.2) with dimensions of (10 mm × 10 mm × 30 mm), see Figure 5.4 (b). However, we shall avoid the bias of the human eye when reading the output by testing the algorithm's output statistically. This will be explained in detail in section 5.2.

5.1.2 Angle statistical reconstruction algorithm

Unlike the PoCA method, the ASR algorithm assumes that when a muon travels through the 3D voxel grid, it is likely to experience many small scatters. The ASR thus avoids the underlying assumption of the PoCA algorithm that a muon only scatters inside a single voxel. The ASR algorithm was developed to mitigate the effects of using the PoCA method's inaccurate approximation of the muon trajectories. This has been achieved by applying a minimum chosen distance (D_r) between the reconstructed muon trajectories and the centre (c) of a voxel, therefore only voxels that lie within the chosen distance are considered. Any voxel that is located beyond the chosen distance

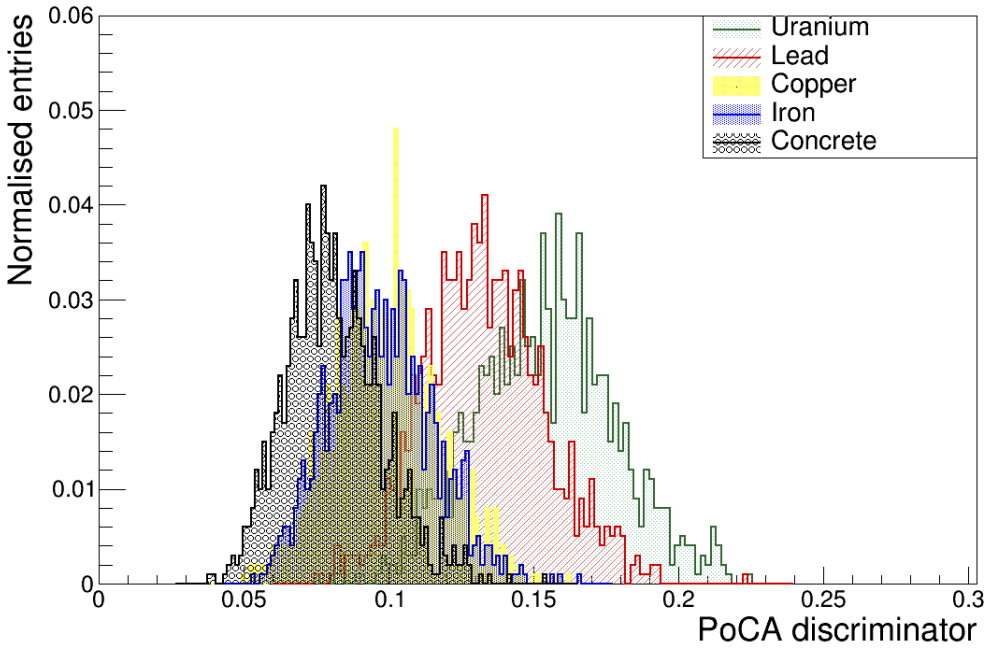

Figure 5.3: Comparison of distributions of the PoCA algorithm discriminator, for 10 cm cubes of uranium, lead, copper, iron, and concrete. Higher discriminator values correspond to higher Z materials. The 3D voxel grid containing these distributions is cubic with a side length of 10 mm.

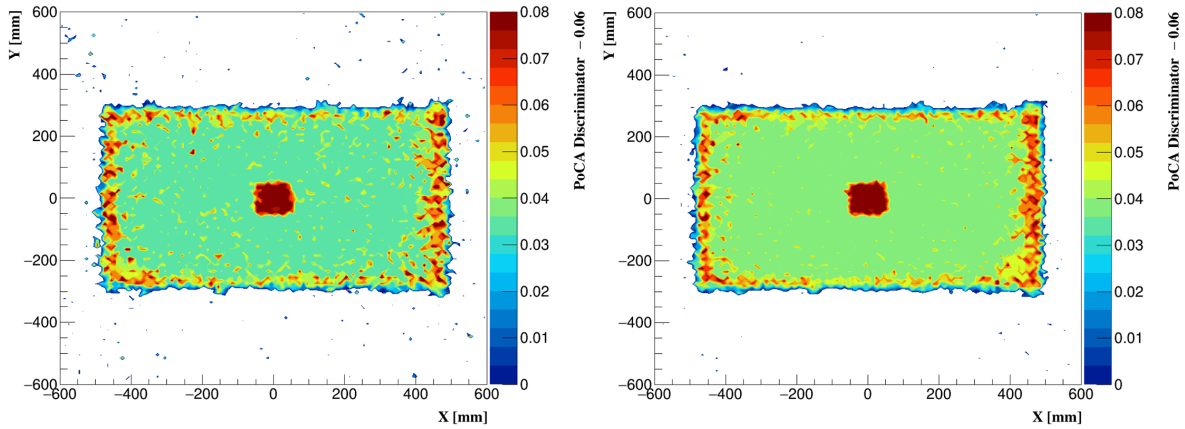

(a) (b)

Figure 5.4: The 2D projected PoCA output of the tungsten cube inside the small drum using (a) a cubic voxel grid and (b) a rectangular voxel grid. The exposure time was 12 days equivalent.

D_r will be neglected. The minimum distance is determined by:

$$D_r = \max(\min ||a(z) - c||, \min ||b(z) - c||) \tag{5.1}$$

where $a(z)$ and $b(z)$ represent the fitted trajectories of the incoming and the outgoing muons, respectively. A threshold distance (d_{th}) is chosen. Ideally (d_{th}) is the same

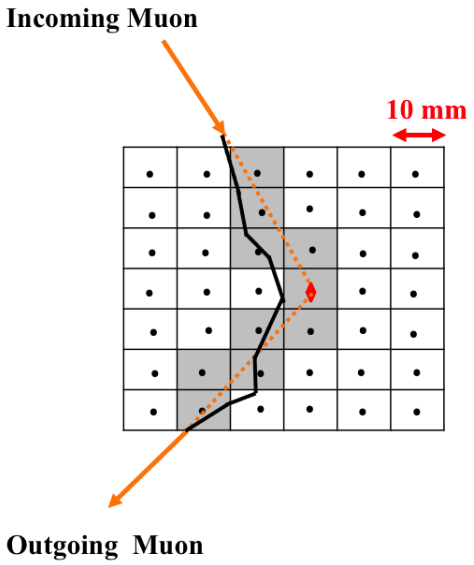

Figure 5.5: 2D illustration of the ASR method: ♦ denotes the reconstructed vertex, the closest approach point of the incoming (a(z)) and outgoing (b(z)) trajectories, represented by red-dashed lines. The • symbol marks the voxel centre, and all grey voxels with centres within distance d_{th} from either trajectory contribute to the weighting of the ASR discriminator scores.

size as a voxel so that all voxels that have $D_r < d_{th}$ will be assigned a discriminator score. For each voxel and each muon with momentum of (p), the projected scattering angles on the x-axis and y-axis (θ_x and θ_y respectively) are used to generate two scores S_1=($|\theta_x| \cdot \widetilde{p}$) and S_2=($|\theta_y| \cdot \widetilde{p}$), where $\widetilde{p}$ is the muon's momentum according to $\widetilde{p} = \frac{P}{P_{norm}}$, where $P_{norm} = 3$ GeV/c . This is repeated for all muons passing through the object of interest resulting in a distribution of the S_1 and S_2 scores for each voxel. Scores are only added to a voxel's distribution if the entering/exiting muon trajectories pass within d_{th} of the voxel.

This method ensures that not just a single voxel is weighted, but rather all voxels are taken into account depending on their proximity to the incoming and outgoing muon paths, as follows:

- Define 3D grid voxels in the volume of interest, which are used to store the 3D image values.
- For each voxel, v, generate an empty list $S_v = \{\}$.
- Determine a minimum distance (a threshold), typically is equal to to the voxel size.
- For each muon, define the incoming $a(z)$ and outgoing muon $b(z)$ lines to detected hit positions, and fit the two lines via least square.
- For each muon, calculate the projection of the deflection angles along x and y planes.
- Generate scores, $S_1 = (|\theta_x| \cdot \widetilde{p})$ and $S_2 = (|\theta_y| \cdot \widetilde{p})$, where $\widetilde{p}$ is the muon's momentum according to $\widetilde{p} = \frac{P}{P_{norm}}$, where $P_{norm} = 3$ GeV/c.
- Choose all voxels, such that the center of these voxels is within a certain proximity (d_{th} = the voxel size) to either the incoming or outgoing tracks.
- Append the S_1 and S_2 scores to the list S_v.
- Sort the $k_v th$ value of S_v in ascending order, where k_v is equal to $q \times n$, where q and n are the size of S_v, and a chosen quartile, respectively.
- For each voxel v, the final score will be the value of k_v.

For each voxel the final distribution of scores is taken and an ASR discriminator score is assigned to be that of the third quartile (0.75) of the distribution, this value will subsequently be referred to in this thesis as the ASR discriminator. These final discriminator scores are used to locate voxels in which high-Z materials might be present. Figure 5.6 shows the ASR discriminator distributions for several materials, higher discriminators correspond to high-Z material.

Figure 5.7(a) demonstrates how, by excluding outlier events with extreme scattering, the ASR algorithm has successfully reduced noise resulting in a clearer image of the tungsten block. Moreover, increasing the vertical height of each voxel boosts the clarity of the reconstructed image, (see Figure 5.7(b)).

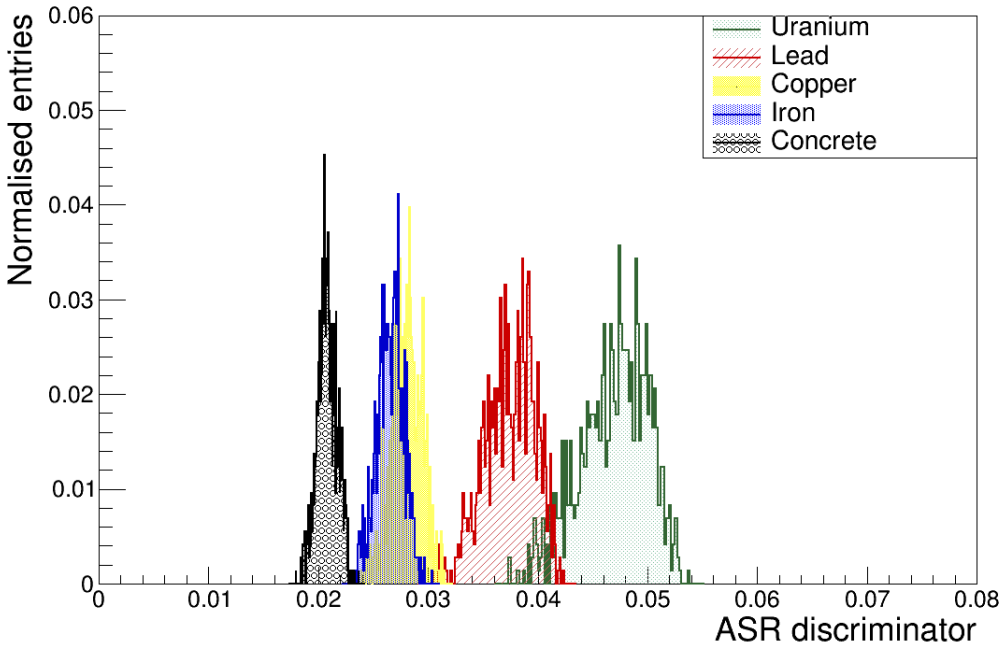

Figure 5.6: Comparison of distributions of the ASR algorithm discriminator, for 10 cm cubes of uranium, lead, copper, iron, and concrete. Higher discriminator values correspond to higher Z materials. The 3D voxel grid containing these distributions is cubic with a side length of 10 mm.

5.1.3 Binned Clustering Algorithm

The BC algorithm [69] is based on the fact that the density of high angle scattering vertices is higher in high-Z materials. After assigning the scattering vertices to a voxel, the scattering angles are ordered and only the N most highly scattered vertices are considered to calculate the metric distance between two vertices weighted by their scattering angle. Voxels containing a number of vertices less than N are neglected. The choice of N is important as it can effect the reconstructed image. For instance, a higher value of N might cause a distortion of the reconstructed image as a result of removing more voxels containing lower number of vertices than the chosen N.

For each pair of vertices v_i and v_j within the investigated volume, a weighted metric distance, $\widetilde{m_{ij}}$ is determined by:

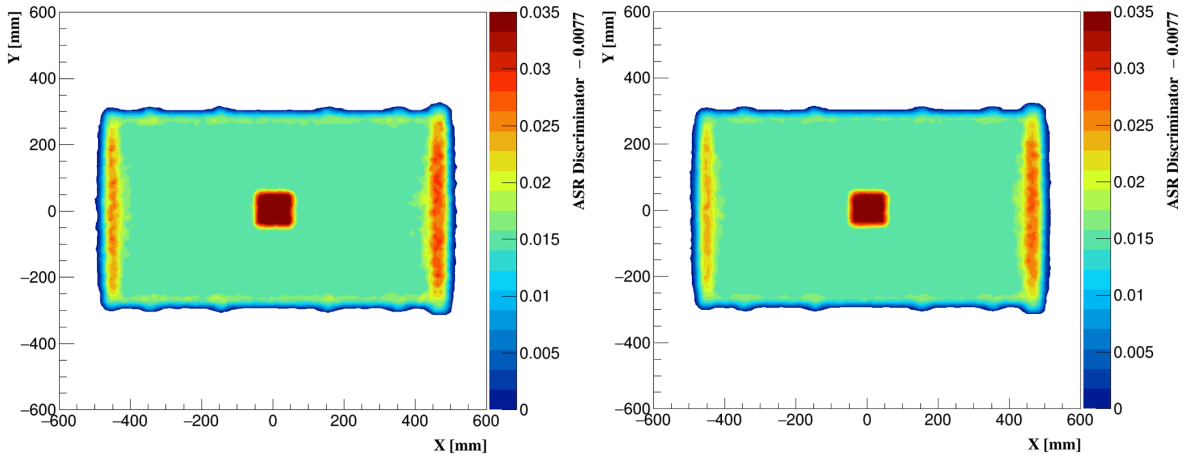

(a) (b)

Figure 5.7: The 2D projected ASR output of the tungsten cube inside the small drum using (a) a cubic voxel grid and (b) a rectangular voxel grid. The exposure time was 12 days equivalent.

$$\widetilde{m}_{ij} = \frac{||V_i - V_j||}{(\theta_i \widetilde{p}_i) \cdot (\theta_j \widetilde{p}_j)} \tag{5.2}$$

where, θ_i , θ_j are the scattering angles for muons i and j respectively of vertices v_i and v_j. While V_i represents the position of the scattering vertex v_i and V_j represents the position of the scattering vertex v_j. For muon i, p_i is the muon momentum of scattering vertex (v_i) and $\widetilde{p}_i$ is the muon momentum according to $\widetilde{p}_i = \frac{P_i}{P_{norm}}$ where $P_{norm} = 3$ GeV/c. This algorithm uses the density of the PoCA high-angle scattering vertices as follows:

- Define 3D grid voxels in the volume of interest, which are used to store the 3D image values.
- For each voxel, generate three empty lists S_θ={}, S_{pos}={} and S_{disc}={}.
- Calculate the scattering angle, θ, from the incoming and outgoing muon tracks information using the PoCA single scatter assumption.
- For each muon, append the scattering angle (θ) and the scattering vertex position to S_θ and S_{pos}, respectively. Here, S is the voxel that contains the single scattering vertex.
- For all S voxels, sort the scattering vertices in the lists (S_θ and S_{pos}) by descending normalised θ.

- Choose a value of N and discard all S voxels containing a number of vertices $< N$.

For each S voxel, and for every of the $\binom{N}{2} = \frac{N!}{2!(N-2)!}$ pairs of vertices, v_i and v_j:

- Calculate the weighted metric between V_i and V_j ($\widetilde{m_{ij}}$) using equation 5.2.
- Calculate the values of $log(\widetilde{m_{ij}})$, and fill the histogram with these values.
- Append the values of $log(\widetilde{m_{ij}})$ distribution to the list S_{disc}.
- Sort the values of $log(\widetilde{m_{ij}})$ distribution in the list S_{disc} in ascending order.
- Calculate the median of the values of $log(\widetilde{m_{ij}})$ distribution in the list S_{disc}, this will serve as the final discriminator value for the S voxel.

The median of the distribution of $\log(\widetilde{m}_{ij})$ inside a voxel is used as the discriminator value for that voxel and this value will be referred to in this thesis as the BC discriminator. This is expected to be lower if the target is a high-Z material as the average distance between high scattering vertices is smaller and the scattering angles higher in high-Z materials. Conversely, if the target is a low-Z material, the median would be higher (see Figure 5.8). The BC discriminator output for imaging the tungsten cube inside the waste drum demonstrates good contrast when compared to the background (see Figure 5.9(a)). However, using the rectangular voxel grids results in less variation in the concrete matrix region, (see Figure 5.9(b)).

5.2 Performance Tests

5.2.1 Contrast-to-Noise Ratio (CNR)

One of the principal aims of this study is to undertake a quantitative comparison of the algorithms discussed above, to facilitate this, a method to quantitatively compare the outputs of all of the algorithms to each other was developed. The contrast to noise ratio (CNR) method is thus applied to compare an algorithm's ability to differentiate between two distinct regions (e.g. a region containing high-Z material against the matrix material) in the reconstructed image of the investigated object.

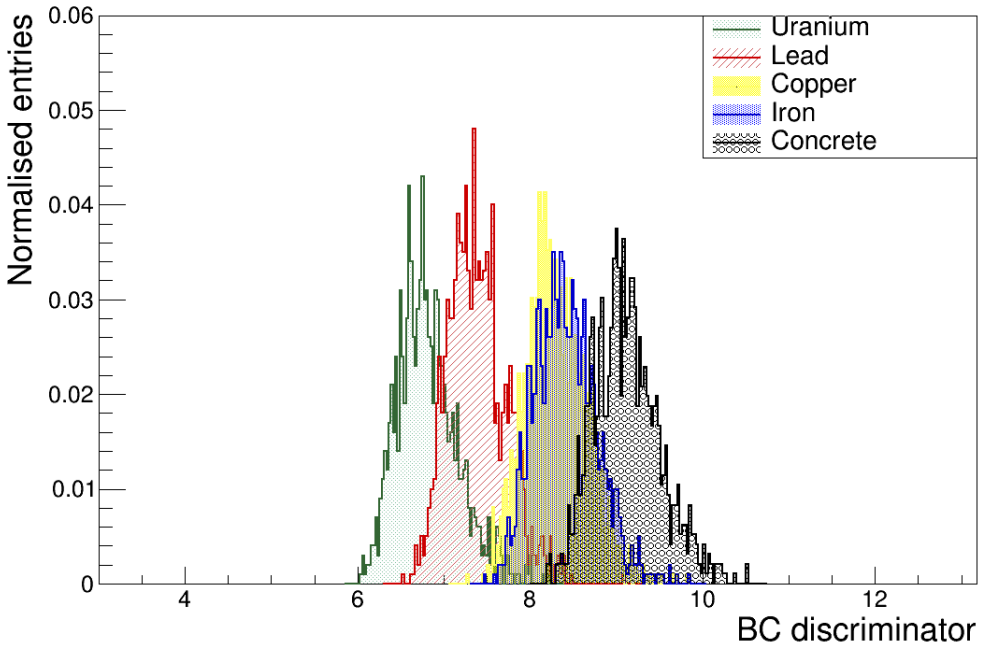

Figure 5.8: Comparison of distributions of the BC algorithm discriminator, for 10 cm cubes of uranium, lead, copper, iron, and concrete. Higher discriminator values correspond to lower Z materials. The 3D voxel grid containing these distributions is cubic with a side length of 10 mm.

To assess the reconstructed image quality, the so-called Contrast-to-Noise Ratio (CNR) method was employed to evaluate the efficacy of the considered algorithms in differentiating between low-contrast, medium-contrast, and high-contrast regions inside the investigated volume.

A high CNR value indicates that the algorithm is able to distinguish well between the two regions under comparison. Similarly, a low CNR value suggests that the algorithm under consideration is unable to make a distinction between the compared regions. The CNR value for two regions, A and B, is calculated to understand the feature resolution of the MST system and algorithm under consideration, and is given by:

$$\mathrm{CNR} = \frac{|\mu_A - \mu_B|}{\sqrt{\sigma_A^2 + \sigma_B^2}} \tag{5.3}$$

where μ_A is the mean of region A's signal and μ_B is the mean of region B's signal. Here σ_A and σ_B are the standard deviations of the signals in region A and region B,

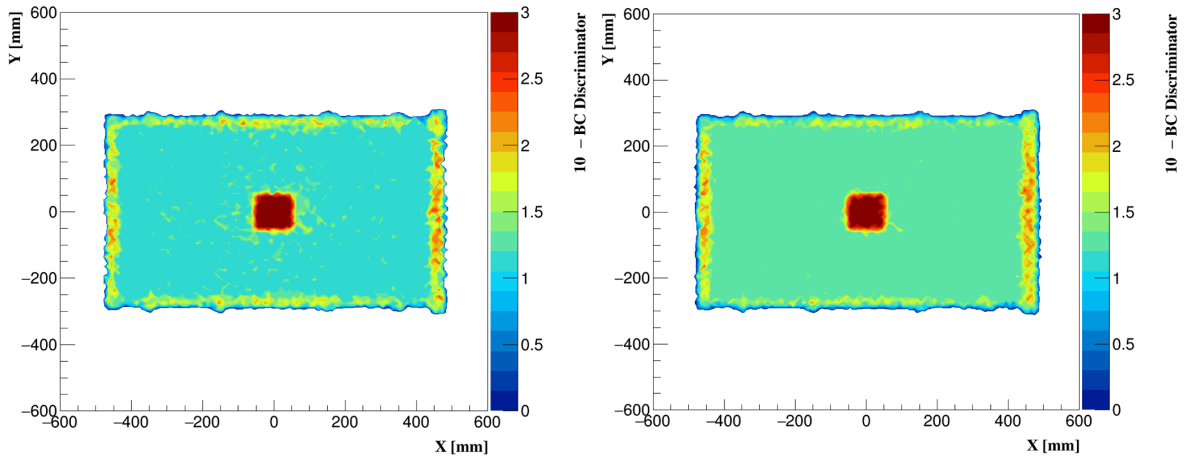

(a) (b)

Figure 5.9: The 2D projected BC output of the tungsten cube inside the small drum using (a) a cubic voxel grid and (b) a rectangular voxel grid. The BC algorithm considered the 18 most scattered tracks per voxel for 12 days of exposure time.

respectively.

5.2.2 Geometrical Voxel Shape

In MST, dividing the volume of interest into cubic voxels is a popular approach. Here, this thesis introduces a new approach by changing the voxels' shape to rectangular voxels. In addition to the default cubic voxels with a side length of 10 mm, alternative approaches were considered by increasing the voxel's height from 10 to 40 mm, in 10 mm intervals. This allows us to understand the effects of the vertical smearing inherited from the approximation of the scattering vertex position throughout the volume of interest. Three simulated MST muon track data cross three waste drums: an empty drum with only a concrete matrix, and two drums containing a 10 cm cube of uranium and lead in the centre of the drum, respectively. The exposure time for the three simulations was 8 days equivalent. For each simulation, four images of the target cube inside the drum have been reconstructed using four different 3D voxel-grids. The X- and Y-dimension of each voxel is set to be 10 mm, and the height of the voxel used to reconstruct the four images are respectively 10, 20, 30, and 40 mm.

Figure 5.10 shows the discriminator distributions of the uranium cube as a signal and the lead cube as a background for all algorithms considered in this study. Other comparisons were performed between the uranium cube as a signal and an equally-

sized concrete cube as a background. The quality of the four images was tested by comparing the uranium and lead distributions using the CNR method. The CNR value between the uranium and lead distributions increased for all algorithms when using the rectangular voxel grid with a height of 30 mm, see Figure 5.11. For example, the ASR algorithm produces a CNR value between uranium and lead approximately 45% higher than the CNR result when using the 10 mm voxel height, with values of 3.2 ± 0.1, and 2.2 ± 0.07, respectively. The comparison between uranium and concrete also shows the same trend for all methods with the best CNR value being obtained when using a 30 mm voxel height. Henceforth, for the small steel drum analysis a voxel size of 10 mm $\times$ 10 mm $\times$ 30 mm will be used.

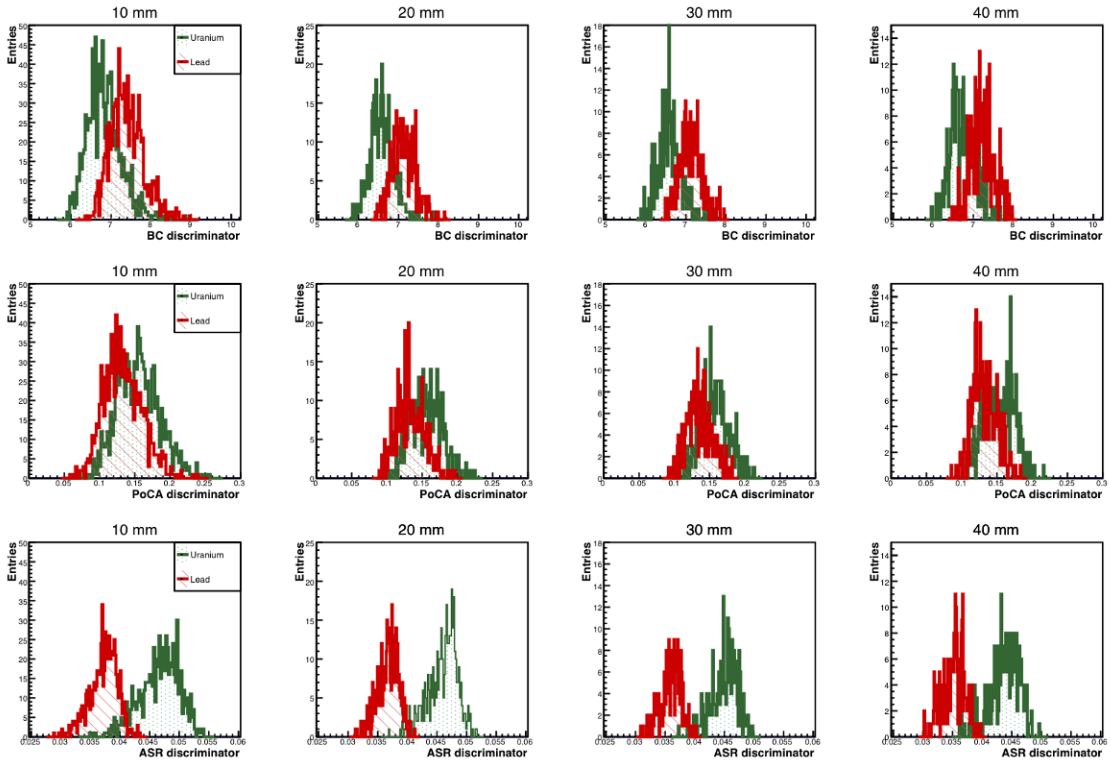

Figure 5.10: From the left: the discriminator distributions inside voxels with height of 10, 20, 30 and 40 mm, respectively. The signal in green are voxels containing 10 cm side-length uranium and background in red are voxels containing lead cube. The top, middle and the bottom discriminator distributions are calculated using the PoCA, the BC, and the ASR algorithms, respectively. The exposure time was 8 days equivalent.

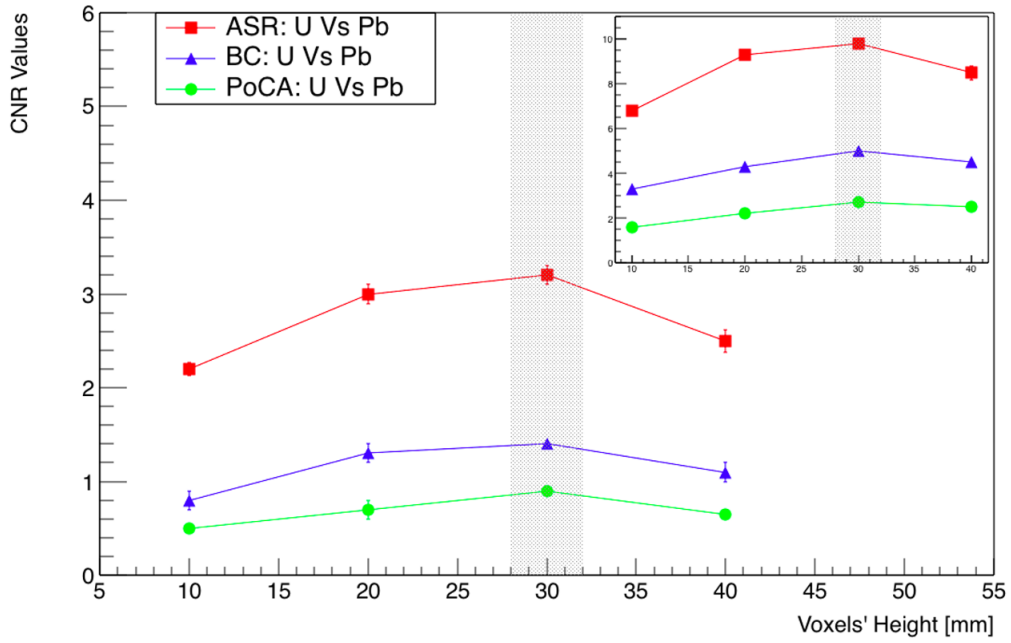

Figure 5.11: Comparison of the CNR value as a function of the voxel height of all algorithms when differentiating between a 10 cm side-length uranium cube against an equally-sized lead cube. The inset shows the CNR values when comparing uranium against concrete. The highest CNR value has been highlighted with a grey box.

5.2.3 Minimum CNR (mCNR) value

When comparing results from the imaging of different materials in both the small steel drum and CASTOR V/52 cask a consistent metric to compare results is required. The concept of a specific metric, namely a "minimum CNR" (mCNR) is thus introduced to distinguish between two regions. Good quality of the reconstructed images is highly desirable in this study. Hence, in this chapter, the study has applied two conditions to determine the mCNR values for all methods and to differentiate between region A and region B.:

- The structures of regions A and B must be fully reconstructed (method's discriminator > 0).
- The mean discriminator of region A must be separated from that for region B by at least $\sigma_A + \sigma_B$ (see Equation 5.4) where σ_A and σ_B are the errors (the standard deviations) on the discriminators for regions A and B respectively, i.e.:

$$\mu_A - \mu_B > \sigma_A + \sigma_B \tag{5.4}$$

The mCNR value is defined by the minimum CNR value produced by each algorithm in which two comparable regions can be distinguished from each other regardless of the muon exposure time. Mathematically this is equivalent to saying that the 2 discrimination methods under consideration are separated by more than the sum of their (statistical) errors for that particular configuration. To avoid the position effects on the discriminator values, the target materials were placed individually in the centre of the drum, and then two simulations were performed of muon tracks that cross two waste drums containing a 10 cm side-length cube of uranium and lead, respectively. Four muon exposure times were considered for each simulation: 24, 15, 12, and 9 hours, see Figure 5.12. Based on the conditions set out in the study for determining the mCNR value, it has been statistically shown that this value is independent of the method used. Therefore, the ASR algorithm was selected for determining the mCNR value, as it yielded the clearest 2D image of the tungsten cube in Figure (5.7b). The mCNR value is calculated by comparing the uranium discriminator as a signal distribution against the lead discriminator as a background distribution. The results showed that after 24 and 15 hours of muon exposure time, the distributions of signal against background can achieve the mCNR value conditions with a value of 2 and 1.4, respectively. After 12 hours, the signal and background distributions are separated by less than their statistical errors, with CNR values of 1.1. Henceforth, the mCNR value to differentiate between any comparable regions is assigned to be 1.4 for all algorithms.

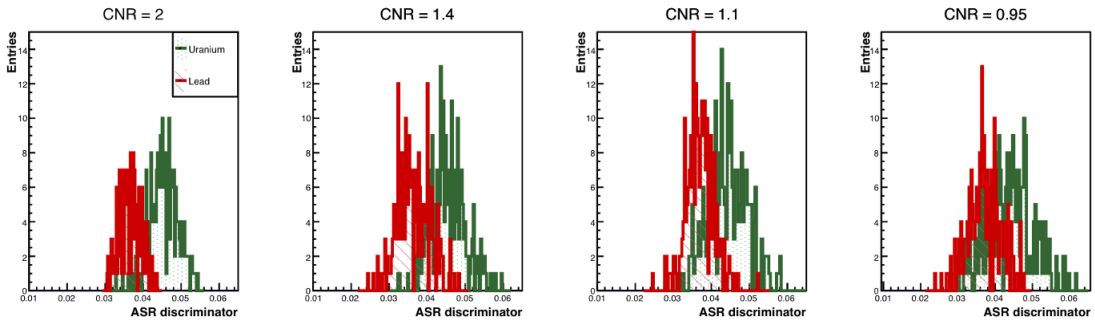

Figure 5.12: From the left: the ASR discriminator distributions of uranium and lead after 24, 15, 12, and 9 hours of muon exposure time. The histogram titles indicates the corresponding CNR value.

5.3 Small drum studies

In order to perform an initial assessment of performance of the various MST algorithms we considered an array of five cuboid materials of differing atomic number and density (see Table 5.1) which are embedded inside a small cemented matrix waste drum. The material cubes each have side length of 10 cm and they are aligned with the central (cylindrical) axis of the drum (see Figure 5.13).

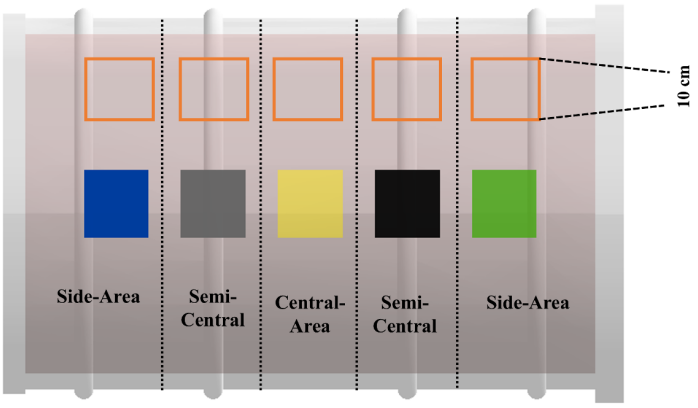

Figure 5.13: The five cubes of material each with a side of length 10 cm, placed within a concrete matrix inside a steel drum. From the left: Aluminium, Iron, Copper, Lead and Uranium. The orange squares represent the chosen background regions from both the side and central areas of the drum.

Target Material	**Atomic Number (Z)**	**Density g/cm^3**
Uranium	92	18.95
Lead	82	11.35
Copper	29	8.96
Iron	26	7.87
Aluminium	11	2.699

Table 5.1: Characteristics of the target materials under consideration.

For each algorithm described in section 5.1, the 3D density map of the drum contents is sliced into a 2D projection (through the centre of the drum in the $x-y$ plane) and then the regions inside the drum are located based on the discriminator

score for each method. Comparing each of the five regions to the background region should reveal the ability of each algorithm to locate high-density, medium-density and low-density materials inside the drum. For example, the CNR values which compares the copper region and the background region determines the ability of each algorithm to distinguish the copper cube within the background regions. Similarly, comparing two regions that contain materials with almost similar atomic numbers and densities (copper and iron) aid understanding of the efficacy of each algorithm.

The size and location of material within the drum may also affect the algorithm's performance. Hence, three simulations of the same materials were done with different sizes and locations of the target materials, namely cubes with side dimensions of 7 cm, 10 cm and 13 cm. The positions of the materials are classified as central, semi-central and side locations, as illustrated in Figure 5.13.

5.4 Results and Discussion

5.4.1 Application of the CNR test to a small nuclear waste drum

The three reconstruction algorithms discussed earlier were each used to image five target materials that varied in density from 2.699 g/cm^3 (aluminium) to 18.59 g/cm^3 (uranium). Furthermore, the dependence of the results on the size of the target materials and the muon exposure time was also considered.

5.4.1.1 Size and location dependence

In order to avoid the limitations of some reconstruction algorithms in cases of short exposure times, this section will compare the performance of all methods with a fixed muon exposure time. The performance of each method is represented here by the CNR value between two different regions after 12 days of muon exposure time. The sliced outputs shown in Figure 5.14 are taken through the 3D density maps along the centre of the drum. In this case the target materials are of size 10 cm $\times$ 10 cm $\times$ 10 cm inside the waste drum. The outputs clearly show that all three reconstruction methods are able to locate high-Z materials (U and Pb) shielded by the concrete matrix. Whereas the PoCA method can only reconstruct a partial image of the medium-Z target materials (Cu and Fe). For the low-Z target material, all methods are unable to separate the

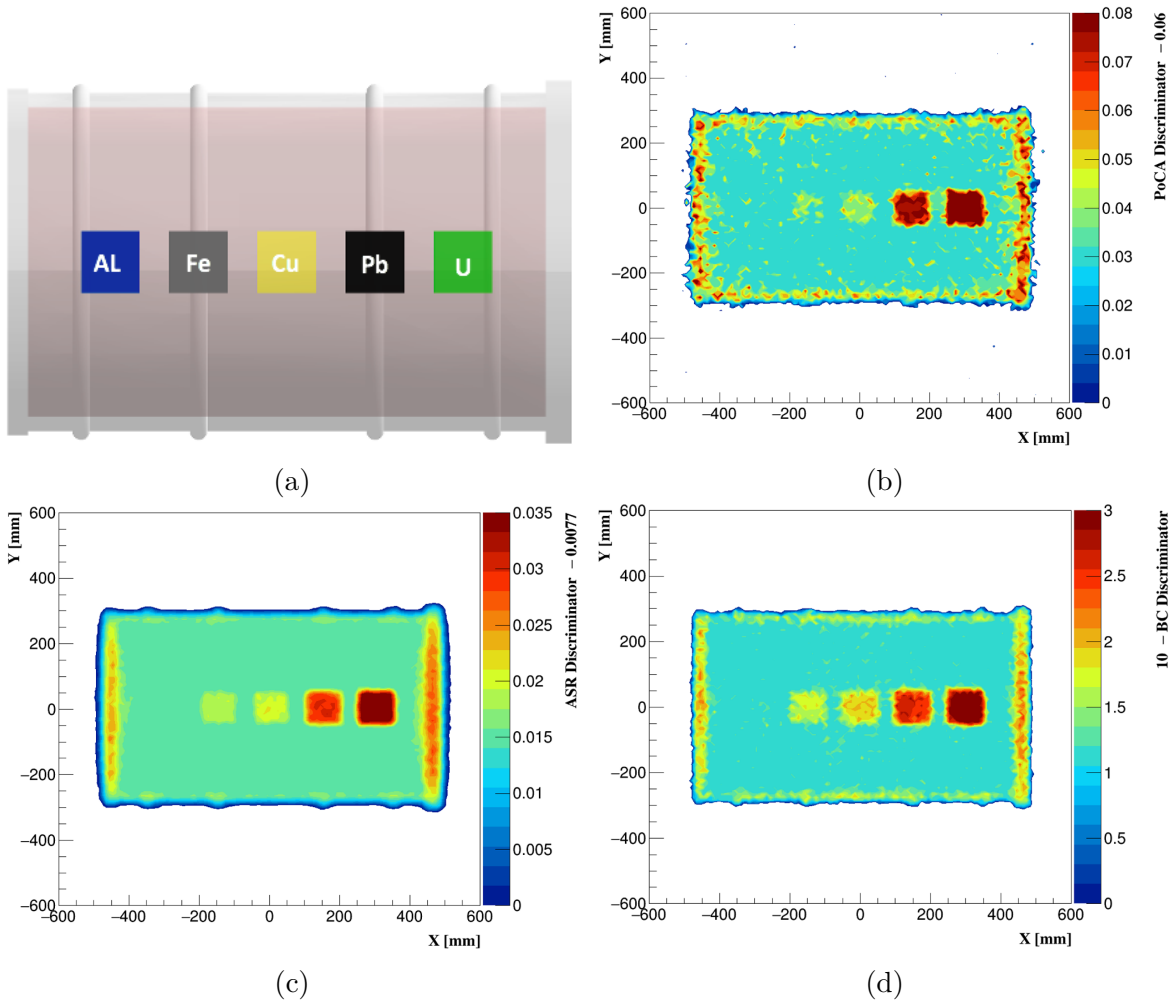

Figure 5.14: (a) Target materials inside the simulated drum. X-Y slice outputs through the 3D density map from applying the (b) PoCA, (c) ASR, and (d) BC algorithms respectively. The exposure time was 12 days equivalent. The BC algorithm considered the 18 most scattered tracks per voxel (N).

aluminium cube from the background, which is expected because the aluminium has similar density to the concrete.

Figure 5.15 shows the CNR results of all algorithms used after 12 days of muon exposure when comparing the five target materials, namely uranium, lead, copper, iron, and aluminium individually against the regions that have background signals. The ASR algorithm showed the best performance when comparing the regions that contained a high-Z material (uranium) cube against the background regions. In the case of a 10 cm cube the BC method produces a 42% lower CNR value of 6.0 $\pm$ 0.1 compared to the CNR value of 10.4 $\pm$ 0.2 produced by the ASR algorithm.

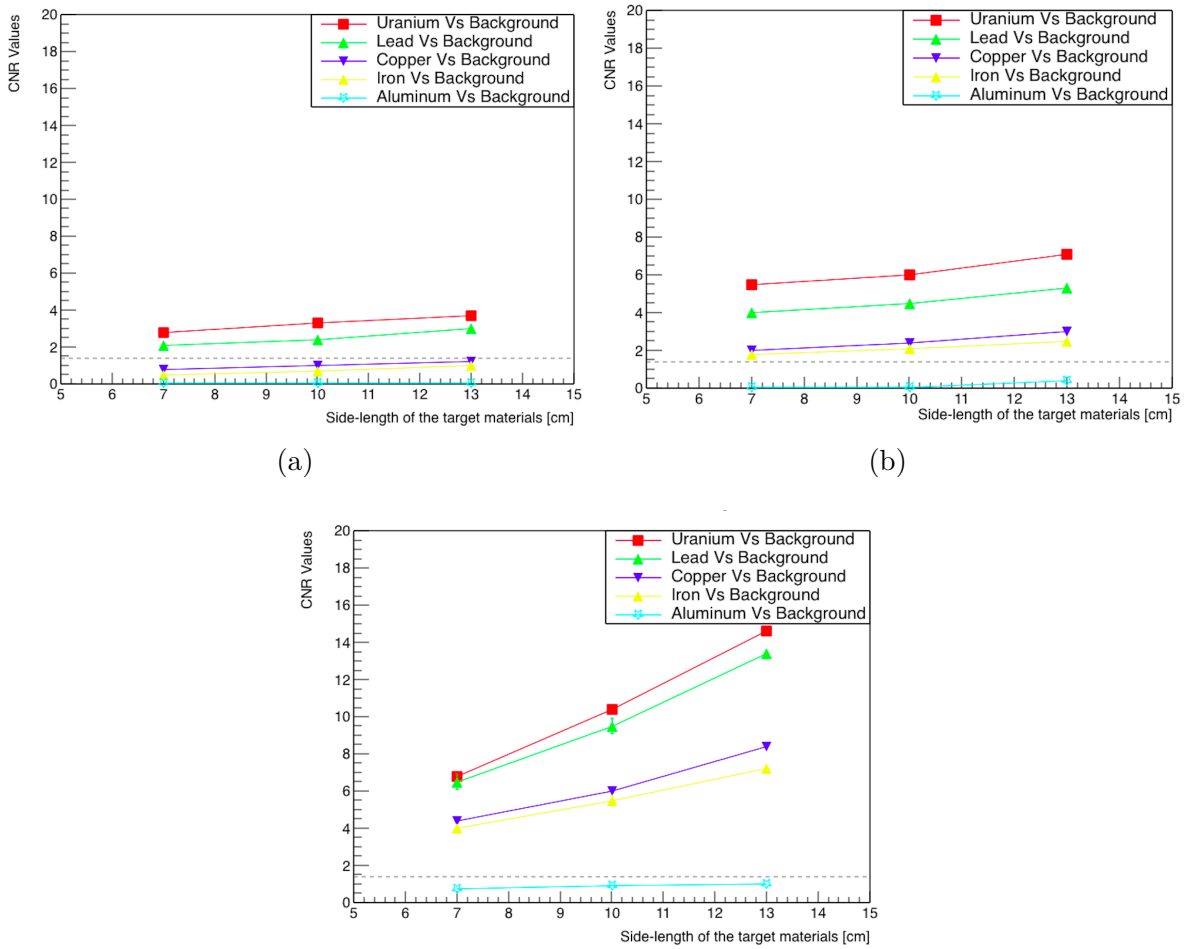

Figure 5.15: Comparison of the CNR values of the (a) PoCA, (b) BC and (c) ASR algorithms when differentiating between different target materials and background for target materials with side lengths of 7, 10, and 13 cm. Results are for 12 days of muon exposure time. The horizontal dashed line represents the minimum CNR value used to distinguish the target material inside the drum.

The PoCA method is affected by the single-scattering assumption, which leads to adding more noise which reduces the CNR values between the compared regions inside the drum. For example, for 10 cm sided cubes the PoCA algorithm has only been able to distinguish the uranium and lead from the background with relatively low CNR values of 3.3 ± 0.1 and 2.4 ± 0.12, respectively.

The results from comparing the regions containing copper and uranium reveal that the ASR algorithm is the most capable of differentiating between medium-Z and

high-Z materials with a CNR value of 7.1 ± 0.3, which is 108% better than the CNR value produced for the comparable regions by the BC method. In terms of the size dependence, the CNR results from comparing the target regions showed that the ASR is more likely to be affected by the target region's size. For example, comparing lead cubes against background regions showed an increase in the CNR values from 6.5 ± 0.4 to 13.4 ± 0.2 when the side-length of the lead cube is increased from 7 cm to 13 cm. While the CNR values in the BC method showed a steady decline as the side-length of the lead cube decreased from 13 cm to 7 cm dropping from 5.3 ± 0.12 to 4.0 ± 0.1. This indicates the efficacy of the BC method as it relies on calculating the vertices density within a comparable region.

5.4.1.2 Dependence on muon exposure time

An additional variable of muon exposure time, i.e. the number of muons contributing to each simulation, must be considered to to fully interpret the CNR values mentioned above. Figure 5.16 shows the output density maps produced by the ASR and BC algorithms after 2, 4, and 8 days of exposure time for the same target materials inside the small waste drum.

The ASR algorithm produces images of the target materials with greater clarity even when the exposure time is as short as 1 day. This clarity in the reconstructed image is ascribed to the fact that outsider events with large scattering angles are not included in the weights of the voxel. The ASR method maintained its capability of distinguishing between the uranium cube and the background region with CNR values of 9.8 ± 0.2 and 6.6 ± 0.2 after 8 and 2 days of muon exposure time, respectively.

The performance of the BC algorithm is significantly reduced when the imaging time is reduced to 2 days of muon exposure (see Figure 5.16(e)). For instance, the medium-Z materials (Cu and Fe) have become indistinguishable from the background regions, with CNR values of just 1.1 ± 0.04 and 0.86 ± 0.05 for the copper and iron targets, respectively. However, high-Z materials can still be differentiated from the background with CNR values of 2.8 ± 0.15 and 2.1 ± 0.12 respectively when comparing uranium and lead respectively against the background regions.

Generating tomographic images of the target materials can be achieved with fewer cosmic muons by using the ASR algorithm, e.g. after 12 hours of muon exposure time, this gives approximately 800,000 muons . By using the ASR method, the MST system can separate uranium and lead from background regions in only 12 hours of muon exposure time with CNR values of 4.0 ± 0.2 and 3.0 ± 0.15 respectively.

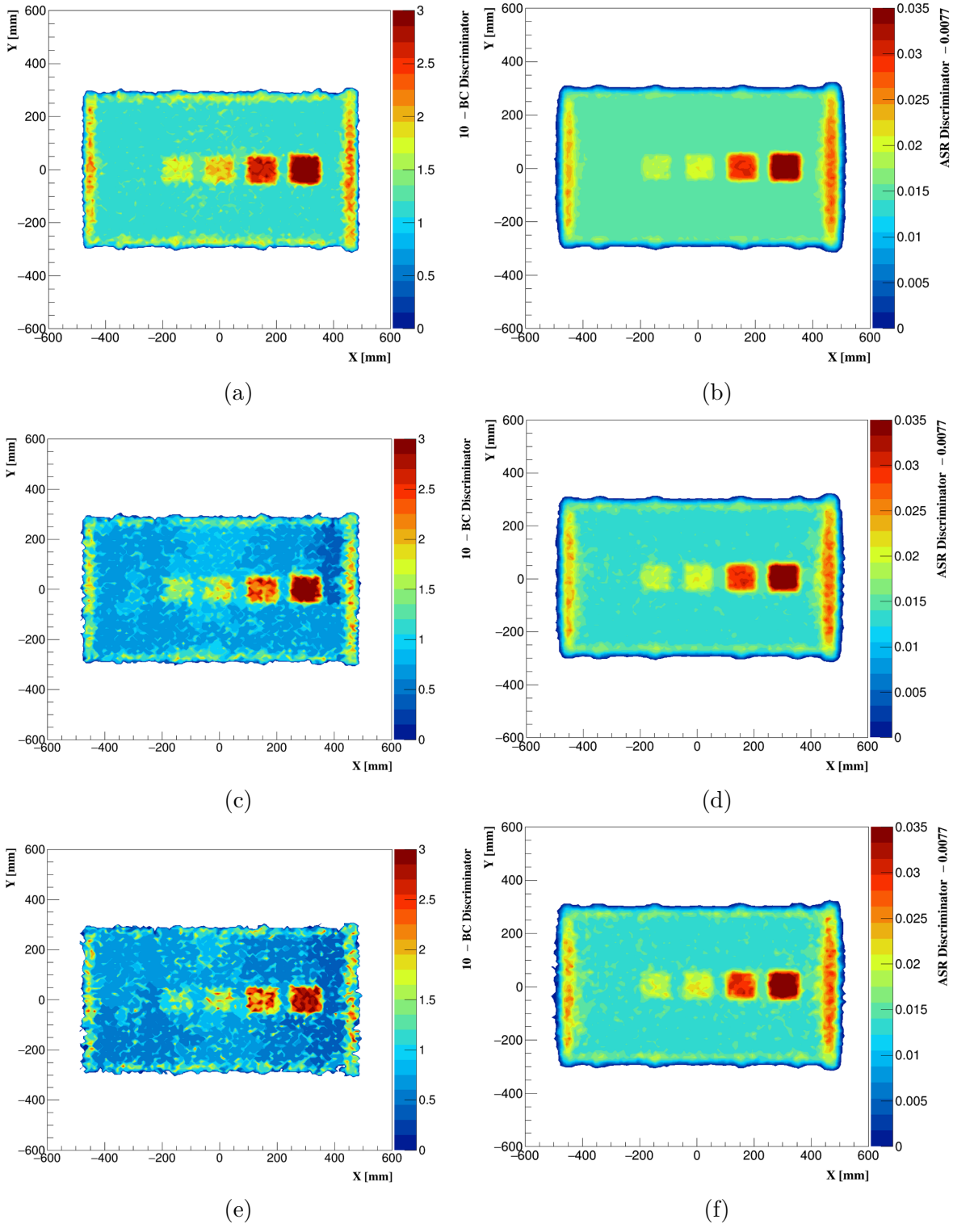

Figure 5.16: Comparison of feature resolution of the target materials with a side length of 10 cm reconstructed by the BC algorithm (left) and by the ASR algorithm (right) after 8 (top), 4 (middle), and 2 (bottom) days of muon exposure. The BC algorithm considered the 12, 6 and 4 most scattered tracks per voxel for 8, 4 and 2 days of exposure time, respectively.

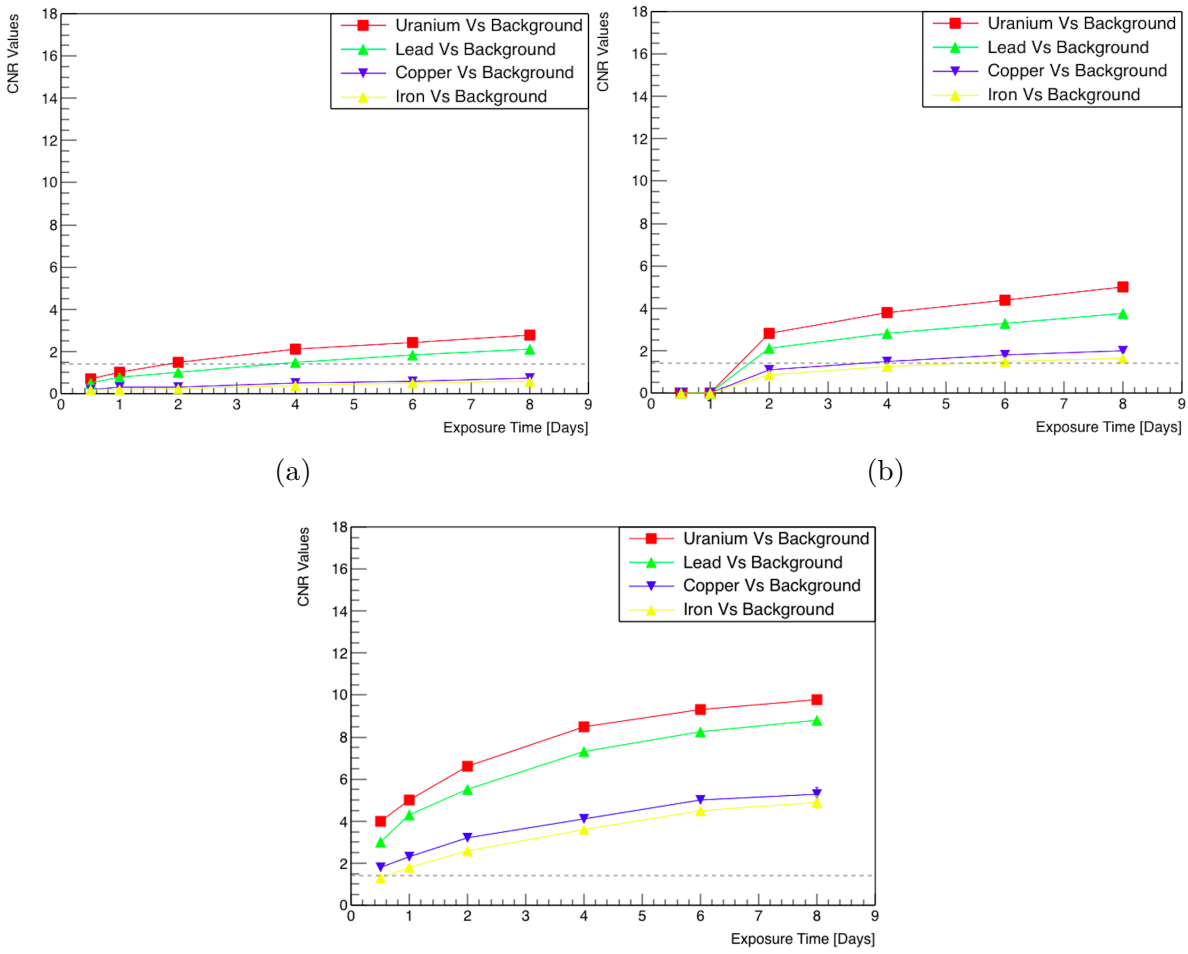

Figure 5.17: Comparison of the CNR values produced by the (a) PoCA, (b) BC and (c) ASR algorithms for different materials of 10 cm side-length as a function of the muon exposure time. The horizontal dashed line represents the minimum CNR value used to distinguish the target material inside the drum.

With a muon exposure time of 24 hours or less the BC algorithm is affected by the muon track cut parameter (N) in which most voxels containing the background region do not have enough scattering vertices, and they were discarded automatically by the algorithm. For this reason, the CNR values are set to 0.0 as one of the comparable regions was not reconstructed. A summary of the CNR values for 10 cm side-length cubes of uranium, lead, copper and iron as a function of muon exposure time is illustrated in Figure 5.17.

5.4.1.3 Influence of the spatial resolution

In addition to muon momentum information, the discriminator values in each voxel of all algorithms described in section 5.1 are calculated by mainly using the information of the muons' scattering angles. The BC and PoCA algorithms use (θ) and the ASR algorithm uses (θ_x and θ_y). Firstly, the CNR values between the target regions listed in tables 5.1 were measured according to the primary scattering angle information obtained from the simulated default system setting described in section 4.2.1. The angular resolution depends on the hit resolution of the detectors. To understand the influence on the angular resolution of the hit position resolution, a study was performed which considered degrading the drift chamber and the RPC hit position resolutions by 20, 50, 80, and 100% which, in turn, impacts the angular resolution of the system. Clearly the angular resolution of this system is dominated by the RPCs however, since the simulation represented an actual empirical system then for the sake of completeness both detector system resolutions were doubled.

Figure 5.18 shows examples of the BC outputs of a 10 cm side-length tungsten cube after degrading the spatial resolutions by 50% and 100%. The cube structure is easily distinguishable in both figures. However, there is a more variation in the discriminator values of the background matrix in the 100 % degraded resolution image of the drum. Furthermore, the reconstructed image of the cube appears to be sharper when using the default detector resolutions (see Figure 5.9(b)).

The results of additional simulations of the MST detector with degraded spatial resolutions have been performed with both fixed muon exposure time (4 days) and material size (10 cm side-length). Figure 5.19 shows the CNR results comparing the 4 target materials against the background regions, using the PoCA(a), BC(b), and ASR(c) algorithms.

The quality of the reconstructed images has been slightly affected by degrading the detector resolutions, especially when comparing the medium-Z materials against the background. For example, the ability of the detector system to differentiate between lead with 10 cm side-length and equally-sized background regions is slightly degraded from a CNR value of 7.3 ± 0.1 to 5.75 ± 0.22, when using the ASR algorithm. However, even with poor detector resolutions, all of the target materials reconstructed by the ASR can be easily distinguished, e.g., the copper and the iron cubes can be separated from the background regions with CNR values of 2.8 ± 0.2 and 2.3 ± 0.2, respectively.

Regardless of the muon exposure time, the detector's capability to reconstruct images of the target materials using the PoCA and BC methods remains above the

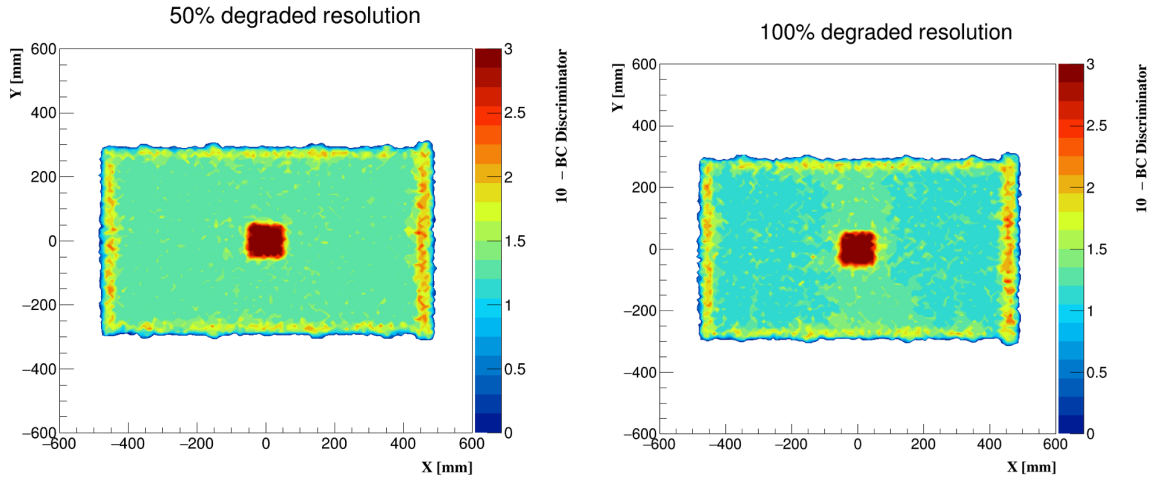

Figure 5.18: A 10 cm side length tungsten cube placed in the centre of a simulated cement matrix nuclear waste drum. The 2D projected BC outputs of the same cube inside the small drum using (left) the detector system after degrading the RPC and DC position resolutions to 0.525 and 3 mm and (right) to 0.7 and 4 mm respectively. The voxels containing the background regions have more variation of the reconstructed image in the later system. The exposure time was 12 days equivalent.

mCNR value when comparing high-Z materials against the background regions.

The system's capability to distinguish materials is not significantly impaired even when using RPCs with a degraded position resolution of 700 microns. Hence, the simulated detector configuration is able to generate tomographic images of shielded high-Z and medium-Z materials with fewer muons when using the ASR method (4 days of muon exposure time). With a shorter exposure time (12 hours), the detector system starts to lose its ability to separate copper from the background with a CNR value of 1.1 $\pm$ 0.05, when using the ASR method. However, the system is still able to discriminate high-Z materials, such as uranium, from the background with a CNR value of 3.3 $\pm$ 0.1 (see Figure 5.20).

5.4.2 CASTOR drum studies

In a second study, a CASTOR V/52 nuclear waste container was simulated (see Section 4.2.3) in order to assess so-called "diversion" scenarios whereby small amounts of fissile material is illegally diverted. Again, the performance of the different muon tomography reconstruction algorithms was considered and compared using the CNR metric. The CASTOR V/52 nuclear waste drum accommodates fuel assembly baskets. A number

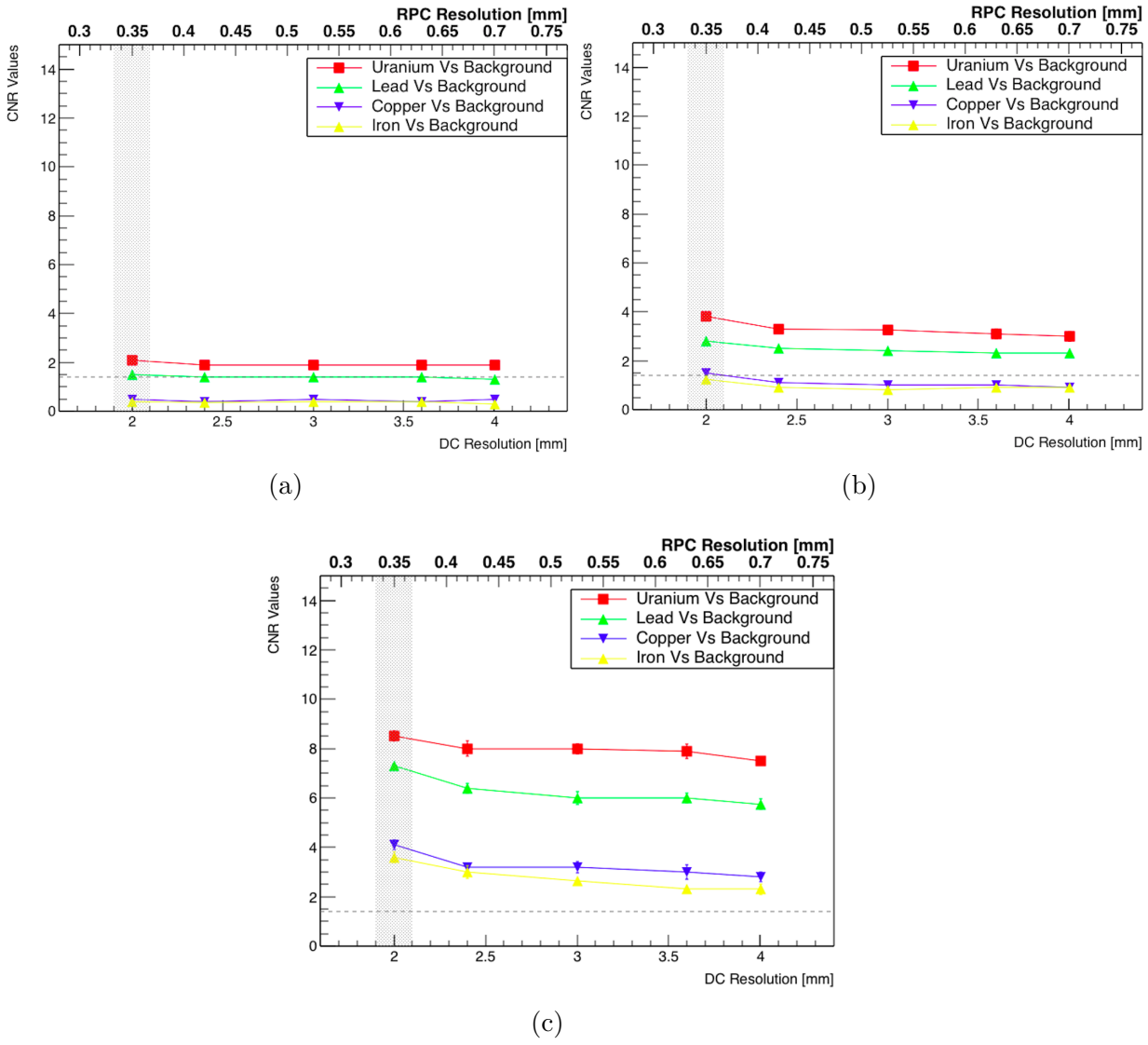

Figure 5.19: Comparison of the CNR values produced by the (a) PoCA, (b) BC and (c) ASR algorithms for different materials of 10 cm side-length as a function of the muon detector resolutions. The results obtained using the default detector setup are highlighted with a grey box. The horizontal dashed line represents the minimum CNR value used to distinguish the target material inside the drum. The exposure time was 4 days equivalent.

of scenarios were simultaneously considered in the simulation, (see Table 5.2), namely diversion of the nuclear fuel (modelled as uranium oxide) and replacement with lead or copper. A further fuel basket was intentionally left empty. The CNR test was subsequently extended to understand whether the performance of each algorithm would

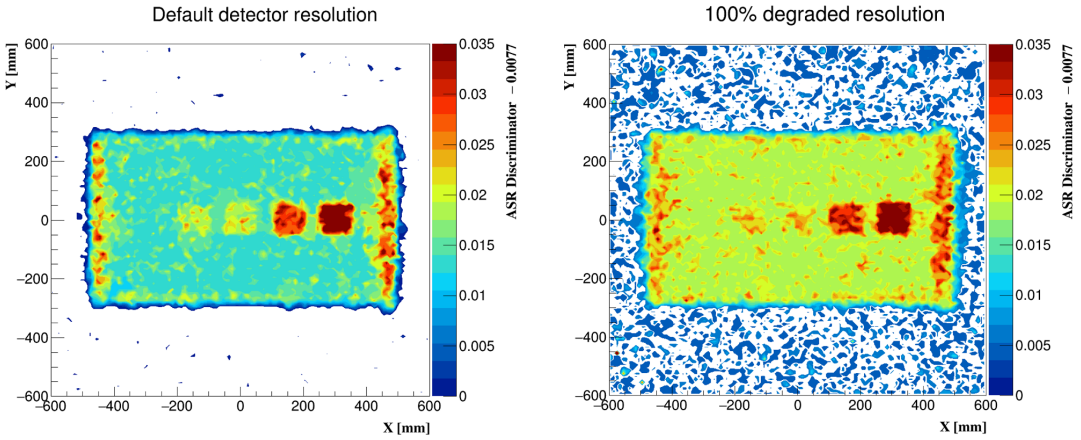

Figure 5.20: The 2D projected output of the target materials with a side length of 10 cm reconstructed by the ASR algorithm using the default detector resolution (left) and after degrading the RPC and DC position resolutions to 0.7 and 4 mm respectively (right). The exposure time was 12 hours equivalent.

be affected by a thicker and more shielded cask. As it was seen in the small drum study that using rectangular voxels shape has optimised all algorithms performances, hence, a rectangular shaped voxel also used here with dimension of 20 mm × 20 mm × 500 mm, (see Figure 5.22).

Basket Content	**Number of Baskets**	**Density g/cm^3**
Uranium Oxide (Fully-loaded)	48	10.97
Uranium Oxide(Half-loaded)	2	10.97
Lead	1	11.35
Copper	1	7.87
Empty	1	0.0012

Table 5.2: Details of the target materials placed inside the simulated CASTOR V/52 waste drum.

The CNR test conveys information about the feature resolution of the algorithms in order to distinguish the contents of each basket individually and separate abnormal baskets (e.g., an empty basket) from the UO_2 fully-filled baskets. The feature resolution can be tested by comparing the CNR value for a basket that accommodates UO_2 fuel assemblies with that for another basket filled with pellets of materials classified as non-hazardous, such as lead or copper. To test the size resolution, two randomly-chosen

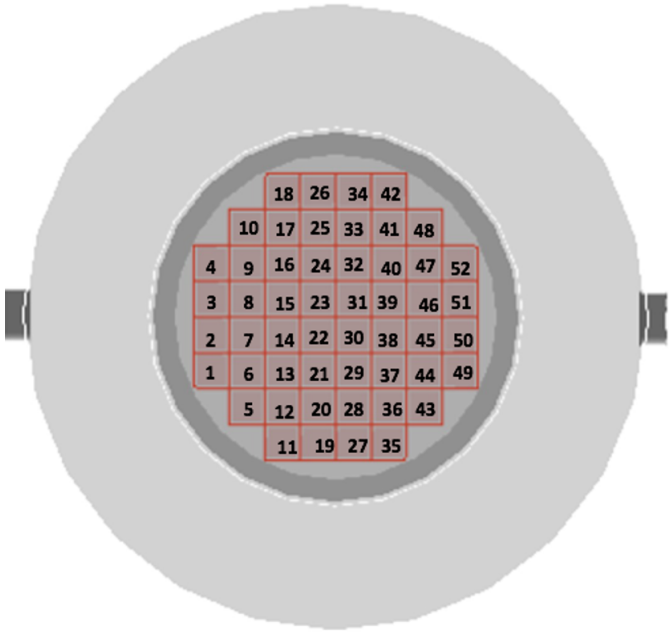

Figure 5.21: Top view of the V/52 CASTOR, showing all the baskets and labelling them with numbers from 1 to 52 (the lid and the base are removed for illustrative purposes).

baskets had up to 50% of their normal capacity unloaded. Half of the fuel assembles are removed from different positions inside each half-loaded basket, either from the side or the central-mounted fuel assemblies; comparing two regions of the half-loaded basket to the fully loaded basket assesses the ability of the algorithm to detect any irregularities within the basket to be evaluated.

For each of the non-standard (part loaded/material exchanged) baskets the comparison is made by calculating the discriminator for that basket and comparing it to the average discriminator for the eight neighbouring fully-loaded baskets.

It is important to understand the effect that the location of the fuel assembly basket inside the cask has on the CNR values for each algorithm. Hence, the target (abnormal) basket will be classified depending on its location inside the cask as either a central-area or side-area basket. Abnormal baskets are either filled with non-hazardous materials, half-loaded UO_2 fuel assemblies, or are completely empty. For the side-area basket study a single abnormal basket was placed in the side area of the cask (basket no. 7, see Figure 5.21) and then compared with the eight fully loaded fuel assembly baskets surrounding it for each of the fill scenarios detailed above (see Figure 5.21). Similar simulations for the same materials placed in a basket located in the central

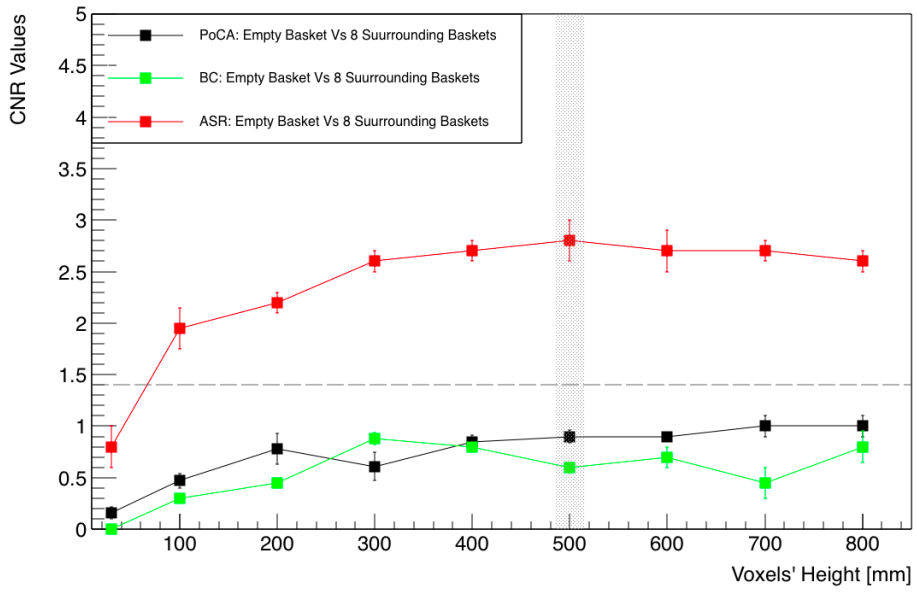

Figure 5.22: Comparison of the CNR value as a function of voxel height of all algorithms when differentiating between an empty basket against the eight surrounding fully loaded baskets. The grey box highlights the considered voxel height hereafter. The horizontal dashed-line represents the minimum CNR value in which the comparable regions could be distinguished from each other. Exposure time = 30 days.

area (basket no. 30) of the cask were also carried out for the central-area studies. Finally, for each target basket, the final value of the CNR is obtained by calculating the average of the CNR values measured when the material is positioned in the side and central areas of the cask.

5.4.3 Results and Discussion

This section presents the results of an extended study of the feature resolution of the reconstructed images in the presence of thicker and denser shields. Again, a number of scenarios are considered, namely a single target basket that is half-loaded with either UO_2 or a single target basket fully-loaded with either copper or lead pellets. The feature resolution is quantitatively represented here by the CNR value between the single target basket of interest and the eight fully-loaded UO_2 baskets that surround it. The PoCA and BC algorithms could not distinguish the empty basket from the eight neighbouring, fully loaded baskets with CNR values of 0.9 ± 0.1 and 0.6 ± 0.05, respectively. The

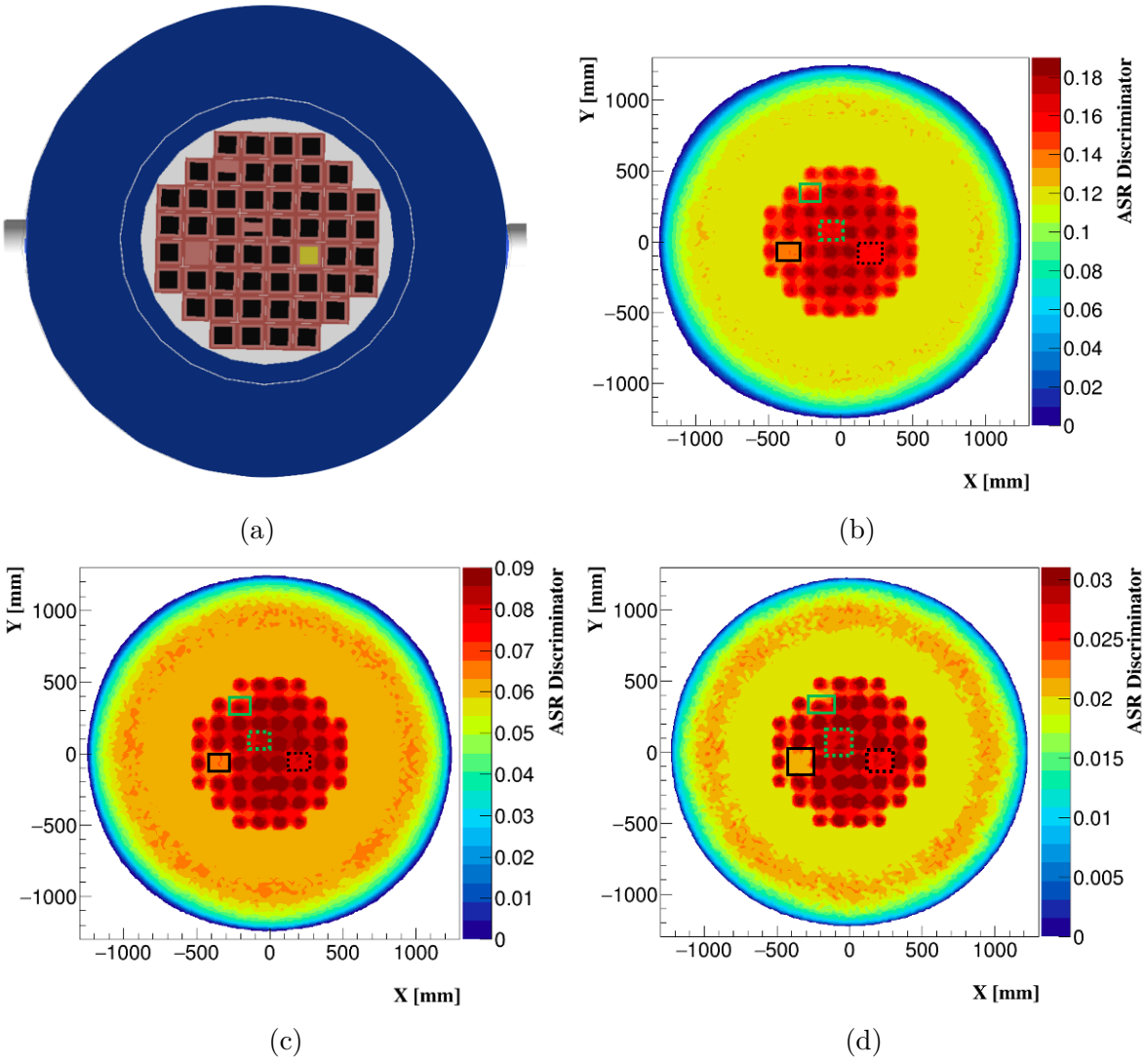

Figure 5.23: (a) top-view of the V/52 CASTOR showing four baskets which contain irregular contents. Comparison of the imaging of the cask's contents produced by the ASR algorithm when considering (b) 75%, (c) 50% and (d) 25% of the ASR discriminator in each voxel, respectively. The solid and dashed green boxes indicate the half-loaded baskets, while the solid and dashed black boxes indicate the baskets that contain no pellets and copper pellets, respectively.The exposure time was 30 days equivalent.

CNR values produced using several height of voxels showed that the incapability of these methods in imaging contests of V52 CASTOR, see Figure 5.22. It was shown that a fluctuation of the CNR values produced by the PoCA and the BC algorithms. This is likely caused by the PoCA assumption which approximates multiple scattering to one single instance of scattering, which results in poor approximation of the scattering

locations. This also impacts on the feature resolution capabilities of the BC algorithm which uses the scattering location of PoCA algorithm. This assumption mainly affects the vertical positions of the muon scattering, as the momentum component of the cosmic ray muons is much larger in the vertical direction; hence, fluctuations in the clustering values occur.

The ASR algorithm succeeds in minimising the smearing noise that results from the PoCA assumption. The performance of the ASR improved when the voxel height was increased from 30 mm to 500 mm, resulting in a 108% increase in the CNR values. Additional quantiles of 25% and 50% of the ASR discriminator distributions in each voxel are considered (see Figure 5.23). Comparing the empty basket with the eight surrounding fully loaded baskets produces a CNR value of 2.8 ± 0.4 when 75% of the discriminator distributions were taken in each voxel. However, considering the 25% quantile of each voxel distribution improves the CNR value to 5.0 ± 0.3. Therefore, hereon all quoted CNR results will use the ASR[25%] value.

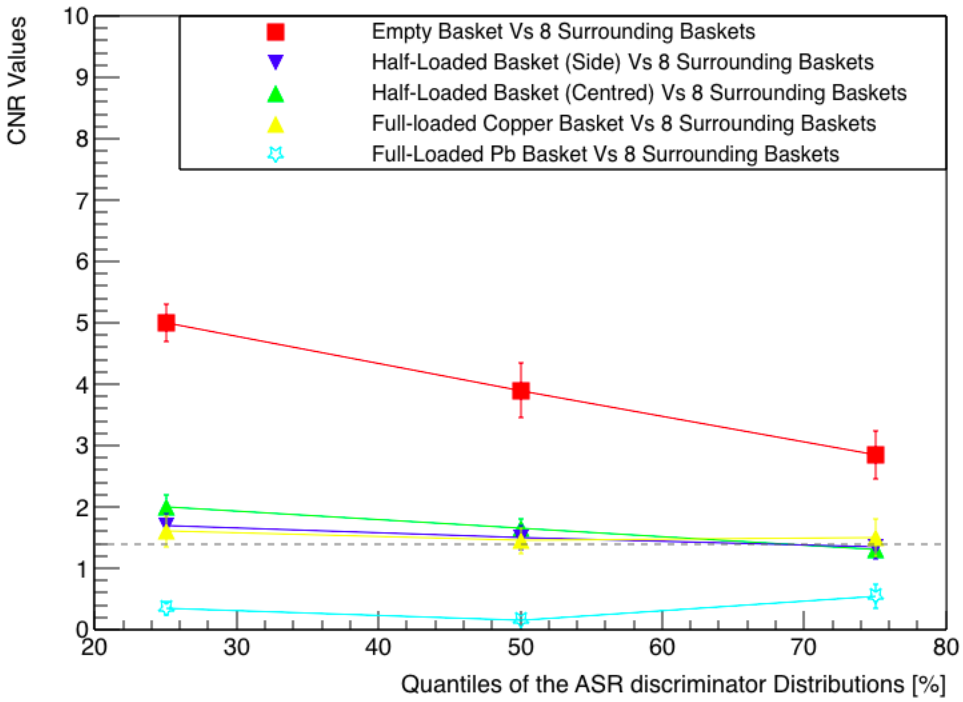

Figure 5.24: Comparison of the CNR values produced by the ASR discriminator when considering 25%, 50% and 75% of voxel's distributions after 30 days of muon exposure. The horizontal dashed-line represents the minimum CNR value in which the comparable regions could be distinguished from each other.

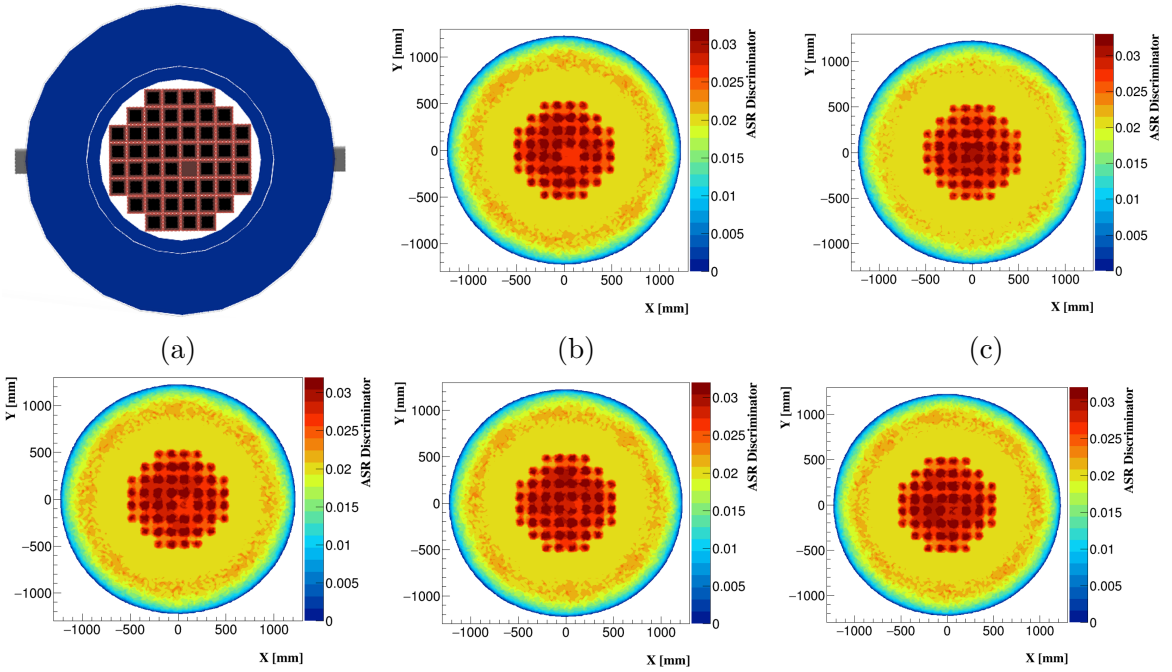

Figure 5.25: Comparison of the feature resolutions of the contents of basket number 30 when only 25% of the ASR discriminator's distributions are considered in each voxel. All figures indicate basket number 30 accommodating (b) no pellets, (c) fully-loaded with Pb pellets, (d) fully-loaded with Cu pellets, (e) half-sided and (f) half-centred. The exposure time was 30 days equivalent.

Figure 5.24 shows a comparison using 25%, 50% and 75% quantiles of the ASR distributions inside each voxel after 30 days of muon exposure time. As expected, the CNR values increase as the quantile decreases, the improvement being greatest for those material combinations where there is the greatest level of discrimination. The X-Y projections of the 52 baskets accommodating 51 full-loaded baskets with UO_2 fuel assemblies and one basket (number 30) accommodating the target materials are shown in Figure 5.25. Testing the size reliance of the target material was achieved by comparing half-loaded baskets to the eight baskets surrounding it. This shows the ability of the ASR method to separate the irregular contents of the basket. The CNR values from comparing half-unloaded (centered) and half-unloaded (sided) baskets to the eight fully loaded baskets appear to be just above the minimum distinguishable CNR level of 1.9 ± 0.2 and 1.6 ± 0.3, respectively. As expected, the regions of the basket filled with lead pellets and the surrounding baskets are not distinguishable (CNR $= 0.35 \pm 0.05$) due to the similarity of lead and UO_2 densities.

It is possible to use the CNR test to rapidly evaluate how the detector performance

might be affected when one of the operating conditions, such as the muon exposure time, is changed. The output density map of the ASR discriminator is shown in Figure 5.26 for between 4 and 20 days of muon exposure time. After 11 days of muon exposure time, the noise in the reconstructed density map renders the half-loaded baskets indistinguishable, with CNR values of 1.05 ± 0.2 and 0.93 ± 0.25 when half of the fuel assemblies are unloaded from the centre of the basket and from the side of the basket, respectively.

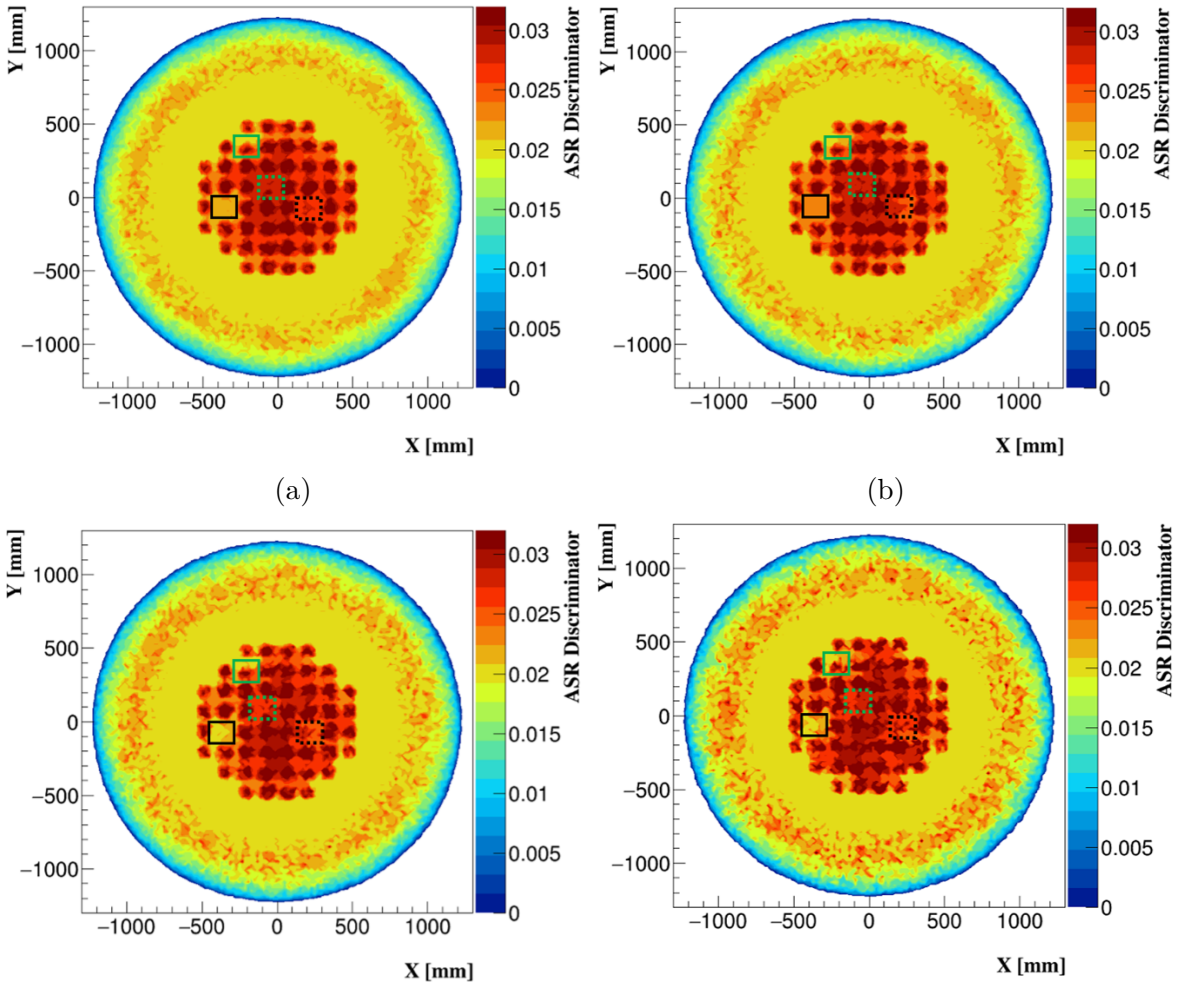

Figure 5.26: Comparison of the imaging the cask's contents produced via the ASR algorithm when considering 25% of the ASR discriminator in each voxel after (a) 20, (b) 11, (c) 8 and (d) 4 days of muon exposure time, respectively. The solid and dashed green boxes in indicate the half-loaded baskets, while the solid and dashed black boxes indicate the baskets that contain no pellets and copper pellets, respectively.

After 4 days of muon exposure time, the density maps are constrained by the detector's angular resolution and the fuel assemblies inside the image are smeared by the neighbouring baskets. Finally, in terms of the detector resolutions, the MST detector maintained its performance in locating the empty basket from the surrounding neighbouring fully-loaded baskets, after degrading the system's resolutions. For instance, after sixteen days of muon exposure time, the ability of the detector system to separate the empty basket from the eight surrounded baskets is degraded from a CNR value of 2.8 ± 0.2 to 2.2 ± 0.115, 2.0 ± 0.23, and 1.65 ± 0.25, when degrading the detectors' position resolutions by factors of 20, 50 and 80%, respectively. Figure 5.27 indicates the 2D outputs of the CASTOR contents with fifty one fully loaded baskets and a one empty basket (basket number 30) when using the default system's resolutions and the 50% degraded resolutions.

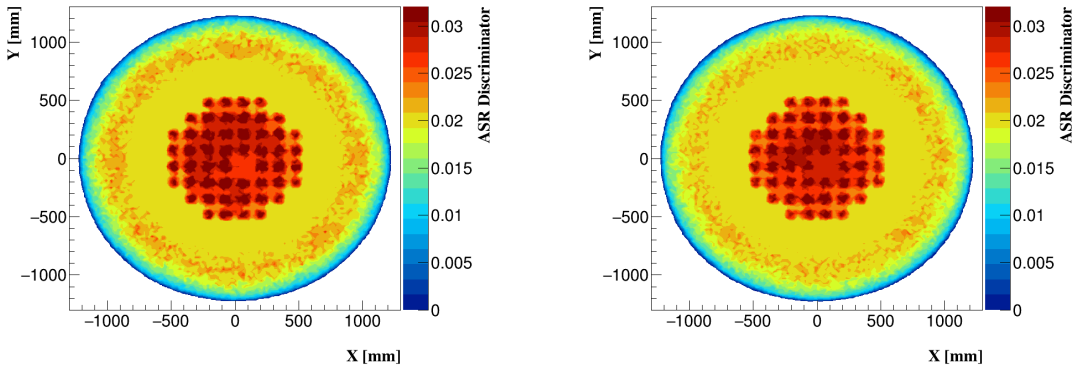

Figure 5.27: The 2D projected output of the target baskets reconstructed by the ASR algorithm using the default detector resolution (left) and after degrading the RPC and DC position resolutions by 50% of their default resolutions (right). The exposure time was 16 days equivalent.

5.5 Conclusion

A quantitative method was conducted to evaluate the performance of an empirical MST detector system in differentiating between high-Z and medium-Z materials. The CNR method was applied to assay three reconstruction algorithms in terms of their ability and limitations to differentiate between chosen target materials of different sizes,

positioned in different locations inside a small-cemented matrix drum and a large-scale CASTOR V/52 cask.

For the small drum, the CNR results conclude that the BC and the ASR algorithms were sufficiently capable of locating and differentiating between regions containing high-and medium-Z materials with side-lengths of 7, 10, and 13 cm against 4 regions containing background signal. The BC method performance improves gradually as the target material size increases with CNR values of 5.5 ± 0.2, 6.0 ± 0.12 and 7.1 ± 0.12 for 7, 10, and 13 cm side length uranium cubes, respectively. However, this performance degrades significantly, and the ability of the BC method is constrained, when the muon exposure time was shortened to two days with CNR values of 1.1 ± 0.04 and 0.9 ± 0.05 for copper and iron compared to background regions. This rendered the medium-Z materials indistinguishable from the background.

The ASR algorithm was shown to be more efficient in investigating target materials in a short time. All the materials investigated by the ASR lie above the distinguishable level (except Aluminium) even when the muon exposure time is as short as 2 days, with CNR values of 6.6 ± 0.2, 5.5 ± 0.1, 3.2 ± 0.15 and 2.6 ± 0.1 when comparing 10 cm side-length of uranium, lead, copper, and iron against background regions. Despite degrading the detector resolution to 700 micron for the RPCs and 4 mm for the DCs, the detector system has maintained the ability to separate the copper cube with 10 cm side-length from the background regions with a CNR value of 2.8 ± 0.2 after 4 days of muon exposure.

For the larger V/52 cask, the PoCA and the BC method failed to locate any of the irregular baskets that had 100% of their capacity unloaded, with CNR values of 0.9 ± 0.1 and 0.6 ± 0.05. The ASR method has been shown to be a good candidate for examining large and well-shielded materials. The ASR discriminator worked well to decrease the effects of the PoCA single-scatter assumption, and it demonstrated the ability to locate any irregularity within the fuel assemblies, such as empty, half-unloaded, and basket composite copper pellets. It was shown that the simulated detector system can locate any empty basket, whether it is located in the side or the centre of the cask, with a CNR value of 5.0 ± 0.3. Despite degrading the detector resolution to 525 microns for the RPCs and 3 mm for the DCs, the detector system has displayed the capability of the system in identifying the missing contents of any basket with a CNR value of 2.0 ± 0.23. The ability of the ASR algorithm to detect half-unloaded baskets is limited by the angular resolution of the detector when the cask's content is investigated with an exposure time of 11 days or less.

Chapter 6

Development of Reconstruction Algorithms for Materials Identification

Algorithms are important in the muon scattering tomography (MST) technique and are required to reconstruct a density map of the volume of interest. Several algorithms, most commonly the point of closest approach (PoCA), binned clustering (BC), and angle statistical reconstruction (ASR) algorithms, have already been proposed for imaging nuclear waste materials. The ability of these algorithms to reconstruct the muon trajectories was tested numerically in the previous chapter. The ability of MST in imaging well-shielded materials was shown in Chapter 5, and the strengths and limitations of the previous algorithms were addressed in Chapter 5. Promising results of ASR and BC algorithms in separating high- and medium-Z materials from the shielding matrix were also shown. The optimised previous algorithms showed the capability of localising the material's positions inside the drum with good approximation.

In this chapter, further work on the original ASR method is performed to improve the original ASR algorithm performance in material classification and is presented in Section 6.1. In addition, a new reconstruction algorithm is built to strengthen the ability of MST to identify materials for nuclear waste characterisation. This chapter introduces a new imaging method that builds on the concept of both ASR and BC algorithms (see Section 6.2). The position information of waste materials is obtained with good resolution using the new imaging methods. Subsequently, once the materials are localised, the next step is to identify them for nuclear waste characterisation. Classification between materials that have similarities in their properties, such as atomic

number, is challenging. Such materials are with $\Delta\ Z \leq 10.0$, e.g. uranium and lead ($_{92}U$ against $_{82}Pb$). This chapter also provides a method of classification of materials with similarities in Z number. A discrimination method between uranium, lead, and tungsten ($_{92}U$, $_{82}Pb$, and $_{74}W$) is presented. Furthermore, the performance of the discrimination method was also extended to discriminate between high-Z materials with $\Delta\ Z = 3.0$, such as astatine $_{77}Ir$ and $_{74}W$. The principle of this study is to gather information on specific materials that are highly likely to be present in nuclear waste drums. Hence, any unknown objects could be imaged and compared with the "reference materials"; thus, the target object could be discriminated.

Section (6.3.3) describes the method of using the multi-variate analysis (MVA) classifier tool [75] to discriminate between the object of interest using MST data. It also presents the performance of several classifiers in combination with the considered algorithms in discriminating between high-Z materials. The results of the discrimination between high-Z materials with different object sizes are presented in Section (6.7). Furthermore, the discrimination method is tested for different sizes of materials and several exposure times to understand the effects of the size and the scale time for each algorithm to discriminate between high-Z materials. Section (6.7) presents the results of using MST to identify materials according to the differences between their Z numbers. This chapter also investigates the effects of muon momentum on the algorithms' performance in terms of discrimination between high-Z materials. As explained in Chapter 4, the default measurement of muon momentum in this thesis is using smeared momentum with 50% as it is used in [76, 77]. Two additional approaches of muon momentum information to the default set-up are considered in this study, including Monte Carlo (MC) true momentum, and with no momentum information. Finally, the discussion and conclusion are given in Sections (6.7) and (6.8), respectively.

6.1 High-angle statistics algorithm

This section presents an optimisation of the original ASR algorithm developed by [74], which was previously explained in (Section 5.1.2). The sophisticated method of the ASR algorithm is the concept of determining which voxels along the muon path to apply discriminator scores throughout the volume of interest. This was achieved by defining a minimum distance (D_r) between the centre of a voxel (c) and the incoming and outgoing track fit lines, $a(z)$ and $b(z)$, respectively, and determined as;

$$D_r = \max(\min ||a(z) - c||, \min ||b(z) - c||) \tag{6.1}$$

A discriminator score is assigned to all voxels with D_r less than a chosen threshold distance (d_{th} = voxel's size). The discriminator scores are calculated using the projected angles (θ_x and θ_y), which are mathematically related to the deflected angle (θ) by ($tan^2\theta = tan^2\theta_x + tan^2\theta_y$). Using the magnitudes of the projected angles as independent variables provides access to more information on the scattering vertices in each voxel. Then, the final scores are assigned to all selected voxels as the third quartile of the distribution of the scores. This method showed promising results in imaging high-Z materials; thus, further steps were taken to optimise the ASR method.

Here, following the argument of the availability of muon scattering information obtained by the ASR method in each voxel. It is reasonable to consider a fixed number of scattering vertices in each voxel. For example, considering only N of the most scattered vertices per voxel might reduce the statistical error of the discriminator scores in each voxel. The scattering vertices in each voxel are sorted according to the projected angles of the corresponding muon, and the vertices with N of the largest scattering angles are kept. Any voxel containing a number of vertices less than N will be automatically discarded. Hence, an optimised version of the ASR algorithm is defined, which is a modification of the original ASR algorithm and is referred to as the high-angle statistics reconstruction (H-ASR) algorithm.

Algorithm setup

- Define 3D grid voxels in the volume of interest.
- For each voxel, v, generate an empty list S_v={}.
- Determine a minimum distance (a threshold), d_{th}, typically is equal to the voxel size.

For each muon

- Define the incoming $l(z)$ and outgoing $l(z)$ lines to detected hit positions, and fit the lines via least square.
- Calculate the projection of the deflection angles along x plane (θ_x) and y plane (θ_y).
- Sort vertices by descending normalized projected angles.

- Consider only the N high-ranked vertices, and generate scores, $s_1 = |\theta_x|\widetilde{p}$ and $s_2 = |\theta_y|\widetilde{p}$, where $\widetilde{p}$ is the momentum according to $\widetilde{p} = \frac{p}{p_{norm}}$, where $p_{norm} = 3$ GeV, and p is the muon momentum.
- Choose all voxels, such that the centre of these voxels is within a certain proximity (d_{th} = the voxel size) to either the incoming or outgoing tracks.
- Append the s_1 and s_2 scores to the list S_v.
- Sort the $k_v th$ value of S_v in ascending order, where k_v is equal to $q \times n$, where q and n are the size of S_v, and a chosen quartile, respectively.
- For each voxel v, the final score will be the value of k_v.

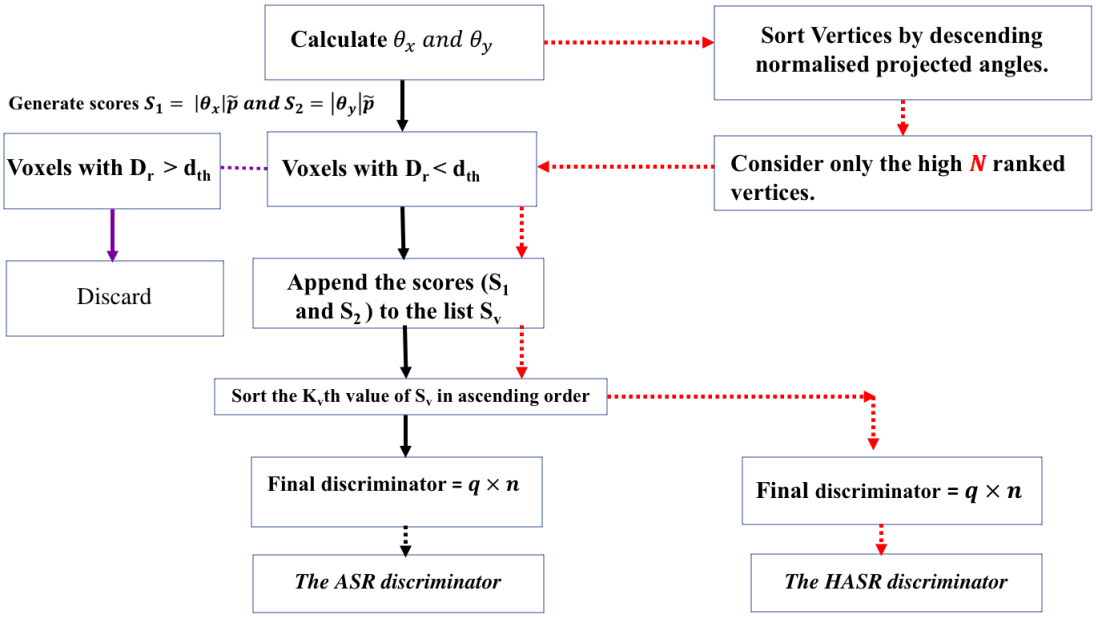

Figure 6.1: Comparison of flow charts indicating the final discriminator values assigned to each voxel for both the ASR (black arrow) and HASR algorithms (red-dashed arrow).

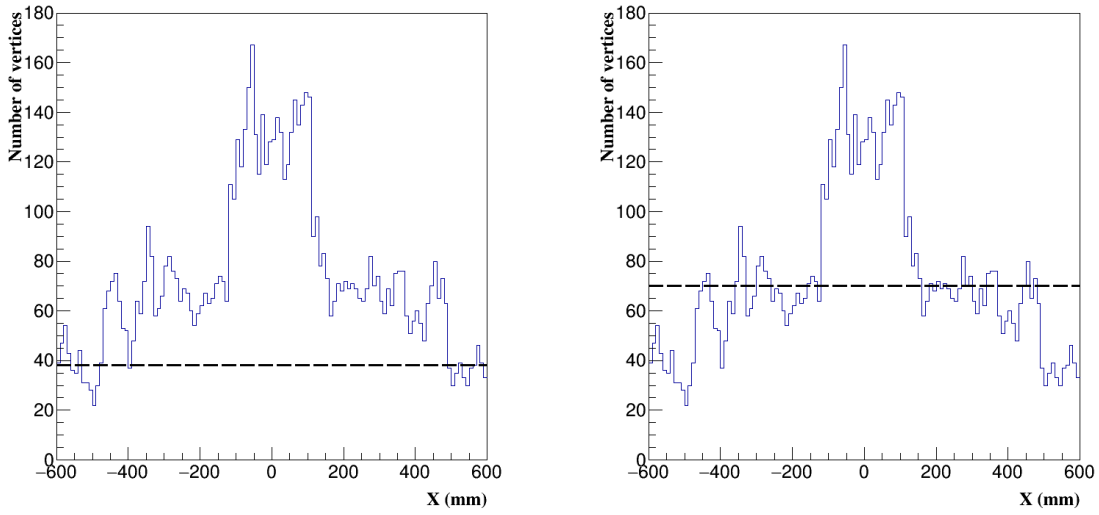

(a) (b)

Figure 6.2: The distribution of the number of vertices as a function of the position along X-axis. Higher number of vertices in the centre indicates the position of the uranium cube. The horizontal lines indicate the considered N showed in Figure 6.3.

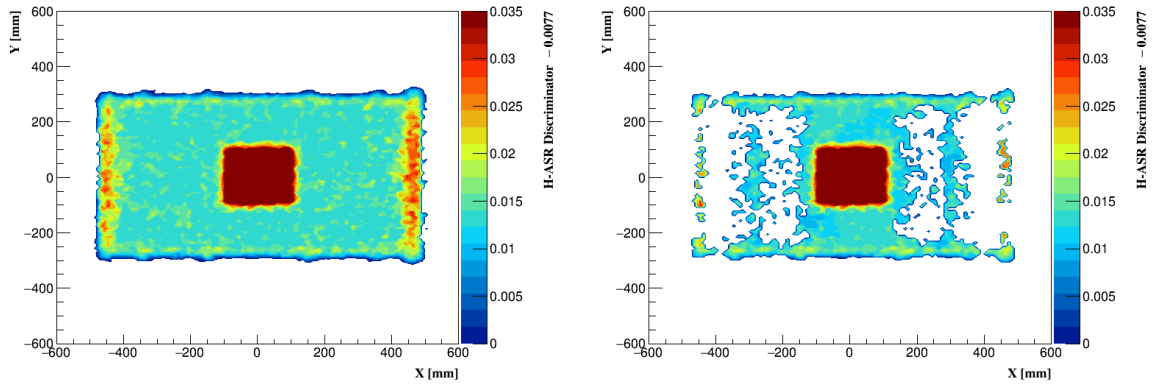

(a) (b)

Figure 6.3: The 2D projected output of the uranium cube with a side length of 20 cm reconstructed by the H-ASR algorithm when considering the 38 most scattered vertices (left) and the most 70 scattered vertices (right). The exposure time was 24 hours equivalent.

The fixed number N of scattering vertices is chosen according to a fixed muon exposure time. For 24 hours of muon exposure time, each voxel with dimension of (10 mm $\times$ 10 mm $\times$ 30 mm) contains a concrete matrix, with an average between 50 and 70

scattering vertices. However, as it is seen in Figure 6.4 voxels contain high-Z materials, with a number between 80 and 130 vertices per voxel. This means that for 24 hours of exposure time, some voxels containing concrete matrix are discarded if the $N \geq 70$, as these voxels do not have enough scattering vertices; thus, these voxels are removed from the reconstructed image, see Figures 6.3 and 6.2.

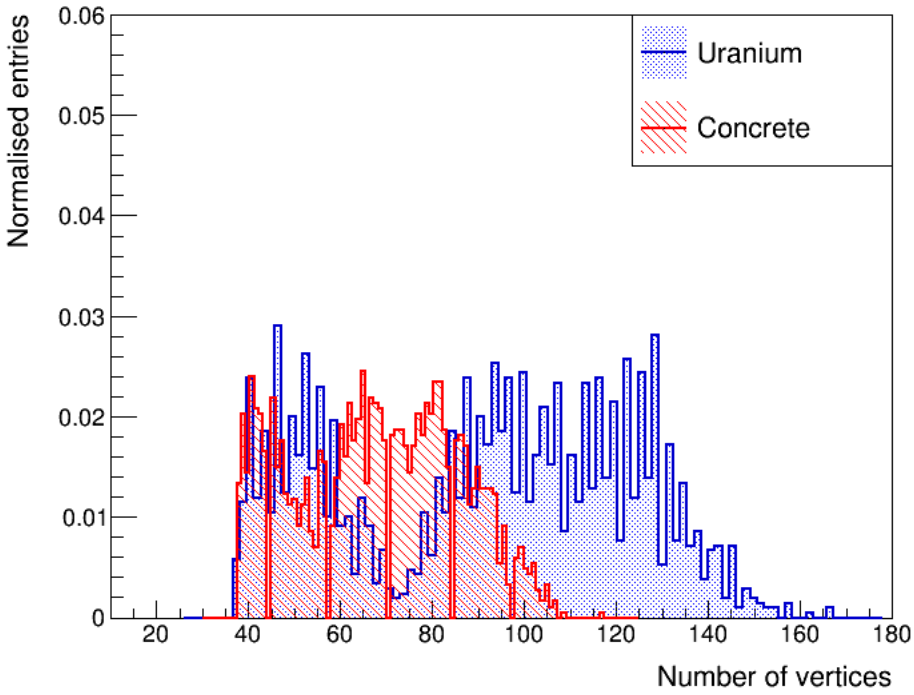

Figure 6.4: Comparison of distributions of the number of scattering vertices inside 20 cm cubes of uranium in blue, and inside equally-sized concrete matrix in red. Higher number of vertices corresponding to the vertices within the uranium cube.

For high values of N, it is understandable to see improvement in the contrast between high-Z materials and the shielding matrix, as more voxels containing the shielding materials are removed from the image, as these voxels fall below the cut. Furthermore, a high value of N also might underestimate the size of high-Z materials in the vertical direction, as the number of scattering vertices decreases due to muon absorption, and hence more voxels fall below the N cut. For this reason, the chosen N for 1, 2, and 4 days of muon exposure time are 38, 76, and 152, respectively.

A comparison of imaging a uranium cube with a side length of 20 cm embedded in a small nuclear waste drum using the ASR and the H-ASR algorithms is shown in

Figure 6.5. The figures show slices of the algorithm's discriminator through (xy) and (zy) directions, for the original ASR (left), the H-ASR with $N = 380$ (middle), and the H-ASR with $N = 500$ (right). The output of the ASR algorithm showed vertical smearing along the z direction, which is caused by the uncertainty in the scattering vertices for muons with small scattering angles along the z direction. This smearing along the z direction is reduced using the H-ASR algorithm, which is shown in Figure 6.5 after applying the N factor. However, choosing a high value of $N \geq 500$ for 10 days of muon exposure time affects the reconstructed image along the vertical direction, as more voxels do not have a number of vertices $n < N$; hence these voxels are eliminated. As a result, the size of the uranium cube along the z is underestimated. For this, the H-ASR algorithm considered 380 scattered vertices per voxel for 10 days of muon exposure time.

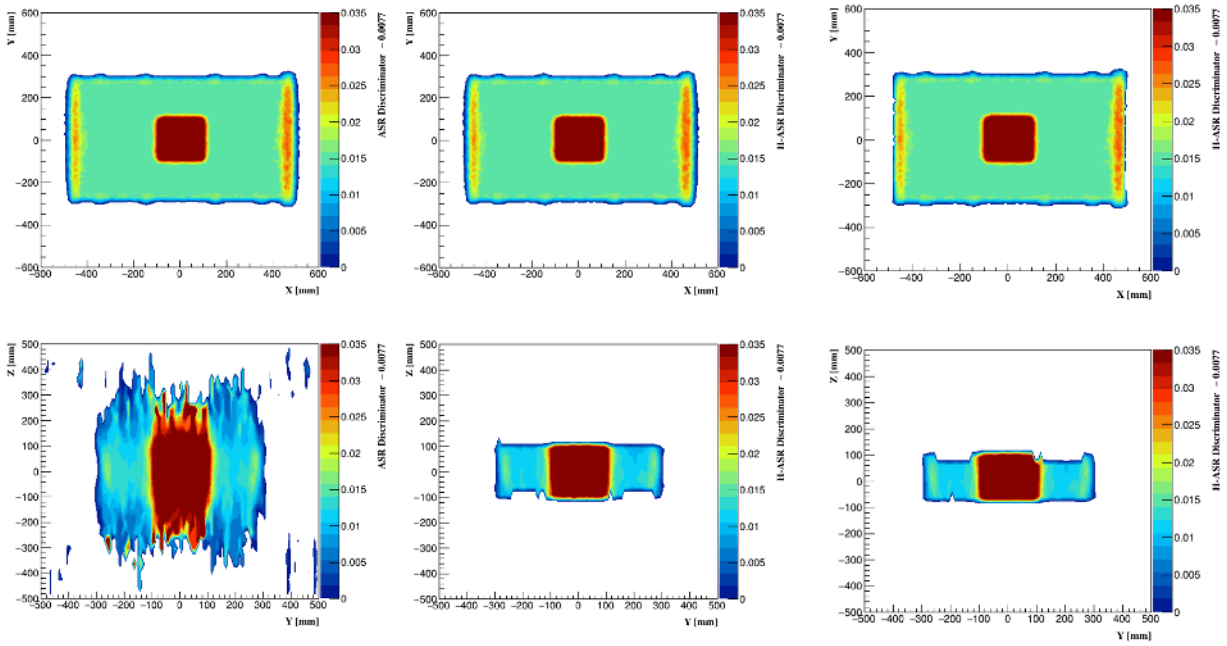

Figure 6.5: xy (above) and yz (below) slices of a 20-cm-side-length uranium cube from the ASR algorithm output (left), the H-ASR algorithm output when $N = 380$ (middle), and the H-ASR algorithm output when $N = 500$ (right). The ASR algorithm clearly shows smearing effects along the z direction; this smearing is caused by uncertainty in the scattering vertex along the vertical direction for muons with small scattering angles.

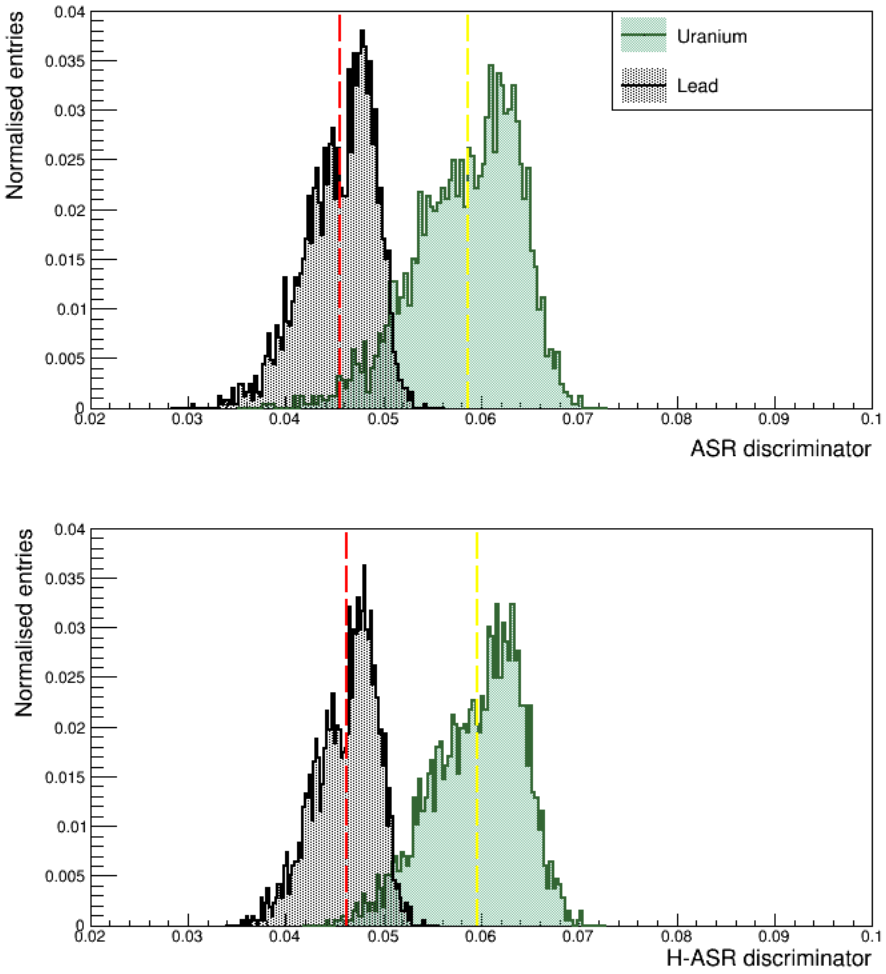

Figure 6.6: Comparison of distributions of the ASR (top) and the H-ASR (bottom) for 20-cm cubes of uranium and lead. The H-ASR considered the 380 most scattered vertices per voxel. The red and yellow dashed lines, respectively, represent the mean of the discriminator distribution for lead and uranium cubes.

Examples of the discriminator distributions of the ASR and H-ASR algorithms inside voxels containing 20 cm uranium and lead cubes are shown in Figure 6.6. Comparing the data set in the distributions clearly shows that the data in the H-ASR distributions of uranium and lead cubes are closely clustered around their mean, which in theory means a lower statistical error (σ). Statistically, applying the fixed number N of scattering vertices in each voxel reduced the errors in the discriminator distributions. Figure 6.7 compares the value of σ calculated using the ASR and the HASR discriminator distributions inside voxels containing uranium and lead cubes as a func-

tion of muon exposure time. Finally, in addition to the material distributions, more variables are extracted from the 3D density map of the inspected volume produced by the H-ASR algorithm and are considered to be used for material classification in Section (6.3).

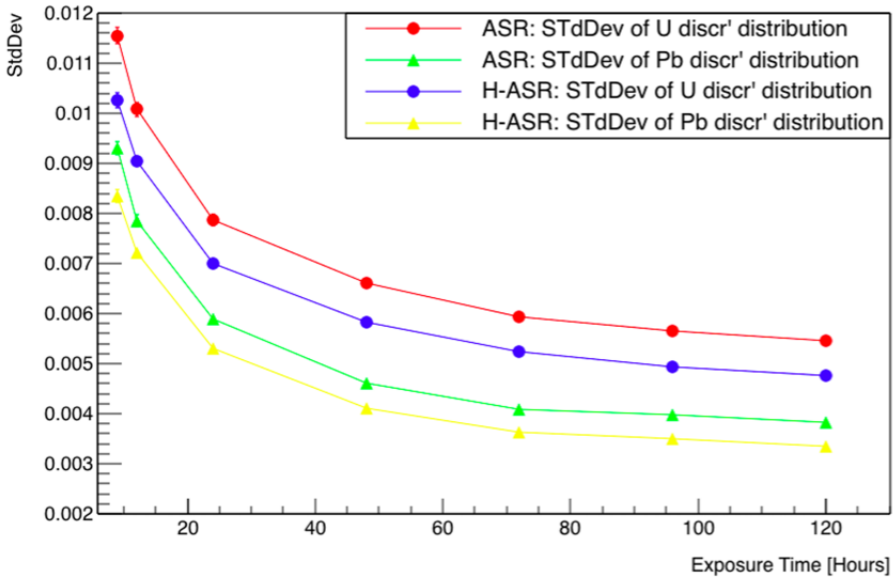

Figure 6.7: Comparison of error (σ) values in the discriminator distributions for voxels containing uranium and lead by the ASR and the H-ASR algorithms as a function of muon exposure time. The values of σ are reduced using the H-ASR after considering the 190, 152, 114, 76, 38, 18, and 14 most scattering vertices per voxel for muon exposure times of 120, 96, 72, 48, 24, 12, and 9 hours, respectively.

6.2 Hybrid algorithm

Based on the contrast to noise ratio (CNR) results shown in Chapter 5, a new algorithm was built based on a combination of the principles of BC and ASR algorithms. The BC algorithm is based on the fact that the density of high-angle scattering vertices is higher in high-Z materials. This can be explained as it only considers a fixed number of high scattering vertices (N) to calculate the metric distance between a pair of scattering vertices (v_i, and v_j) weighted by their scattering angle. In contrast, the density of high scattering angle vertices is expected to be lower in medium- and low-Z materials.

For each pair of vertices v_i and v_j within the investigated volume, a weighted

metric distance, $\widetilde{m_{ij}}$, is determined by

$$\widetilde{m}_{ij} = \frac{||V_i - V_j||}{(\theta_i \widetilde{p}_i) \cdot (\theta_j \widetilde{p}_j)} \tag{6.2}$$

where θ_i and θ_j are the scattering angles for muons i and j, respectively, in vertices v_i and v_j. While V_i represents the position of the scattering vertex v_i and V_j represents the position of the scattering vertex v_j. For muon i, p_i is the muon momentum of scattering vertex (v_i) and $\widetilde{p}_i$ is the muon momentum according to $\widetilde{p}_i = \frac{P_i}{P_{norm}}$, where $P_{norm} = 3\ GeV/c$.

The median of $log(\widetilde{m_{ij}})$ is set as the final discriminator for each voxel. This principle gives the BC method a good degree of localising different Z materials and thus can be a benefit in materials classification. However, as previously discussed, the principle of the BC algorithm in section 5.1.3 is that it uses the assumption of a single-scattering vertex assumed by the PoCA method. This makes it prone to additional noise due to the poor approximation of the scattering vertex position and, as a result, affects the material's classification performance of the BC algorithm.

The PoCA approximation of the scattering vertex was obviated by the ASR method by accounting for all voxels within a minimum distance (D_r) of the muon tracks reconstructed before and after the inspected volume, as discussed in the previous section. As a result, the noise inherited by the PoCA assumption was significantly reduced. The ASR method offers a good degree of accuracy in reconstructing the muon trajectories through the volume of interest. In theory, it is reasonable to combine the strengths of the BC (density of the scattering vertices) and the ASR (accurate scattering vertices reconstruction); hence, following the argument in this section, a new method is built and defined as the HyBrid (HB) algorithm.

Algorithm setup:

- Define 3D grid voxels in the volume of interest, which are used to store the 3D image values.
- For each voxel, generate three empty lists v_θ={}, v_{pos}={} and v_{disc}={}.
- For each muon, define the incoming $a(z)$ and outgoing $b(z)$ tracks to detected hit positions, and fit the lines via least square.
- Choose a threshold distance, d_{th}, typically is equal to the side-length of the voxel size.

- For each voxel, v, determine D_r, and scattering vertices with $D_r > d_{th}$ are discarded.
- Calculate the scattering angle, θ, from the incoming and outgoing muon tracks information.
- For each muon, append the scattering angles (θ) and the scattering vertices position to v_θ and v_{pos}, respectively. Here, v is all voxels containing vertices with $D_r < d_{th}$.
- For all v voxels, sort the scattering vertices in the lists v_θ and v_{pos} in descending order by normalised scattering angle (θ).
- Choose a value of N.
- Keep only the N largest scattering angles, any voxel containing a number of vertices $< N$, are automatically discarded.

For each voxel, and for every of the $\binom{N}{2} = \frac{N!}{2!(N-2)!}$ pairs of vertices, v_i and v_j:

- Calculate the weighted metric between V_i and V_j ($\widetilde{m_{ij}}$) using equation 6.2.
- Calculate the values of $log(\widetilde{m_{ij}})$, and fill the histogram with these values.
- Append the values of $log(\widetilde{m_{ij}})$ distribution to the list v_{disc}.
- Sort the values of $log(\widetilde{m_{ij}})$ distribution in the list v_{disc} in ascending order.
- The final discriminator value for the v voxel is calculated in ascending order (final discriminator value $= n \times q$), where n is the number of entries in the list v_{disc} and q is the chosen quartile, e.g. if $q = 0.5$, the median value is chosen as the final discriminator value.

The main principle of the HB algorithm is to overcome the main limitation of the BC method, which is not primarily caused by the calculation of the BC discriminator itself. However, it is inherited from using the single-vertex assumption of PoCA. In addition to this assumption of localising the scattering vertices, selecting the number of vertices as a track cut in each voxel would make it challenging to reconstruct low-Z materials in a short exposure time ($\backsim$ minutes). For example, in Section 5.4.1.2, the BC method fails to reconstruct medium- and low-Z materials in short muon exposure time, as

the muon track cut N condition discarded all voxels containing a number of vertices less than considered N. In theory, the single-vertex assumption can be obviated by applying discriminator scores to all voxels (with $D_r < d_{th}$) along the muon's path. Subsequently, more scattering vertex information is gained in each voxel, which means that the N factor becomes more applicable in the case of short muon exposure time.

In the case of the HB method, more scattering vertex events are expected to occur in each voxel; this should resolve the BC failure of reconstructing of low-density materials in such a short muon exposure time. However, the relation between the clusters' density of scattering vertices and the Z number of the reconstructed material is kept in the HB method as voxels containing high-Z material expect a higher density of scattering vertices than voxels containing medium- and low-Z materials.

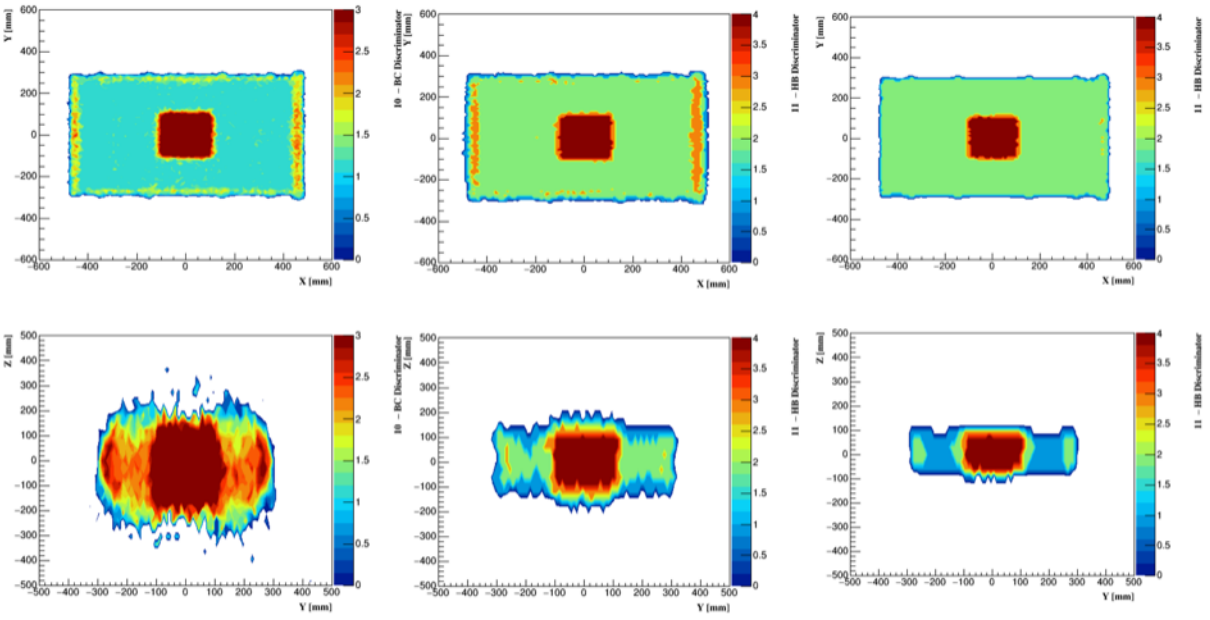

Figure 6.8: xy (above) and yz (below) slices of a 20 cm-side-length uranium cube from the BC algorithm output (left), the HB algorithm output when $N = 20$ (middle), and the HB algorithm output when $N = 250$ (right). The BC algorithm clearly shows smearing effects along the z direction; this smearing is caused by uncertainty in the scattering vertex along the vertical direction for muons with small scattering angles.

A comparison of imaging a uranium cube with a side length of 20 cm embedded in a small nuclear waste drum using the BC and HB algorithms is shown in Figure 6.8. The figures show slices of the algorithms' discriminator through (xy) and (zy) directions, for the BC method (left), the HB with $N = 20$ (middle), and the HB with $N = 250$ (right).

Vertical smearing along the z direction is shown in the BC output, which is caused by the uncertainty in the scattering vertices for muons with small scattering angles along the z direction. However, the reconstructed image in the yz direction is less affected by the HB method output. This can be understood as the HB discriminator scores are used as a number of the most scattered vertices N of the discriminator distribution in each voxel. Similar to the H-ASR algorithm, vertical smearing is slightly reduced when considering the higher N of the most scattering vertices per voxel. Figure 6.9 shows examples of the discriminator distributions of the BC (top)

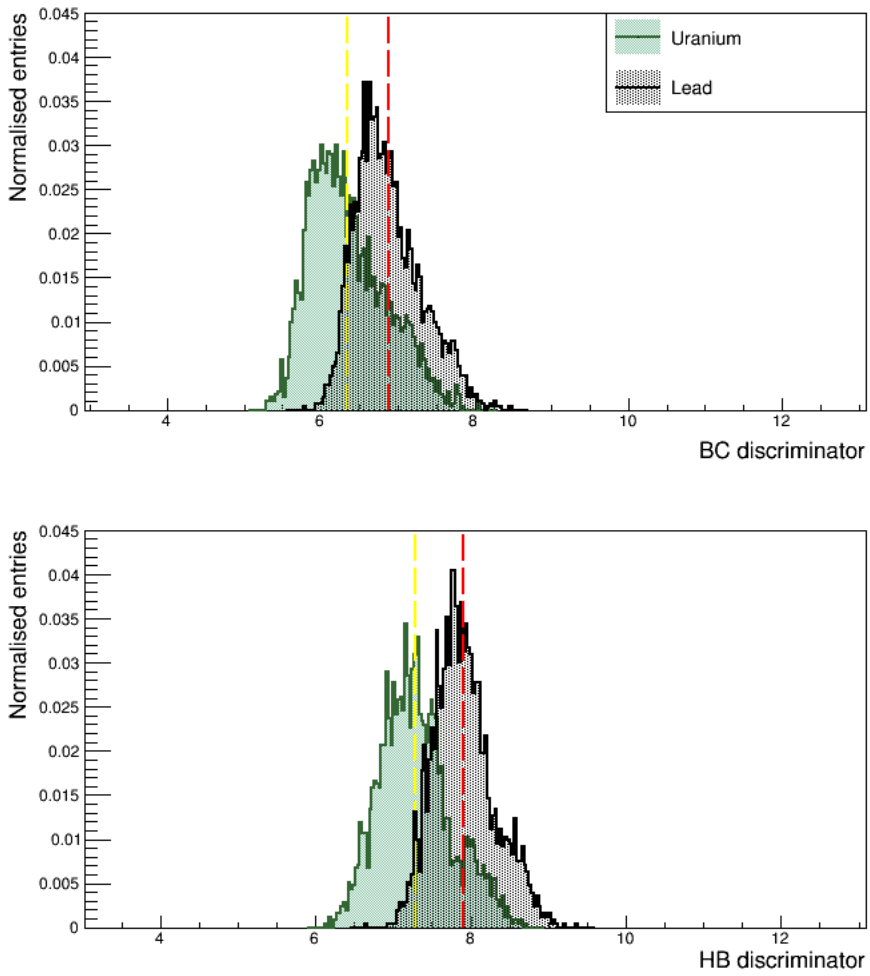

Figure 6.9: Comparison of distributions of the BC (top) and the HB (bottom) for 20 cm cubes of uranium and lead. Both methods considered 20 most scattered vertices per voxel. The red and yellow dashed lines, respectively, represent the mean of the discriminator distribution for lead and uranium cubes.

and HB (bottom) algorithms inside voxels containing 20 cm uranium and lead cubes.

Higher discriminator values correspond to lead cubes. Even though the HB method can separate the comparable distributions by increasing the N factor, the N of most scattered vertices is kept the same for both algorithms. Moreover, choosing a very high number of N could lead to an underestimation of the target's size, especially in the vertical direction. This can be seen in Figure 6.8 (bottom right) and the uranium cube is shrunk when the number of scattering vertices rose to 250 for 10 days of muon exposure time. Even though the HB method offers more scattering vertices in each voxel, as this chapter compares the HB discrimination performance to that of the BC algorithm, the N number will be kept as it was used in the BC algorithm, example in [77]. To avoid human-eye bias, the errors of the voxel distribution containing uranium and lead are calculated for different exposure times (see Figure 6.10). The errors in the distributions produced by the HB showed that the HB method was slightly affected by reducing the exposure time. The BC showed a sharp increase in the errors of the distribution of the material when the exposure times were lower than 24 hours. Finally, the HB algorithm is applied in this thesis to classify nuclear waste materials in the next section.

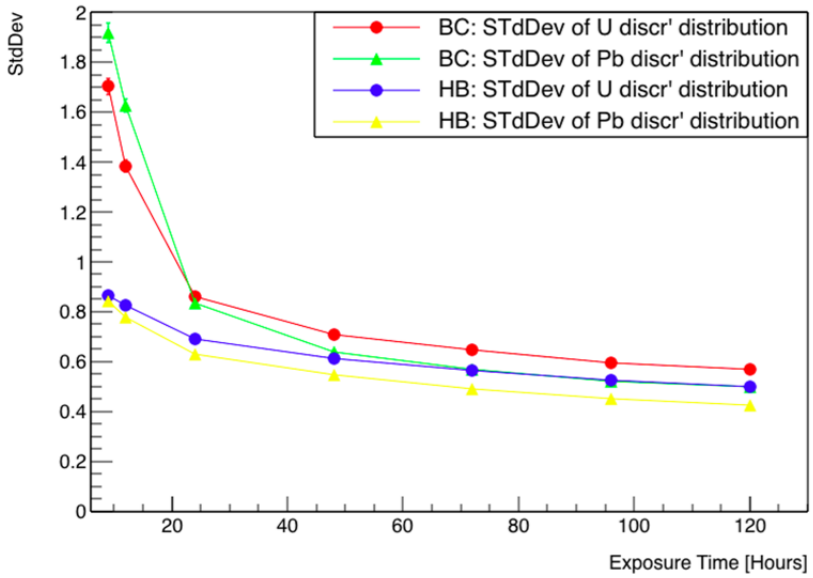

Figure 6.10: Comparison of error (σ) values in the discriminator distributions for voxels containing uranium and lead by the BC and HB algorithms as a function of muon exposure time. The values of σ grow significantly for muon exposure time of less than 24 hours. Both algorithms considered 10, 8, 6, 5, 4, and 4 most scattered vertices per voxel for 120, 96, 72, 48, 24, and 12 hours, respectively. Notice that for 9 hours of muon exposure, the 4 most scattered vertices are also chosen for both algorithms.

6.3 Discrimination materials for nuclear waste characterisation

Classification of waste materials was performed using MVA classifiers, which were trained and analysed using TMVA, a CERN ROOT package . Multiple classifiers are available in TMVA, and they can be trained simultaneously. All classifiers' performances can be compared quantitatively using a receiver operating characteristic curve (ROCc). This can be performed by plotting a curve of a true positive rate against a false positive rate, and the area under the curve (AUC) is calculated. The true positive rate corresponds to the classifier correctly identifying the signal, while the false positive rate corresponds to the classifier incorrectly identifying the background as a signal. The AUC value indicates the performance of the classifiers applied, in which the perfect classifier produces AUC with a value of 1.0. Conversely, when the classifier produces an AUC equal to 0.5, this indicates that the data were randomly classified. In this thesis, an AUC produced by a classifier with a minimum value of 0.95 will be considered a good discriminator performance. The statistical error of the AUC values will be calculated using the 95% confidence intervals used by Hanlley and McNeil [78]. More details of simulated waste materials, muon momentum information, and MVA classifiers are presented in this section.

6.3.1 Simulation of High-Z Materials

All the materials used for materials classification were simulated using Geant4 with the same settings, as described in 4.2, of simulation cosmic muon, MST detectors, and waste drums. The materials were simulated mainly in cubic shapes with different side lengths of 20, 10, and 5 cm. The materials considered here have $Z > 70$, specifically, uranium, lead iridium, and tungsten. In terms of data-taking time, different exposure times were also compared to understand the scanning time of waste drums depending on the size of the waste materials.

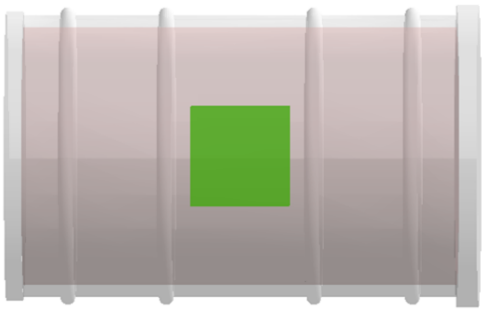

Figure 6.11: An example of a 20-cm-side-length uranium cube used for materials classification by MVA classifiers.

6.3.2 Muon momentum information

Muon momentum is an important variable in the simulated MST data and classification analysis, (see section 4.3). The most common methods were used in MST data analysis, as in [69, 76, 77]. These methods were used in this chapter as follows: a Monte-Carlo truth momentum, adding smearing of random values of Gaussian distributions with 50% of the truth momentum (default set-up), and with no momentum information. The default set-up uses the 50% smeared momentum for the results stated in this chapter, except where stated of using the two other methods.

6.3.3 Multi-variate Analysis

The MVA classifiers use a combination of several variables of data to classify between any two or more comparable materials. To test the classifiers' performances available in TMVA, 10 days of muon exposure time simulations of two nuclear waste drums containing uranium and lead cubes with side lengths of 20 cm were performed. Only the data inside the voxels containing the comparable cubes were passed to the MVA classifier. The outputs of the MST track data reconstructed by the BC, HB, ASR, and H-ASR algorithms were individually passed to the MVA classifier. The N factor of the BC, HB, and H-ASR were, respectively, set to 20, 20, and 380.

The MVA classifiers allow the use of a number of input variables with no limits. In this chapter, the variables considered for the MVA classifiers were extracted from the outputs of the BC, HB, ASR, and H-ASR algorithms. The main variables were obtained from each algorithm output, e.g. the discriminator's value distribution (see Figures 6.6 and 6.9), the distributions of the scattering angles (θ, θ_x, and θ_y), and the muon

momentum distributions. Furthermore, additional variables were extracted from the discriminator's value distribution of each algorithm by re-binning these distributions into 25 bins and then calculating the normalised bin counts to be used as additional input variables.

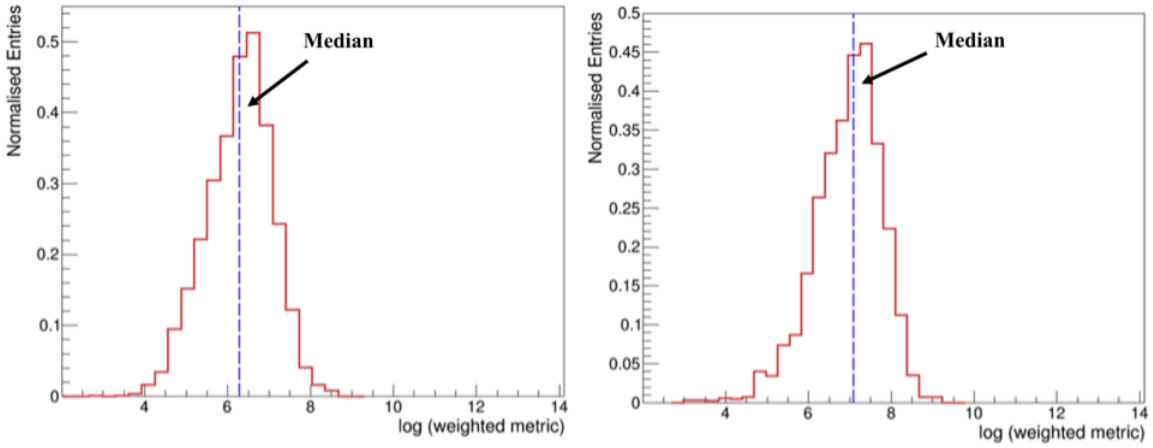

Figure 6.12: Comparison of distributions of the $log(\widetilde{m_{ij}})$) produced by the HB method for a voxel containing uranium (left) and lead (right). The blue-dashed line represents the median of the distributions, which is set as the discriminator value in the HB algorithm output image.

As explained in the algorithm methods, each algorithm assigns discriminator values for each voxel. The BC and HB algorithms use the median of $log(\widetilde{m_{ij}})$; however, the bin counts used as input variables were calculated using the distribution of $log(\widetilde{m_{ij}})$, (see Figure 6.12 for the HB log(metric) distribution). These bin counts were used as input variables for the application of the MVA materials classification. Example distributions of some of these variables used for the MVA classifiers to classify between uranium and lead are shown in Figure 6.13.

The ASR and the H-ASR use the third quartile of the discriminator value distribution in each voxel. These final distributions of the ASR and H-ASR methods were used to calculate the bin counts and then used as additional variables for the MVA classifiers (Figure 6.14 indicates the H-ASR discriminator distribution). Figure 6.15 shows an example of the bin count input variables inside voxels containing uranium and lead for the H-ASR method, which was used to train the MVA classifier. All the described variables, including the main and the additional, were used as inputs into the MVA to discriminate between the uranium cube as a signal and the lead cube as a background. The data sets were trained using multiple MVA methods, and the performance of each method was quantified using the ROC curve. The ROC curve used to understand the performance of each MVA method is a plot of a background rejection

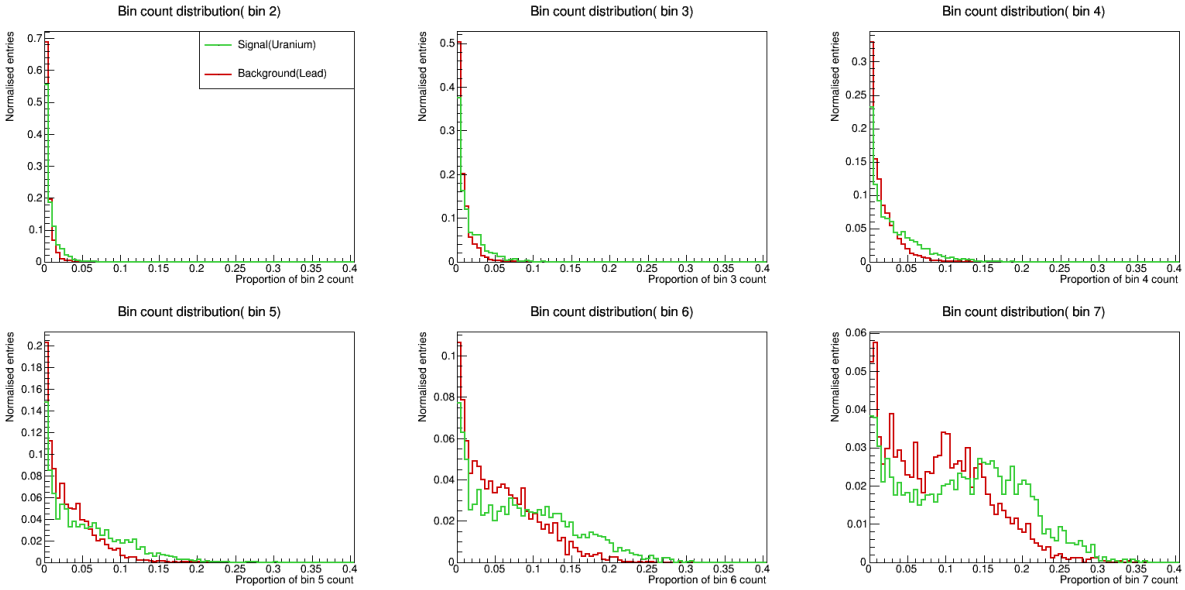

Figure 6.13: Comparison of some bin count distributions of the HB method used as input variables to train the MVA classifiers. These distributions were extracted from the normalised bin counts shown in Figure 6.12. The green line represents voxels containing a 20 cm uranium cube (set as a signal), and the red line represents voxels containing an equally sized lead cube (set as a background).

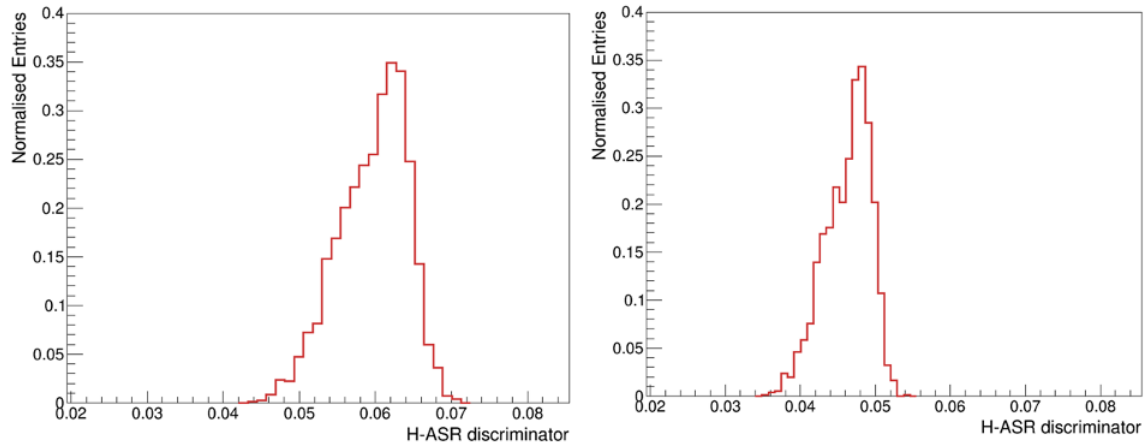

Figure 6.14: Comparison of distributions of the H-ASR discriminator for a voxel containing uranium (left) and lead (right). The normalised bin counts of these distributions are calculated and passed to the MVA classifiers.

against the signal efficiency (see Figures 6.17 and 6.18). The AUC results reveal the most suitable MVA method for training the data sets, which is expected to produce the highest AUC compared to the other methods. The ROC curve interprets the clas-

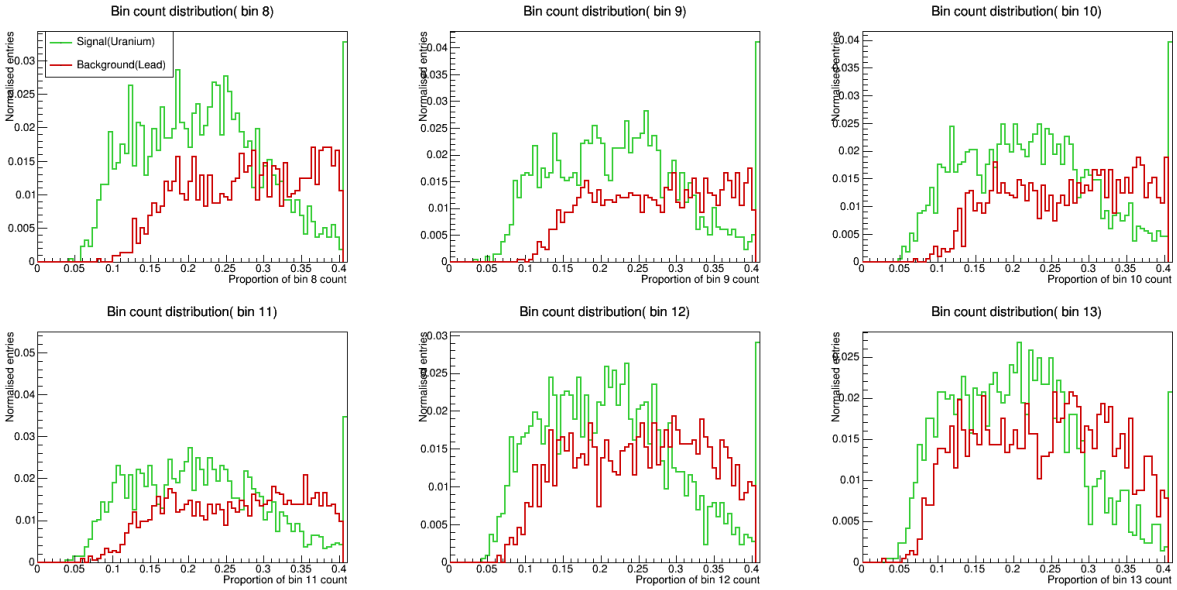

Figure 6.15: Comparison of some bin count distributions of the H-ASR method used as input variables to train the MVA classifiers. These distributions were extracted from the normalised bin counts, as shown in Figure 6.14. The green line represents voxels containing a 20 cm uranium cube (set as a signal), and the red line represents voxels containing an equally sized lead cube (set as a background).

sification performance of each MVA method when applied to the BC, HB, ASR, and H-ASR algorithm variables to discriminate between the signal and the background.

6.4 MVA methods

6.4.1 Boosted Decision Tree (BDT)

The BDT method classifies events by constructing a decision tree (see Figure 6.16), which can be visualized as a ”flow-chart”, starting at the root node from the top. From this root node, the classifier divides the data into a sequence of binary splits, each determined by the distinguishing variables. At every node, the next branch is chosen based on a cut-off point on one of these variables, continuing in this process until the final leaf node is reached. During this process, repeated “yes” or “no” decisions are made for each individual variable until a final determination of either ”signal” or ”background” is achieved.

6.4.2 Gradient-Boosted Decision Tree (BDTG)

Using a single tree in the BDT method makes it susceptible to statistical fluctuations in the training sample. This vulnerability can be countered by creating a forest of trees, which consists of a large number of trees. Further steps can be taken to enhance the classifier performance, one of which is using the gradient-boosted decision tree (BDTG). The BDTG method augments the BDT method's efficiency by merging the weak classifiers from the trees into a unified, stronger classifier.

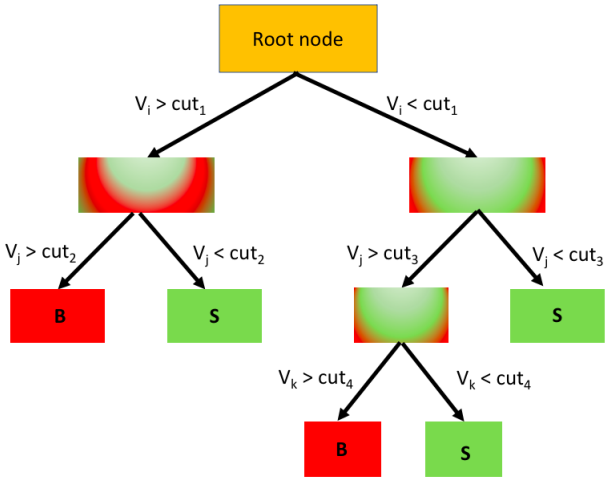

Figure 6.16: Schematic representation of the decision-tree structure illustrates the principle: starting at the root node, the data branches out based on the input variables V_i. At each node, the input variable that best separates the data into signal and background categories after the designated cut-off is applied. The tree culminates in terminal nodes labeled as "S" for signal or "B" for background, depending on the predominant category of events within those nodes.

6.4.3 Multi-Layer Perceptron (MLP)

The MLP method is natural artificial neural network (ANN). It basic structure consists of 1 input layer, $\geq$ 2 hidden layers and an output layer, with 1 or more nodes ("neurons") for each layer. The data or features are input into the input layer, and they progress in a feed-forward manner through the hidden layers to the output layer. The output layer provides the final classification result.

6.4.4 Linear Discriminant analysis (LD)

The basic principle of the LD method is using a linear model in classification between data, in which project the data into lower-dimensional space in a way that maximise the separation between classes. The term "linear" indicates that the linear discriminant function (y_x) is linear with respect to the parameters β as $y(x) = x^\top \beta + \beta_0$, where β_0 represents the bias. Hence, the $y_x \geq 0$ is classified as a signal, while those with $y_x < 0$ are categorized as background.

6.4.5 Fisher Linear Discriminant and Boosted Fisher

The principle of the Fisher method is almost similar the LD method principle, in which it aims to maximize the separation between the classes. Basically, it seeks to find a linear combination between of variables that best separates 2 or more classes. An improved method of the original Fisher method is called "BoostedFisher". The process of Boosting is a general ensemble method that creates a strong classifier from multiple iterations of a weak classifier. The idea is to apply a sequence of weak classifiers (e.g. in the Fisher classifiers) iteratively. Thus, each new classifier focuses on the events that were misclassified by the previous ones.

6.4.6 Likelihood

The Likelihood method is a probabilistic approach to classification. Based on the training data, and for or each input variable, separate histograms are created for signal and background classes. From these histograms, the probability density functions (PDFs) for signal and background of the input variables. The likelihood (L_i) for an event to be either signal or background is computed by multiplying the probability of all its variables: $L_s = \Pi_i p_s(x_i)$, $L_b = \Pi_i p_b(x_i)$, where $p_s(x_i)$ and $p_b(x_i)$ are the probabilities of the i_{th} variable for signal and background.

6.4.7 Functional Discriminant Analysis (FDA)

The FDA is a classification method in which it fits function to the data to achieve maximum separation between the signal and background classes. It aims to determine the function parameters, such that the output of the function provides a clear discrim-

ination between the classes. The FDA_GA uses a Genetic Algorithm (GA) to optimise the parameters of the discrimination function of the FDA method.

The BDTG was shown to be the most suitable method with AUC results of 0.851, 0.987, 0.999, and 1.0 when applied to the BC, HB, ASR, and H-ASR algorithms, respectively, (see Figures 6.17 and 6.18). Hence, the BDTG is applied as the default MVA method for the materials classification hereafter.

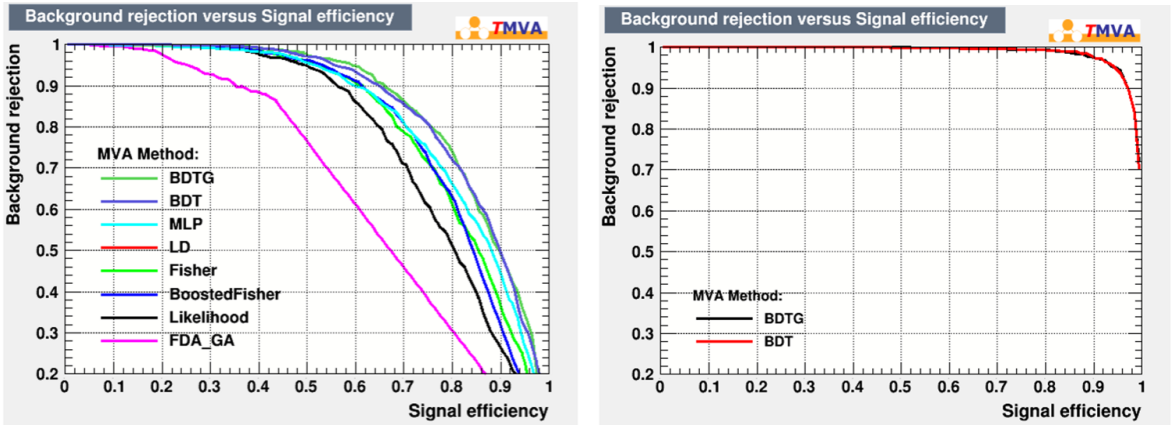

(a) (b)

Figure 6.17: The ROCc plots of background rejection as a function of signal efficiency for multiple TMVA methods when applied to the BC algorithm variables in (a) and when applied to the HB algorithm variables in (b). The most suitable MVA methods are listed from top to bottom. As the HB algorithm is compared to the BC algorithm, the two high-ranked MVA methods are applied to the HB algorithm variables, see Table 6.1.

6.5 MVA binary and non-binary classifiers

The MVA classifiers are applied to identify voxels containing signals from voxels that contain background. In terms of binary classification, the classifier assigns one data set of voxel variables as a signal and another data set of voxel variables as a background. The non-binary classification designates a single data-set voxel variable as a signal and multiple data-set voxel variables as a background. In both cases, the classifier tries to separate signal voxels from background voxels. Hence, when the classifier is applied to a "random voxel", it can correctly classify the voxel contents as a signal or background depending on the contents' variables and the performance of the classifier.

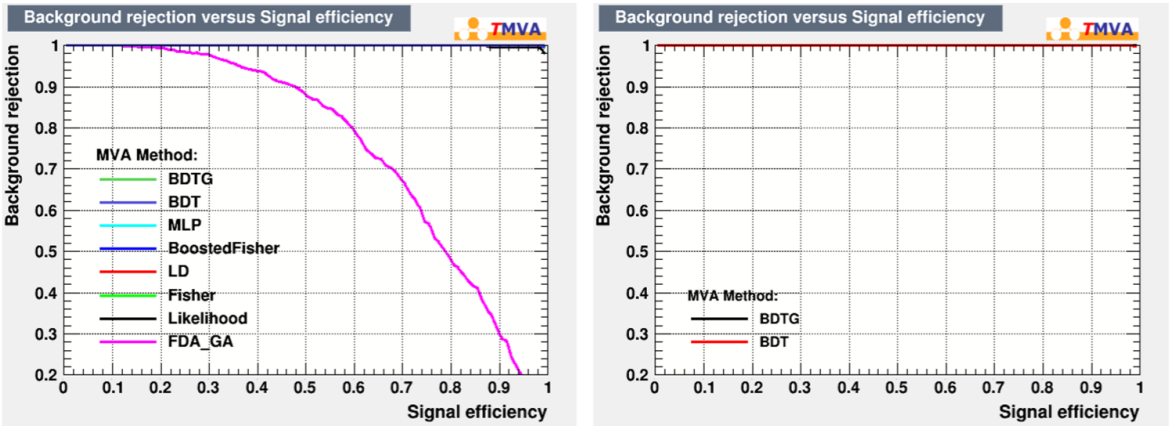

(a) (b)

Figure 6.18: The ROCc plots of background rejection as a function of signal efficiency for multiple TMVA methods when applied to the ASR algorithm variables in (a) and when applied to the H-ASR algorithm variables in (b). The most suitable MVA methods are listed from top to bottom. As the H-ASR algorithm is compared to the ASR algorithm, the two high-ranked MVA methods are applied to the H-ASR algorithm variables, see Table 6.1.

The TMVA classifiers split the data randomly into two equally sized sets, which are "training" and "testing" sets. The classifier is trained on the training set, and then it checks over-training by applying it to the testing sets. The classifier plots two distributions of signal and background for both training and testing data sets as a classifier response (see Figures 6.17) and 6.18). It also calculates a cut value (optimum cut) where all values above this point are assigned as "signal-likeliness" and all responses below the optimum cut are assigned as a "background-likeliness". The optimum cut for two classes can be calculated using ROC curve which corresponds to the point positioned at the furthest top-right point. At this position, the combination of signal efficiency and background rejection is likely maximized. The optimum cut is defined in TMVA as the point at which the signal efficiency and the background rejection (1 − background efficiency) are equalised. This point in the ROC curve corresponds to the point that has a maximum Youden index [79], in which this point is defined as signal efficiency + background rejection − 1. On the ROC curve, the Youden index is the distance between the ROC curve and the diagonal line connecting the points (0, 1) and (1, 0), measured vertically from the curve to this diagonal.

In machine learning, over-training is a frequent issue in classification models. This means that over-training occurrs when the model performs poorly when the "unseen-data" is applied to the model, compared to performance when the test data is applied

Cube Size	**20 cm × 20 cm × 20 cm**	
TMVA method / **Algorithm**	**BDTG**	**BDT**
HASR	**1.0**	**1.0**
ASR	**0.999**	**0.998**
HB	**0.987**	**0.985**
BC	**0.851**	**0.85**

Table 6.1: AUCs of the ROC curves for background rejection, plotted as a function of signal efficiency, for the top two high-ranked MVA methods when applied to variables from the HASR, ASR, HB, and BC algorithms (see Figures 6.17 and 6.18).

to train the model. Subsequently, the capability of the classifier is significantly reduced in terms of discriminating events compared to the performance when the "training" data-set is applied. This can lead to a misinterpretation of the classifier's efficacy when evaluated using the training data. This can be addressed by reducing the statistical fluctuation by providing more samples of training data. Furthermore, over-training can also be occurred in some classification methods, as some method like Boosted Decision Tree (BDT) is more prone to a degree of over-training. However, this can be mitigated using some technique, e.g. nodes with little discriminatory power in the tree can be removed through the process of "pruning" nodes [75]. In addition to the visual comparison between the classifier outputs of training and testing data-set distributions, a further test (a Kolmogorov–Smirnov test) is performed to check over-training quantitatively. This test revealed how the training distributions fit the testing distributions. The values produced by the Kolmogorov–Smirnov test showed that some over-training took place, especially in the classifier's responses when using the BC and the H-ASR data-set variables (see Figures 6.19 and 6.20).

6.6 Muon momentum effects on materials classification

To understand the effects of muon momentum information on material classification, binary uranium/lead BDTG classifiers are trained using voxel variables containing a 20 -cm-side-length uranium cube against voxel variables containing an equally sized

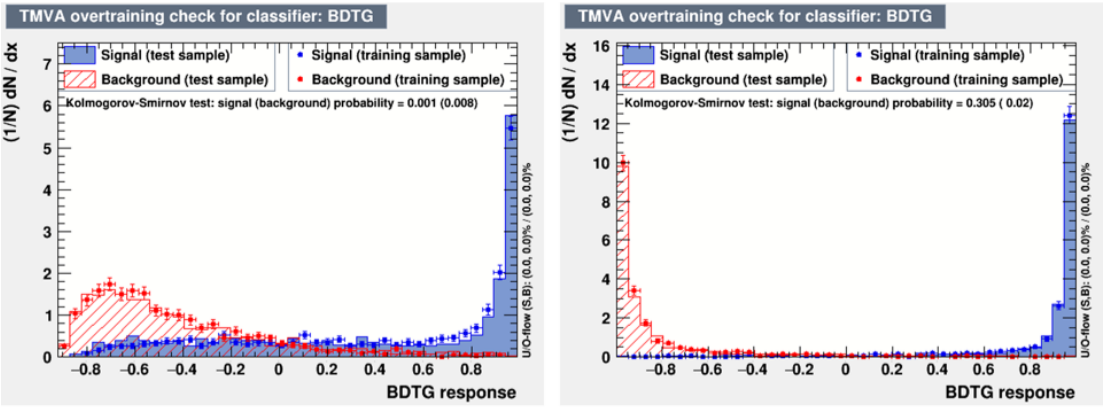

Figure 6.19: The TMVA "over-training" check output for the uranium/lead classifier when applying the BC variables (left) and the HB variables (right). The plots indicate the MVA signal and background output distributions for the training sets in blue and red circles, respectively. Similarly, the MVA output distributions of the testing sets are overlaid with the training sets in blue and red lines for the signal and the background, respectively.

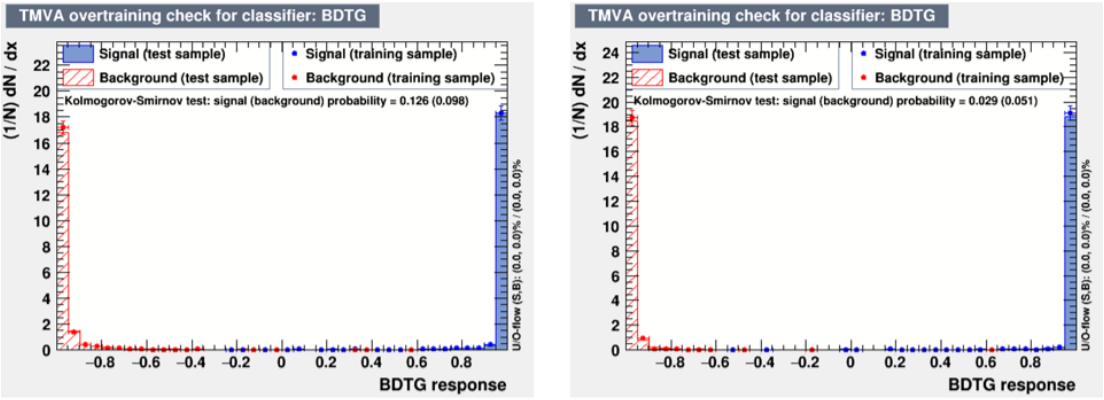

Figure 6.20: The TMVA "over-training" check output for the uranium/lead classifier when applying the ASR variables (left) and the H-ASR variables (right). The plots indicate the MVA signal and background output distributions for the training sets in blue and red circles, respectively. Similarly, the MVA output distributions of the testing sets are overlaid with the training sets in blue and red lines for the signal and the background, respectively.

lead cube. The voxels containing the uranium cube are designated as a signal, and the others containing the lead cube are assigned as background. The classifiers were trained using MST data corresponding to 10 days of muon exposure time reconstructed by the BC, HB, ASR, and H-ASR algorithms. For each reconstruction algorithm, three classifiers were trained using input variables, including the considered approaches

of muon momentum information explained in Section 6.3.2. In terms of materials identification, the performances of the two developed algorithms (the HB and the H-ASR) were compared to the original algorithms in which the HB method was compared to the BC method and the H-ASR method was compared to the ASR method.

The performance of each algorithm was quantified by plotting ROCs and calculating the AUCs when applying the algorithms' input variables when using MC truth momentum, 50% Gaussian smeared momentum, and by removing all the information of the muon momentum (see Figures 6.21, 6.22 and 6.23).

The performance of the HB method showed a significant increase in the AUC values compared to the BC performance, with AUCs, respectively, equalling 99.5 ± 0.2% and 91.9 ± 0.75% when using the MC truth momentum. In the case of the default approach of the 50% smeared momentum, the BC method was slightly affected by the smearing in the momentum information with AUC = 87.2 ± 0.9%, while the HB method maintained its discrimination performance with AUC = 99.0 ± 0.3% showing that the discriminator power of the HB was not significantly affected by the smeared momentum. Furthermore, the HB method also showed good performance in uranium/lead classification even when the muon momentum information was entirely removed with AUC = 90.4 ± 0.85%. Conversely, the ability of the BC method to discriminate the signal from the background was significantly reduced, with AUC = 77.5 ± 1.2%.

It is expected that using the ASR and H-ASR methods showed almost identical discriminator power of the classifier for such a long exposure time (10 days). In the case of using the MC truth momentum, the discriminating power of the classifier was the same, with AUCs = 99.9 ± 0.01% and 99.9 ± 0.004% when using voxels' variables of the ASR and the H-ASR, respectively. It also showed that the classifiers' performance was not affected in the case of using the 50% smeared momentum with AUCs = 99.9 ± 0.05% and 99.9 ± 0.02% for the ASR and the H-ASR voxel variables, respectively.

The AUC of the ROC produced using the H-ASR and the ASR methods showed no effects in the case of removing the momentum information with a value of 99.9 ± 0.02% and 99.9 ± 0.06%, respectively. As shown, a longer exposure time is enough for both algorithms to boost the classifier discriminating power to almost 100%. However, when using the ASR voxel variables with the default scenario of the muon momentum and reducing the exposure time to 12 hours, the classifier's discriminating power decreased to 96.7 ± 0.5%. Conversely, the classifier's discriminating power for the H-ASR method did not reduce as much as in the ASR method, with AUC = 98.0 ± 0.4% (see Figure

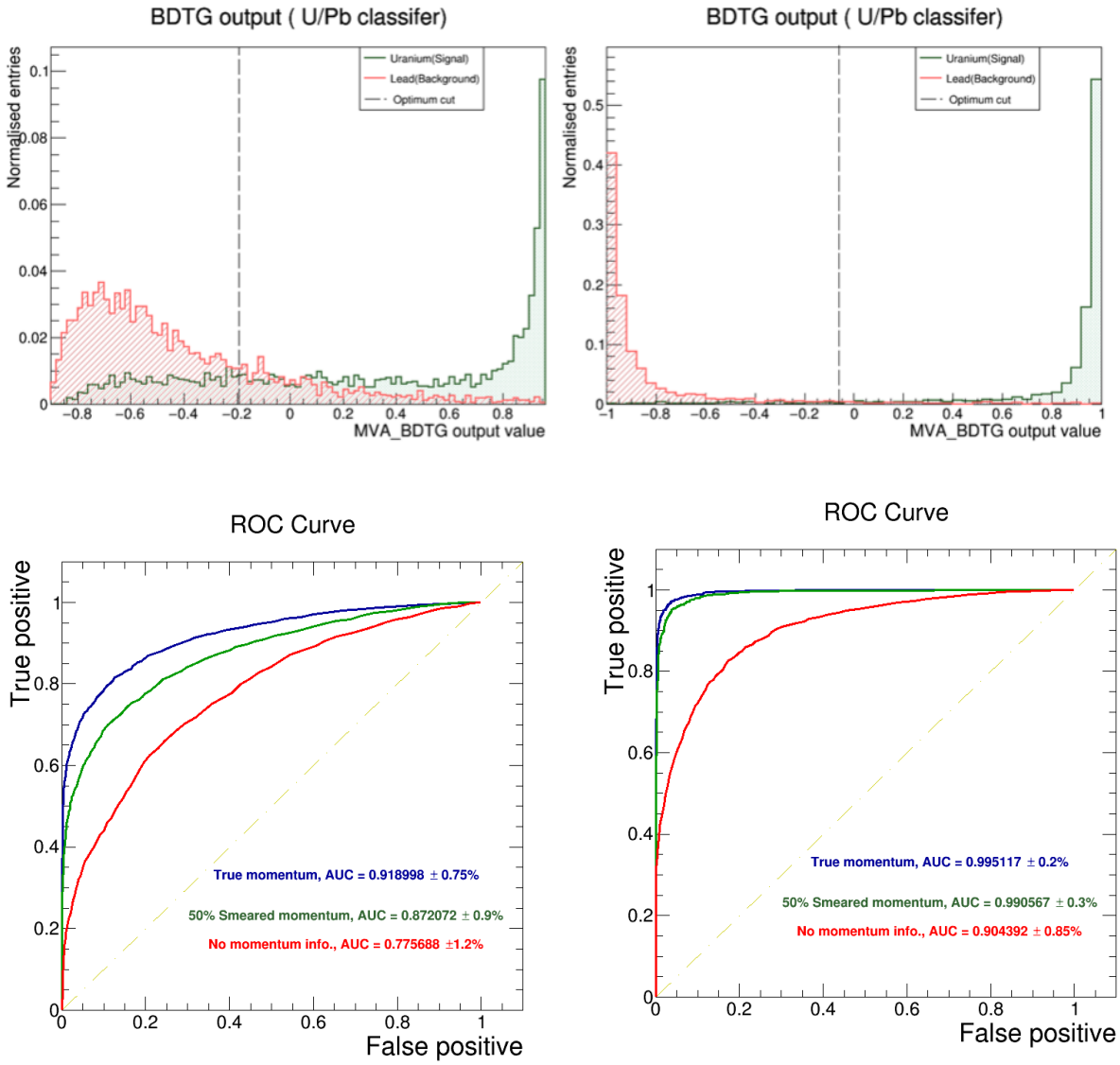

(a)

Figure 6.21: Comparison of the MVA training outputs for the uranium/lead classifier produced using the BC algorithm variables (top left) and the HB algorithm variables (top right). The vertical dashed line represents the optimum cut, which is the point at which signal efficiency and background rejection are equalised, (see section 6.5). The bottom figures show the ROC curves for uranium (signal) vs. lead (background) classifiers using the BC (bottom left) and HB (bottom right) algorithms. The ROC curves and the AUC information are shown for three muon momentum approaches: the MC truth momentum in blue, the 50% Gaussian smeared momentum in green, and when using no momentum information in red.

6.24).

The performance of the MVA classifier showed better discrimination power when trained on the MST muon track data extracted from the HB method compared to the data of the BC algorithm. For this reason, the HB algorithm is applied for materials classification in this chapter. Moreover, in this thesis, algorithms have been developed for using them to identify high-Z materials in such a short exposure time. The MVA classifiers showed that the MST muon track data extracted from the H-ASR algorithm is more powerful, with fewer muons compared to those track data extracted from the ASR method. Hence, the H-ASR muon track data is applied for the MVA classifier hereafter as a second method in addition to the HB algorithm's muon track data.

In terms of muon momentum information, the AUCs of the ROCs created with the three different momentum approaches suggest that the muon momentum information is important in materials classifications. Removing the momentum information significantly reduces the discriminating power, especially when using the muon track data of the BC. In addition, using the HB algorithm data showed a reduction in the discriminating power. However, a 50% smeared momentum scenario indicated that the classifier performance was very close to the performance of the MC truth momentum. For this, the default set-up with smeared momentum is applied in this chapter as the chosen MVA method.

6.7 Results and discussion

As discussed in the previous section, the MVA classifier is able to discriminate a 20-cm uranium cube from a 20 cm lead cube. This section presents the results of the classification of high-Z materials with smaller materials and shorter exposure time. All classifiers will be trained using the simulated MST track data reconstructed by the HB and H-ASR algorithms. These MST data were used in training the MVA classifier explained in Section 6.3. The results of the binary classification method are also discussed.

6.7.1 Binary classification of high-Z Materials

The binary classification method was applied to discriminate between different waste drum contents, including uranium, lead, tungsten, and iridium. All the considered ma-

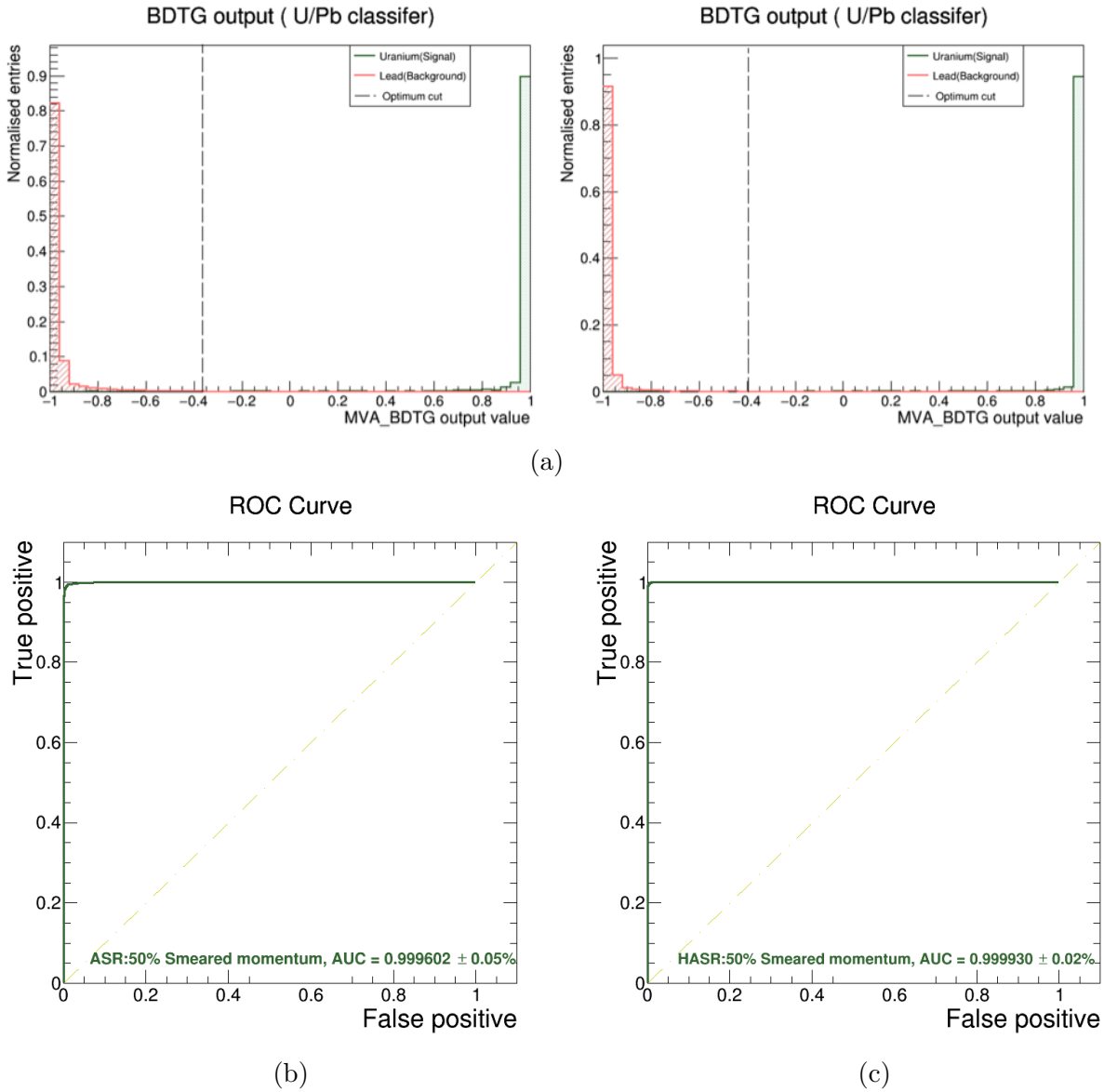

Figure 6.22: Comparison of the MVA training outputs for the uranium/lead classifier produced using the ASR algorithm variables (top left) and the H-ASR algorithm variables (top right). The vertical dashed line represents the optimum cut, which is the point at which signal efficiency and background rejection are equalised, (see section 6.5). The bottom figures show the ROC curves for uranium (signal) vs. lead (background) classifiers using the ASR (bottom left) and H-ASR (bottom right) algorithms. The ROC curves and the AUC information are shown in green for the default muon momentum approach: the 50% Gaussian smeared momentum.

terials were placed in the centre of the waste drum aligned with the drum central axis. This minimises the effects of the positions of the material, where sided objects expect

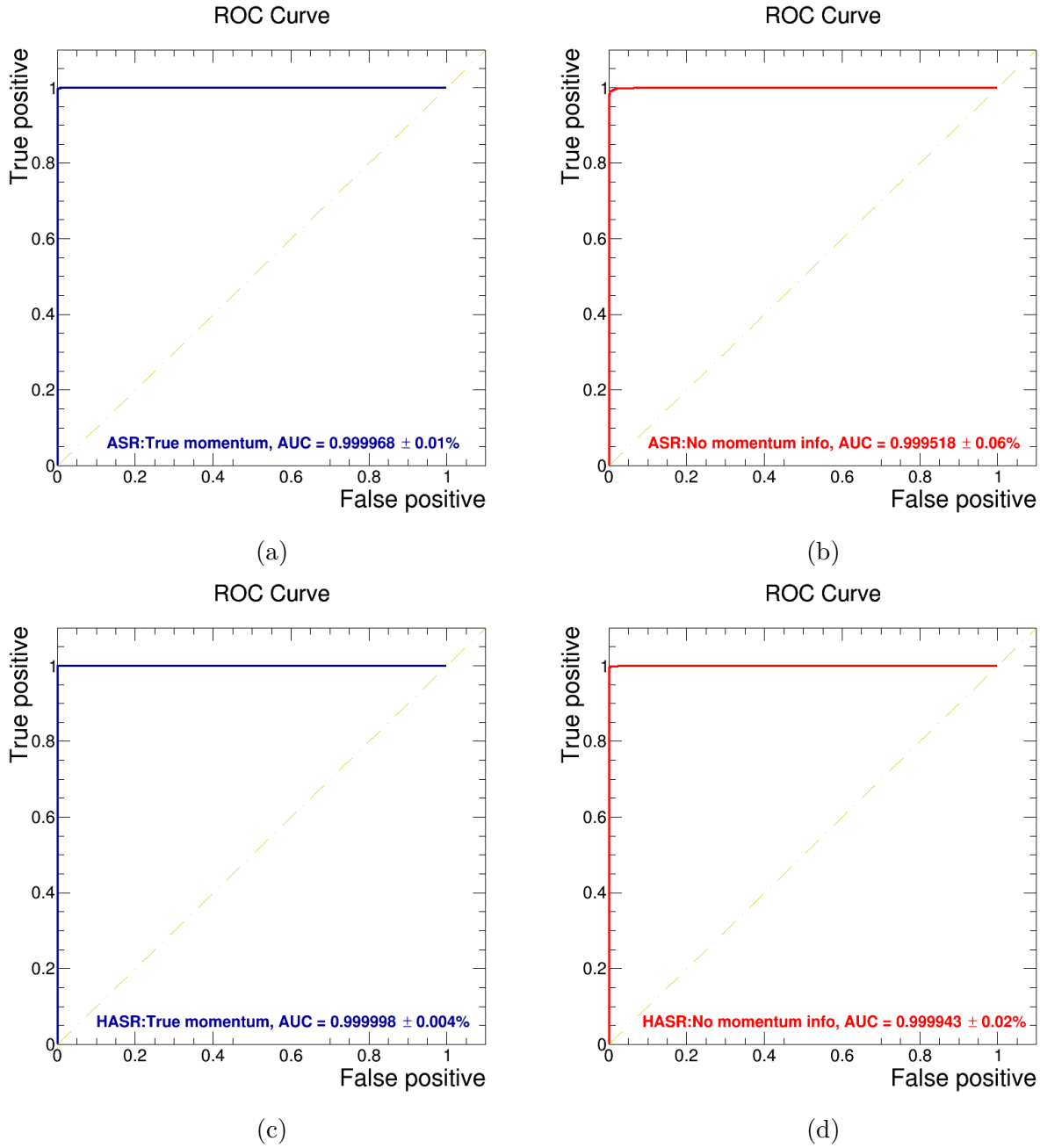

Figure 6.23: The four figures show the ROC curves for uranium (signal) vs. lead (background) classifiers using the ASR (top) and H-ASR (bottom) algorithms. The ROC curves and the AUC information are shown for two muon momentum approaches: the MC truth momentum in blue, and when using no momentum information in red.

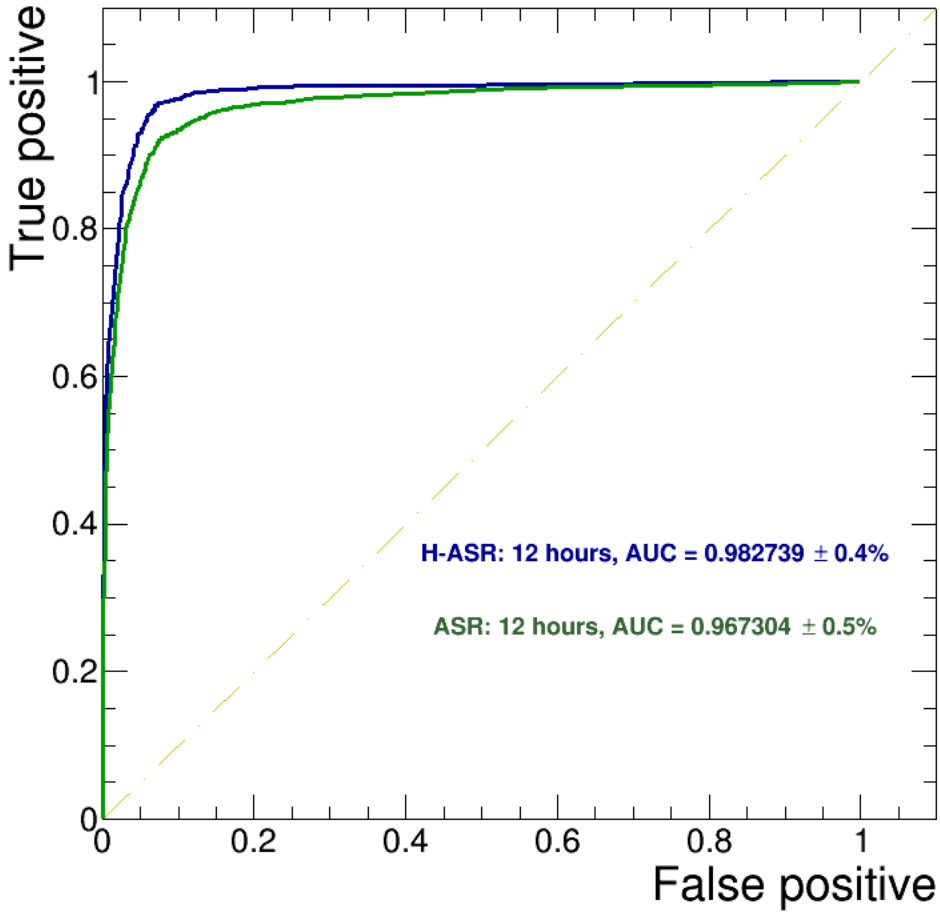

Figure 6.24: Comparison of the ROC curves and the AUC information, respectively, shown in green and blue when using the ASR and the H-ASR for the uranium/lead classifier after 12 hours of muon exposure time.

fewer muons to cross through them. Moreover, this allows for a better understanding of the classification performances of the classifiers.

All the considered materials studied in this section were simulated in a cubic shape with a side length of 5 and 10 cm. Any cubes with a side length of less than 5 cm were not studied due to the fact that the amount of scattering vertices inside these cube sizes was not enough to train the classifier. However, a method used in [76] of adding a few centimetres from the area around the cubes' edge can help gather enough information for the classifiers. In other words, the classifiers can be trained to discriminate between two bigger concrete volumes containing materials with small

cubes. However, this chapter considers only scattering vertices information within the actual cube size.

6.7.1.1 Exposure time dependence

It was already reported in the previous section that almost perfect discrimination between uranium and lead could be obtained for larger cubes. This perfect discrimination was obtained after 10 days of exposure time, with AUCs = 99.9 ± 0.02% and 99.0 ± 0.3% when using the H-ASR and HB algorithms, respectively. This power of discrimination was not degraded when investigating smaller materials in such short times (∽ hours). The AUC for smaller cubes after shorter muon exposure times showed that good discrimination between uranium and cubes could be obtained in a few hours' time (see Figure 6.25 (a)). For example, by using the H-ASR muon track data for discriminating between 10 cm × 10 cm × 10 cm cubes, a good discrimination level can be reached in 3 hours with AUC = 95.0 ± 2.0%.

Moreover, adding one more hour of muon exposure increased the discrimination level to 98.6 ± 1.0%. The discrimination power between uranium and lead reduced slightly after 2 hours of exposure time with AUC = 92.2 ± 2.5%. The AUC values produced for the smaller cubes (5 cm × 5 cm × 5 cm) showed a degree of reduction in the discrimination power between uranium and lead, with AUCs = 94.6 ± 6.5% and 93.6 ± 7.1%, respectively, after 4 and 3 hours of muon exposure time. AUC obtained for

Cube Size	**10** *cm* × **10** *cm* × **10** *cm*		**5** *cm* × **5** *cm* × **5** *cm*	
Classifiers / **Time (h)**	**U/Pb**	**U/W**	**U/Pb**	**U/W**
2	**92.2 ± 2.5**	**81.5 ± 3.7**	**87.0 ± 10.1**	**73.8 ±13.8**
3	**95.0 ± 2.0**	**91.3 ±2.6**	**93.6 ± 7.1**	**88.2 ±9.7**
4	**98.6 ± 1.0**	**97.0 ± 1.5**	**94.6 ± 6.5**	**91.9 ± 8.0**
Time to reach ≥ 95 %	**3 hours**	**4 hours**	**4.5 hours**	**6 hours**

Table 6.2: AUCs of different ROC curves (see Figure 6.25) obtained by the MVA classifier using the H-ASR algorithm variables to discriminate between uranium against lead and uranium against tungsten. The results showed different volumes of the comparable cubes and several short exposure times (hours). The last row shows times to reach good discrimination (AUC = 95.0%) between the comparable materials.

classifying 10 cm-side-length uranium against tungsten was slightly lower, with values of 97.0 ± 1.5% and 91.3 ± 2.6%, respectively, after 4 and 3 hours of muon exposure time. This is expected because of the high similarities in densities of tungsten and uranium with a difference of $\Delta\ \rho = 0.95$, while $\Delta\ \rho$ between uranium and lead is equal to 7.6. According to the results of the uranium/tungsten classifier, it is noticeable that the AUC values increased with more hours of taking data time. The discrimination power of the uranium/tungsten classifier improves, with AUC values climbing from 81.5 ± 3.7% to 97.0 ± 1.5% after 2 and 4 hours of muon taking data time (see Figure 6.25 (b)). There was also significant improvement in the performances in distinguishing between the smaller cubes with AUC values increasing from 73.8 ± 13.8% to 91.9 ± 8.0%, respectively, after 2 and 4 hours of muon exposure time. A summary of the AUC values for the classification of uranium/lead and uranium/tungsten for different sizes and muon exposure times is shown in Table 6.2.

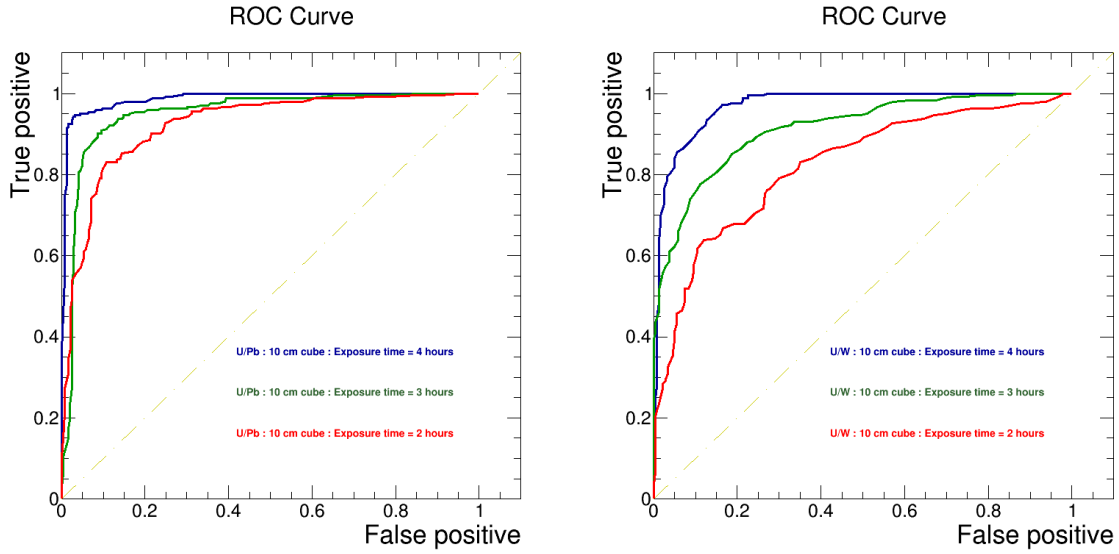

(a) (b)

Figure 6.25: ROC plots of the true positive rate as a function of the false positive rate for 10 cm × 10 cm × 10 cm uranium/lead binary classifier in (a) using the H-ASR variables. ROC plots shown in (b) are for 10 cm × 10 cm × 10 cm uranium/tungsten binary classifier using the H-ASR variables. All ROC curves are shown in red, green, and blue after 2, 3, and 4 hours of muon exposure times, respectively.

It is expected that the classification of materials using the HB algorithm variables needs longer muon exposure time. This is because the HB is based on calculating the metric distances between each pair of scattering vertices in each voxel containing the compared materials. As expected, voxels containing high-Z or dense materials will have a higher density of high scattering vertices. This makes it challenging for

the MVA classifiers to discriminate between two or more materials with similarities in their properties in such a short time. The results of applying the voxel variables obtained by the HB method to the MVA binary classifier showed that a longer time (16 hours) is needed to discriminate between 10 cm side length uranium against lead with AUC = 95.6 ± 1.8%. The improvements in classifier capability grow slowly with increasing muon exposure time. For example, the AUCs obtained from ROC curves after 6 hours of taking MST data were equal to 87.1 ± 3.2%, and it took 12 hours to reach a value of 92.7 ± 2.4% (above 90%). For smaller cubes with a side length of 5 cm, the classifier needs 24 hours of muon exposure time to discriminate between uranium and lead with AUC =96.0 ± 5.6%.

As already mentioned regarding the challenge of classification between uranium and tungsten, the results showed that the classifier needs 20 hours to separate 10-cm-side-length uranium from tungsten with AUC = 96.1 ± 1.7%. A summary of the AUC values for the classification of uranium/lead and uranium/tungsten for 10-cm-side-length cubes and several muon exposure times is shown in Table 6.3. The discrimination power was also affected when the cube material was reduced to 5 cm in the uranium/tungsten classifier case. The AUCs yielded when discriminating smaller uranium and tungsten cubes were equal to 82.1 ± 11.8%, 82.8 ± 11.6%, 83.6 ± 11.3%, 88.1 ± 9.7%, and 93.7 ± 7.0% after 12, 16, 20, 24, and 26 hours of muon exposure time.

Cube Size	**10** cm × **10** cm × **10** cm	
Classifiers / **Time (h)**	**U/Pb**	**U/W**
6	**87.1 ± 3.2**	**77.4 ± 4.1**
8	**87.8 ± 3.1**	**81.1 ±3.8**
12	**92.7 ± 2.4**	**88.8 ± 3.0**
16	**95.6 ± 1.8**	**91.7 ± 2.5**
Time to reach ≥ 95 %	**16 hours**	**20 hours**

Table 6.3: AUCs of different ROC curves (see Figure 6.26) obtained by the MVA classifier using the HB algorithm variables to discriminate between uranium against lead and uranium against tungsten. The results showed for the 10 cm× 10 cm × 10 cm cubes and also for several exposure times (hours). The last row shows the times to reach good discrimination (AUC = 95.0%) between the comparable materials.

Even though the $\Delta\rho$ factor has affected the discrimination performance of the classifier, it is also worth mentioning that the number of muons crossing the smaller cubes also played a big role in reducing the discrimination power. This is reasonable as the classifier only considers the muons that crossed through the target materials. This can be seen when comparing the AUC results of the 10 cm side length cube with a volume of 1000 cm^3 to the 5 cm side length cubes with a volume of 125 cm^3. For example, the classifier performance was reduced by approximately 9.5% when using the H-ASR voxel variables to classify 125 cm^3 uranium from tungsten in 2 hours of muon exposure time compared to the performance when the cubes' volume was 1000 cm^3. However, the percentage of reduction in performance was lower ($\backsim$ 5%) when the exposure time increased to 4 hours.

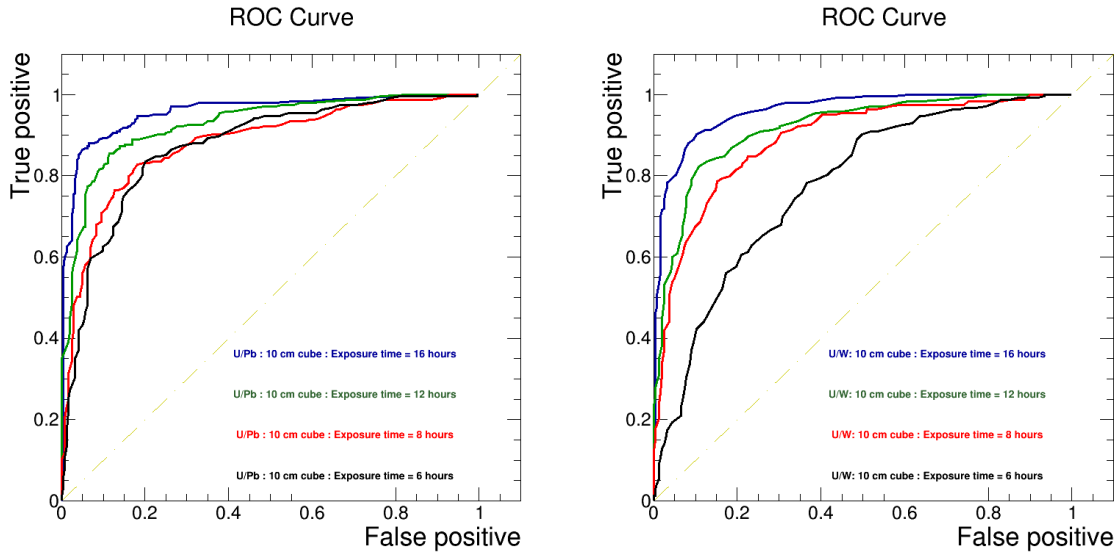

(a) (b)

Figure 6.26: ROCc plots of the true positive rate as a function of the false positive rate for 10 cm × 10 cm × 10 cm uranium/lead binary classifier in (a) using the HB variables. ROCc plots shown in (b) are for 10 cm × 10 cm × 10 cm uranium/tungsten binary classifier using the HB variables. All ROC curves are shown in black, red, green, and blue after 6, 8, 12, and 16 hours of muon exposure time, respectively.

6.7.1.2 Atomic number dependencies

As seen in the previous section, good discrimination power was achieved between materials with $\Delta\ Z = 10.0$ and 18.0 for uranium/lead and uranium/tungsten, respectively. Even though the $\Delta\ Z$ between uranium and tungsten is larger, the similarities in their

densities make the discrimination between those materials more challenging than the discrimination between uranium and lead. Furthermore, MVA classifiers are trained to test the ability of the H-ASR and HB methods to distinguish between materials with lower $\Delta\ Z$ factor. Examples of several ROCs for materials with $\Delta\ Z$ equal to 3, 5, and 8, respectively, for iridium/tungsten, lead/iridium, and lead/tungsten binary classifiers are shown in Figure 6.27. A summary of the AUC values in Figure 6.27 obtained after 6 hours of muon exposure time is shown in Table 6.3.

Cube Size	**10** cm **×** **10** cm **×** **10** cm		
Classifiers / **Algorithm**	**Pb/Ir**	**Pb/W**	**Ir/W**
HASR	**95.6 ± 1.8**	**95.3 ± 1.9**	**94.6 ± 2.0**
HB	**88.9 ± 2.9**	**87.9 ±3.1**	**85.7 ± 3.3**
$\Delta\ Z$	**5**	**8**	**3**
$\Delta\ \rho$	**11.07**	**7.95**	**3.12**

Table 6.4: AUCs of different ROC curves (see Figure 6.27) obtained by the MVA classifier using the H-ASR and HB algorithm variables to discriminate between lead against iridium, lead against tungsten, and iridium against tungsten. The results showed for the 10 cm × 10 cm × 10 cm cubes and for 6 hours of muon exposure time. The characteristics of the considered materials are also shown.

The $\Delta\ Z$ factor is important in materials classification, especially when using the H-ASR voxel variables for the classifiers. For example, the AUC value produced for the lead/tungsten classifier is equal to 95.3 ± 1.9%, which is slightly lower than the AUC value when classifying materials with $\Delta Z \geq 10.0$ (uranium/lead and uranium/tungsten). The classifier needs only 4 hours to reach ≥ 97.0 to discriminate between materials with $\Delta Z \geq 10.0$ (see Table 6.2). However, discriminating between lead/tungsten took 6 hours of muon exposure time to reach the discrimination level of 95%. Moreover, the classification result between iridium and tungsten also showed a small reduction in the discriminating power of the classifier, with AUC = 94.6 ± 2.0%. The iridium/tungsten classifier is the most challenging among the other classifiers, as the characteristics of the materials have similarities with $\Delta Z = 3$ and $\Delta\ \rho = 3.12$.

The case of using the HB variables is different as the classification of the materials most likely depends on the density of the target materials. This can be seen in the results of the uranium/tungsten classifier vs. the iridium/tungsten classifier. The difference in the Z number between uranium and tungsten is large (ΔZ= 18); however,

the AUC value of distinguishing uranium from lead in 6 hours of time is equal to 77.4 ± 4.1%. Once the $\Delta\rho$ factor increases between the comparable materials, the discrimination power improves gradually. For example, the ability of the classifier using the HB variables increased to 85.7 ± 3.3%, 87.9 ± 3.1%, and 88.9 ± 2.9% when the gaps between the densities grew to 3.12, 7.95, and 11.07, respectively.

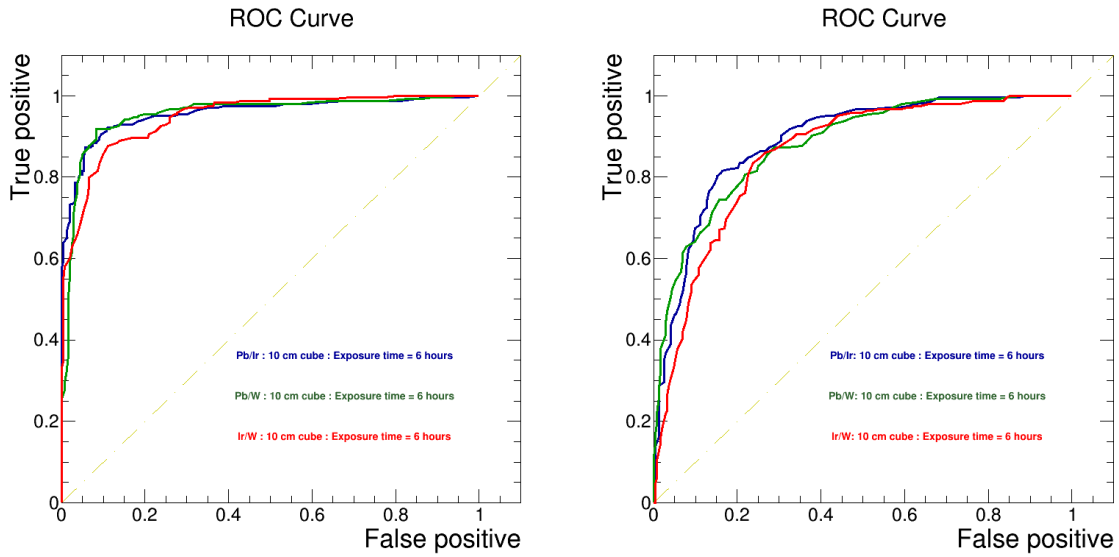

(a) (b)

Figure 6.27: ROCc plots of the true positive rate as a function of the false positive rate for 10 cm × 10 cm × 10 cm lead/iridium, lead/tungsten, and iridium/tungsten binary classifiers in (a) using the H-ASR variables after 6 hours of muon exposure time. ROCc plots shown in (b) are for the same classifiers using the H-ASR variables after 4 hours of exposure time. All ROCc plots shown are plotted after 6 hours of exposure time.

6.7.2 Non-binary classification of high-Z materials

The ability of the developed algorithms to discriminate (binary-classifiers) between different high-Z materials stored globally in the different waste drums was shown in the previous section. Here, a non-binary classifier refers to a classifier trained on two or more classes, where it differentiates one signal from two or more background classes. Further MVA classifiers were performed to discriminate between waste high-Z materials stored in the same drum. As both algorithms are able to localise the materials inside the drum with good resolution in a few hours, classification of materials locally is applicable. The material cube each had a side length of 10 cm and was aligned

with the central (cylindrical) axis of the drum (see Figure 6.28). Two MVA non-binary classifiers were trained using the H-ASR variables and the HB variables that distinguished uranium signals from tungsten and lead backgrounds.

It is important to mention that the non-binary classifier might need a longer exposure time compared to the binary classification discussed in the previous section. This is caused by the fact that the materials positioned on the side area of the drum expect fewer muons compared to the materials in the centre of the drum.

Figures 6.29 and 6.30 indicate the MVA non-binary classifiers responses when using H-ASR and HB variables, respectively. The classifier response outputs were used to plot ROC curves and then calculate the AUCs to evaluate the ability of each method to discriminate uranium from background cubes. The AUCs of the training ROC showed that uranium is easily discriminated from the lead cube in 12 hours of muon exposure time with AUC = 96.5 ± 1.6% when applying the H-ASR voxel variable information. The training ROC when using the HB variables produces an AUC value of 90.6 ± 4.0% in 12 hours, which is below the selected good discriminating level. However, with a longer exposure time (48 and 96 hours), the discrimination power of the non-binary uranium/lead classifier performs nearly perfectly, with AUC = 99.0 ± 0.85% and 99.5 ± 0.5%, respectively, (see Figure 6.31). This is probably due to the method

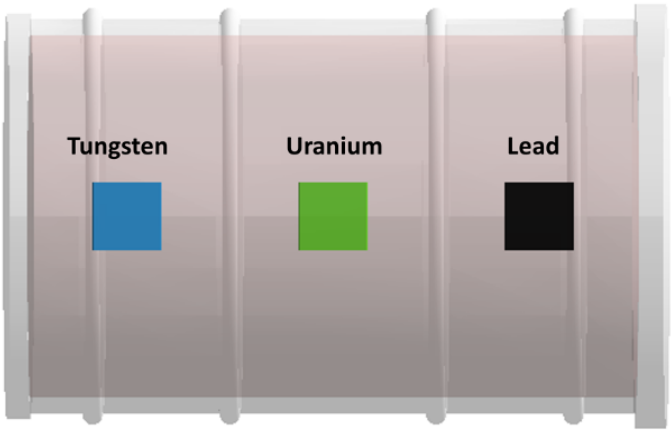

Figure 6.28: Illustrative of the simulated cubic materials inside the steel drum; each cube has a side length of 10 cm. The centre-to-centre distance between the signal cubes (uranium) to the background cubes (lead and tungsten) was set to 30 cm.

of the HB algorithm to calculate the scattering vertices in each voxel, in which the more muons cross the materials, the higher scattering density inside the highly dense materials would occur. The results of AUCs produced using the H-ASR variables suggest that the H-ASR method is faster to reach good discrimination in a short

exposure time (see Figure 6.31).

The training ROC plots for the uranium/tungsten non-binary classifier indicate that the H-ASR method is able to separate uranium from tungsten in 12 hours with AUC = 95.8 ± 1.8%. However, the HB method does not perform well in such a short muon exposure time with AUC = 78.5 ± 4.0%. The performance of the classifier is expected to be under a good separation level due to the high similarity of the materials densities. Moreover, the position of comparable materials might contribute to reducing the non-binary classifier. This is reasonable as the target materials placed in the centre of the drum would expect more muons to cross through it due to the angular acceptance of the detector.

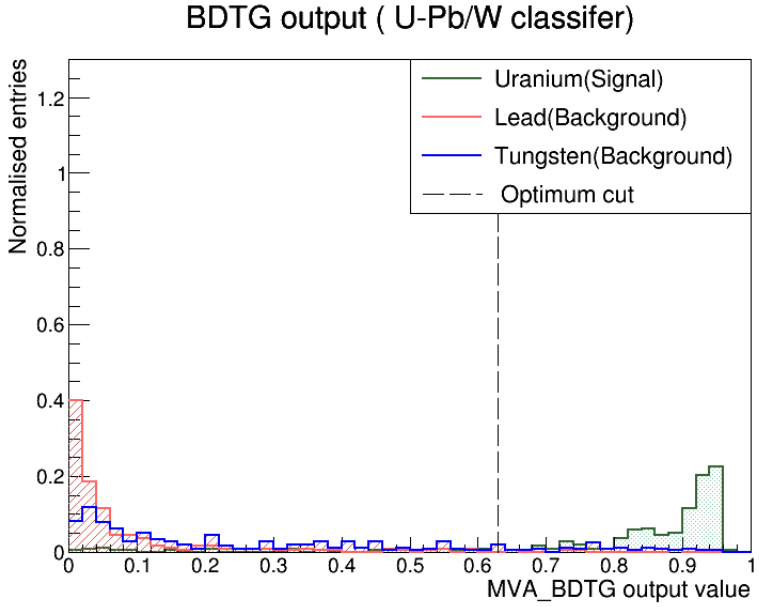

Figure 6.29: Comparison of the MVA training outputs for uranium–lead/tungsten non-binary classifier produced using the H-ASR algorithm variables. The vertical dashed line represents the optimum cut, which is the point at which signal efficiency and background rejection are equalised. The green line represents the uranium signal distribution output, while the red and blue lines represent the background, which are lead and tungsten, respectively.

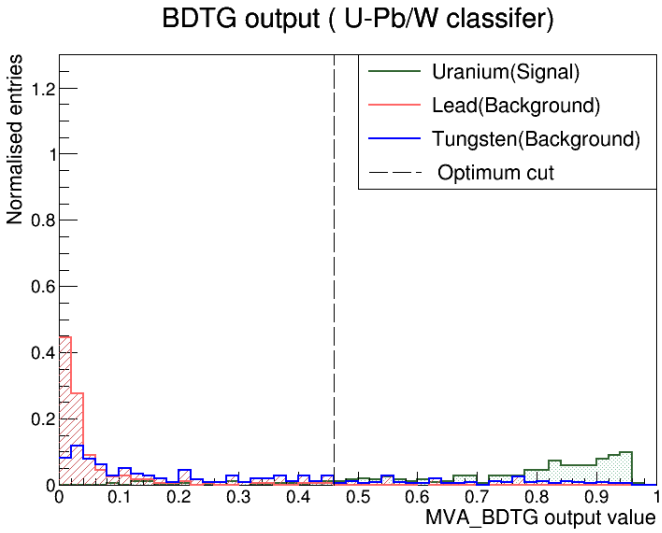

Figure 6.30: Comparison of the MVA training outputs for uranium–lead/tungsten non-binary classifier produced using the HB algorithm variables. The vertical dashed line represents the optimum cut, which is the point at which signal efficiency and background rejection are equalised. The green line represents the uranium signal distribution output, while the red and blue lines represent the background, which are lead and tungsten, respectively.

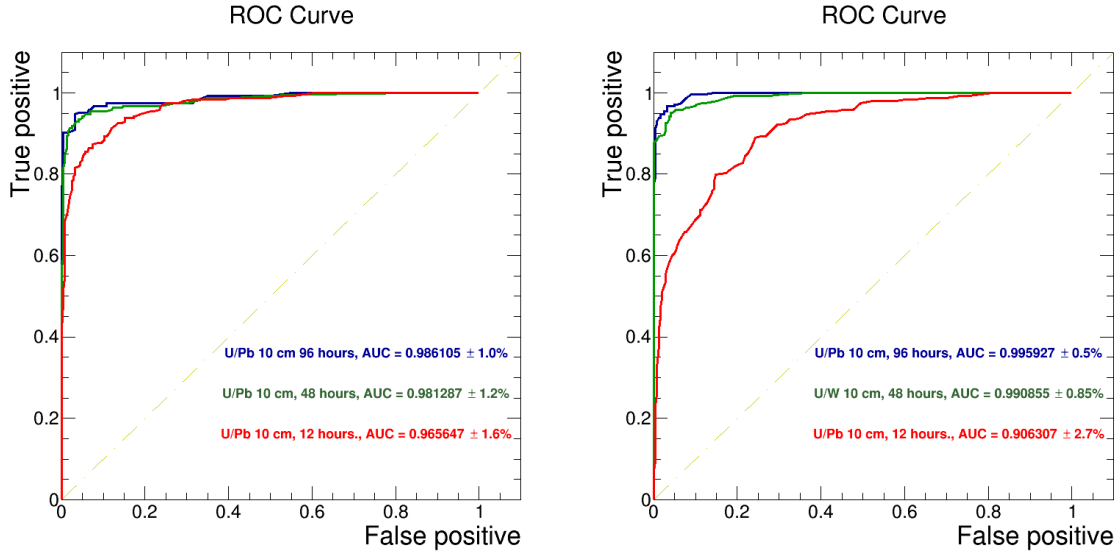

(a) (b)

Figure 6.31: ROCc plots of the true positive rate as a function of the false positive rate for 10 cm × 10 cm × 10 cm uranium/lead non-binary classifier in (a) using the H-ASR variables after several muon exposure times. The ROCc plots shown in (b) are for the same classifiers using the HB variables after several exposure times. The AUC value information is stated in blue, green, and red for the uranium/lead classifier after 96, 48, and 12 hours of muon exposure time.

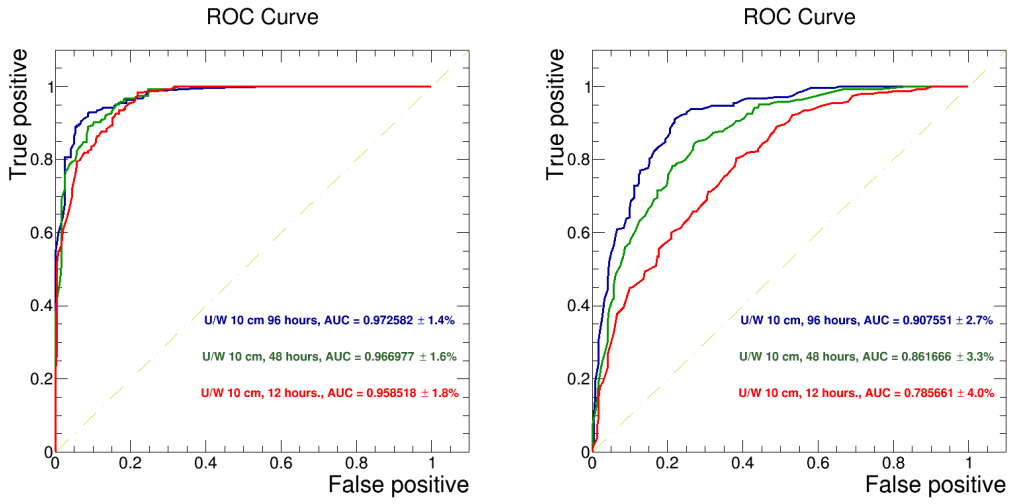

(a) (b)

Figure 6.32: : ROCc plots of the true positive rate as a function of the false positive rate for 10 cm × 10 cm × 10 cm uranium/tungsten non-binary classifier in (a) using the H-ASR variables after several muon exposure times. The ROCc plots shown in (b) are for the same classifiers using the HB variables after several exposure times. The AUC value information is stated in blue, green, and red for the uranium/lead classifier after 96, 48, and 12 hours of muon exposure time.

6.8 Conclusion

This chapter presented two new algorithms that were built and developed to avoid the previous limitations of the reconstruction algorithm in the materials' classification field. The first algorithm is the HB built to avoid the BC algorithm limitation, and the second algorithm is the H-ASR, which is built to optimise the original ASR algorithm. It also demonstrated that combining the TMVA tool and the MST technique is effective in investigating nuclear waste contents. It was shown in this chapter that the HB algorithm significantly boosted the materials classification power of MST compared to the default BC algorithm. This is seen in applying the MVA binary classifier to discriminate between 20-cm-side-length uranium from an equally sized lead cube. The minimum AUCs of the ROCcs were assigned as 95% to discriminate between two or more materials.

The training ROC curves showed results of AUCs with values of 99.0 ± 0.3% and AUC = 90.0 ± 0.85% when using the HB variable data with 50% Gaussian smeared muon momentum and without momentum information, respectively. The results when

using the BC variables data of 10 days equivalent exposure time showed inability of the BC algorithm to discriminate between uranium and lead with AUCs = 87.2 ± 0.9%, and 77.5 ± 1.2%, in the case of using 50% smeared momentum and without momentum information, respectively. Moreover, the classification power of the classifier when trained on the BC variables failed to reach the minimum discrimination level, even when using the MC truth momentum, with AUC = 91.8 ± 0.75%.

In terms of muon momentum information, the results reported in this chapter showed that momentum information is not necessary to achieve the minimum discrimination level using the H-ASR algorithm in materials classification. The MVA binary classifier trained on the H-ASR variables after 10 days of equivalent exposure time showed almost perfect discrimination power when using MC truth momentum, with AUC = 99.9 ± 0.01%. Moreover, when removing all the momentum information, the AUC results were still above the good discrimination level with a value of 99.9 ± 0.06%. After a short exposure time, the 20-cm uranium/lead binary classifier was enhanced when using 12 hours of the H-ASR variables to train the classifier, with AUC = 98.2 ± 0.4%. The classifier performance was compared when the ASR variables were used to train the classifier with AUC = 96.7 ± 0.5%.

The H-ASR algorithm is seen to be feasible for discriminating between high-Z materials in a few hours of muon exposure time. The ability of the MVA classifier trained on the H-ASR variables to discriminate between materials with high similarities in their properties was tested for a short exposure time. For cubic materials with a dimension of 10 cm × 10 cm × 10 cm, the muon detector system used in this thesis needs 3 hours for the U/Pb binary classifier using the H-ASR variables. Moreover, classification between high-Z materials with almost similar density (U/W) needs only 4 hours of muon exposure time to go beyond the good discrimination level with AUC = 97.0 ± 1.5%, using the H-ASR method variables.

The MVA classifier trained on variables extracted from the HB algorithm is more sensitive to the materials' densities. The AUCs produced by the U/Pb binary classifier achieved a good discrimination level in 16 hours of muon exposure time.

The classifiers are also used to train the HB and H-ASR variables to discriminate materials stored inside the same waste drum. The H-ASR algorithm requires only 12 hours of muon exposure time to separate uranium from other background materials, such as lead and tungsten. The MVA non-binary classifier trained using the H-ASR variables can distinguish uranium from lead and tungsten with AUCs of 96.5 ± 1.6%., and 95.8 ± 1.8%.

Chapter 7

Conclusion

The characterisation of nuclear waste materials needs to be addressed to make them safe for disposal or long-term storage. Before waste materials can be sent to disposal/storage facilities, their classification must be considered, including whether they are high-level waste (HLW), intermediate-level waste (ILW), or low-level waste (LLW). Information about the contents of old radioactive waste packages or packages with heterogeneous conditioned radioactive content must also be collected. Several destructive /non-destructive technologies can be used to classify nuclear waste materials. This thesis proposed muon scattering tomography technology (MST) as a non-destructive imaging method to image or classify well-shielded nuclear waste in two types of nuclear waste packages, namely, small steel drums and V/52 CASTOR casks.

In recent years, MST technology has been sufficiently used as a viable method for investigating well-shielded materials. This thesis has covered a wide range of reconstruction algorithm methods connected by the general motivation to use the MST technique for imaging, scanning, and classifying nuclear waste materials. The MST technique exploits the fact that cosmic muons can traverse through large or dense objects. As cosmic muons travel through objects, they undergo multiple Coulomb scattering (MCS). Scattering angle values vary depending on the objects that the muons crossed through (e.g., larger scattering angles are expected when muons cross dense or high-Z materials). The distributions of the scattering angles are used to image/classify hidden bodies of waste materials.

Chapter 5 described the most common previously developed reconstruction algorithms used in MST, namely, the Binned Clustering (BC) [69], Point of Closest Approach (PoCA) [73], and Angle Statistics Reconstruction (ASR) algorithms [74]. These

algorithms were quantitatively evaluated in terms of each method's abilities to differentiate between specific regions within the volume of interest. To differentiate between regions inside a 3D image output of each method, these algorithms were tested using simulated MST data cross through high-Z, medium-Z, and low-Z materials encased in a concrete-matrix small drum and in a large V/52 cask.

A new method for dividing the volume of interest into a rectangular-shaped voxel was introduced in chapter 5, and this new method was applied to optimise the performances of all algorithms regarding the imaging of well-shielded materials. It was documented that statistical errors in the voxels were reduced by increasing the voxel height from 10 mm to 30 mm. For example, a contrast to noise ratio (CNR) value produced by the BC method to distinguish between the 10 cm side length cubes of uranium and lead encased in concrete matrix increased from 0.8 ± 0.1 to 1.4 ± 0.05. This was improved by 75% when applying the new method of changing the shape of the voxels. When discriminating between uranium and lead, the ASR algorithm's performance is also improved when considering the new voxel shape, with a 45% increase in the CNR values, from 2.2 ± 0.07 to 3.2 ± 0.1.

After optimising the old algorithms performances in imaging hidden objects using the MST technique, further developments were made to maximise some of the reconstruction algorithms performance abilities regarding the use of various nuclear waste imaging methods. A new reconstruction algorithm method was developed to combine the strong proprieties of the BC and ASR algorithms, and was denoted as the hybrid algorithm (HB). Another version of the ASR algorithm was also developed based on the ASR method and was denoted as the H-ASR algorithm.

In chapter 6, the new algorithms were applied in the classification of high-Z materials with varying sizes. Because some high-Z materials have similarities in their atomic and nuclear properties, it was shown that when using previous methods, such as the BC algorithm, it might be impossible to discriminate between high-Z materials in a short time. This was demonstrated by the performance of a 20 cm uranium/lead binary classifier trained on the BC variables, which resulted in AUC = 90.6 ± 0.8% after 10 days of muon exposure time. Training the classifier on the HB variables for the same exposure time produced AUC = 99.2 ± 0.2%. Good discrimination levels were achieved in 16 and 20 hours while using materials with $\Delta\ \rho = 7.6$ (U/Pb) and 0.95 (U/W), respectively for 10 cm × 10 cm × 10 cm cubes. The classifier performed better when using the H-ASR variables, reaching a good separation level in 4.5 and 6 hours while distinguishing a 5 cm side length with U/Pb and U/W binary classifiers, respectively. The non-binary classifiers needed a longer exposure time, reaching a good separation level in 12 hours for both U/Pb and U/W, when using the H-ASR variables.

Thesis findings

The results documented in this thesis demonstrated that it is possible to image and discriminate between high-Z materials using the MST technique in a few hours. The procedure starts by localising the materials with a good quality of the reconstructed image of the high-Z and medium-Z. materials. Once the material positions are known, they can be discriminated from one another in a few hours using combinations of multivariate analysis (MVA) that include information on the HB and H-ASR variables.

The results also showed that the geometrical shape of the voxel enhances the algorithm's performance in general. It also showed that limitations inherited from the "single-scattering" assumption were prevented using the HB and H-ASR methods in the classification of high-Z materials. For example, in [77], discrimination between 20 cm side-length uranium and lead produced an AUC of 81.1 (the statistical error was not provided) when 10 days' worth of equivalent data from the BC algorithm was used inside a cubic voxel with 10 mm side lengths. However, using methods that remove the single-scattering assumption improves the classifier's classification power to a discrimination level $\geq 95\%$ with AUCs $= 95.6 \pm 1.8\%$ and $95.0 \pm 2.0\%$ in 16 hours and 3 hours using the HB and the H-ASR variables, respectively.

Future work

Future work is required to continue investigating the classification of high-Z materials without any previous knowledge of the location of the these objects inside drums. This can be done by first filtering out the shielding matrix, as most drum dimensions are well-known, and then by applying machine learning, such as k-mean clustering algorithms, to identify non-filtered voxels that contain high-Z or dense materials. Furthermore, as disposed materials do not necessarily have a cubic shape or a regular shape, more work needs to be performed to test the MST method for identifying materials with different shapes. In summary, this thesis has documented good results while using MST technology for the classification of nuclear waste materials. As the results were obtained using simulated data, the next step will be to apply the methods used in this thesis experimentally. Finally, it is recommended that work in the field of imaging and classifying nuclear waste materials using MST continue, especially with a focus on the highlighted research points mentioned in this section.

Appendix A: The MVA classification Methods

Here, the hyper-parameters sets for the MVA methods used for materials classification in chapter 6.

Boosted Decision Trees (BDT)

- Maximum tree depth: 3
- Smallest fraction of training events in a leaf node: 5%.
- Gradient boosting learning rate: 0.01
- Grid points utilized for optimal variable division: 20.

Gradient-Boosted Decision Tree (BDTG)

- Maximum tree depth: 3
- Smallest fraction of training events in a leaf node: 5%.
- Gradient boosting learning rate: 0.01
- Grid points utilized for optimal variable division: 20.

Appendix B: Additional Figures for Materials Identification

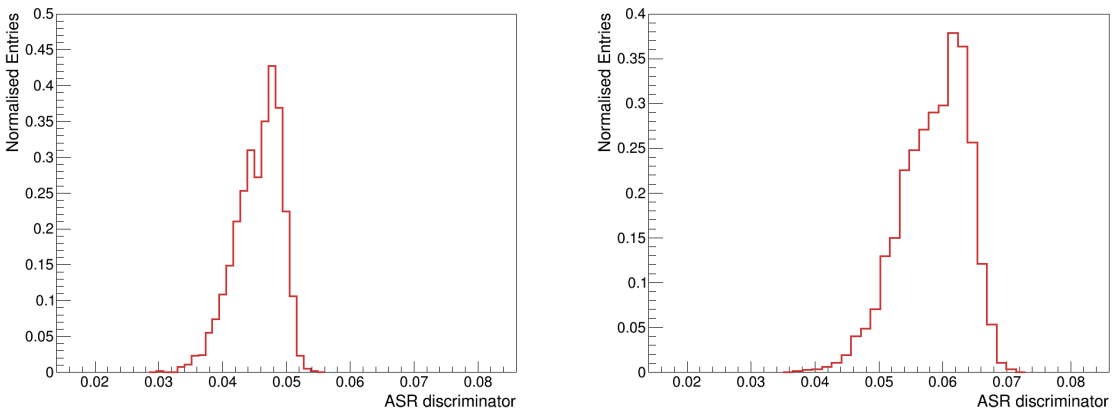

(a) (b)

Figure 7.1: Comparison of distributions of the ASR discriminator for a voxel containing uranium (left) and lead (right). The normalised bin counts of these distributions are calculated and passed to the MVA classifiers.

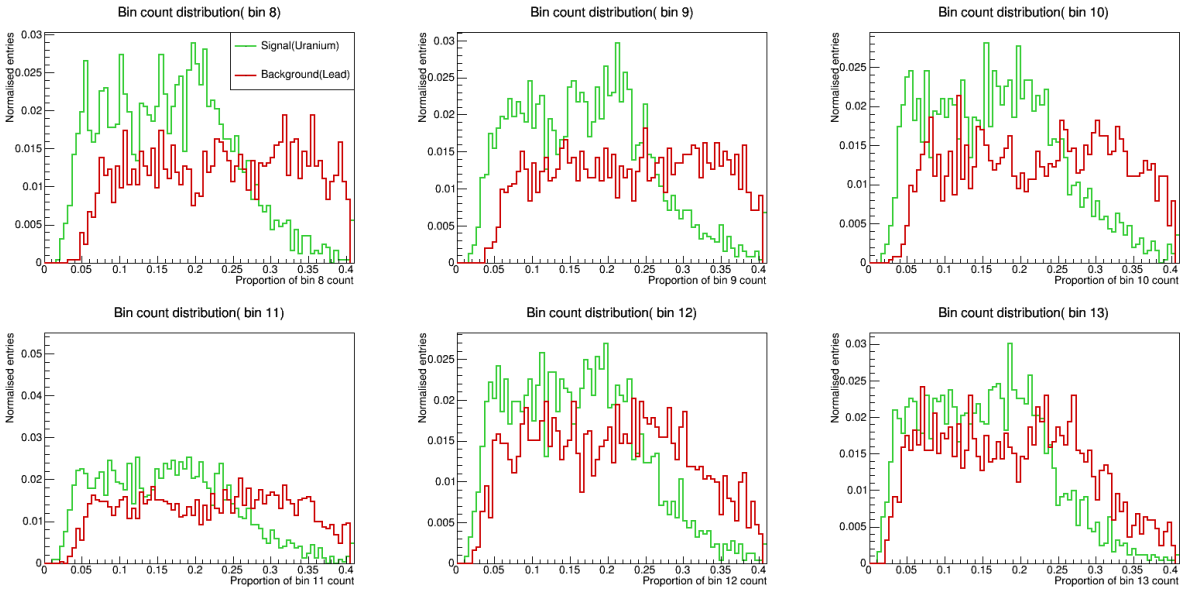

Figure 7.2: Comparison of some bin count distributions of the ASR method used as input variables to train the MVA classifiers. These distributions were extracted from the normalised bin counts. The green line represents voxels containing a 20 cm uranium cube (set as a signal), and the red line represents voxels containing an equally sized lead cube (set as a background).

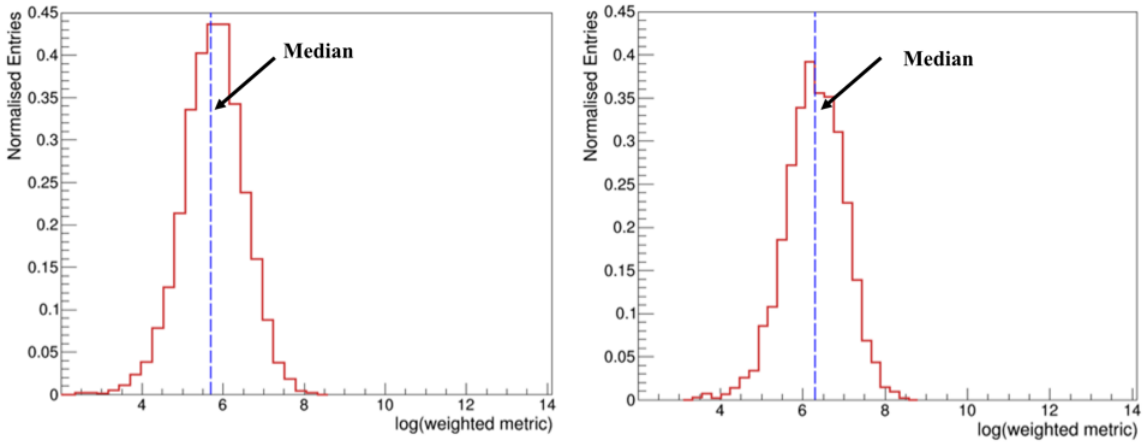

Figure 7.3: Comparison of distributions of the $log(\widetilde{m_{ij}})$ produced by the BC method for a voxel containing uranium (left) and lead (right). The blue-dashed line represents the median of the distributions, which is set as the discriminator value in the BC algorithm output image.

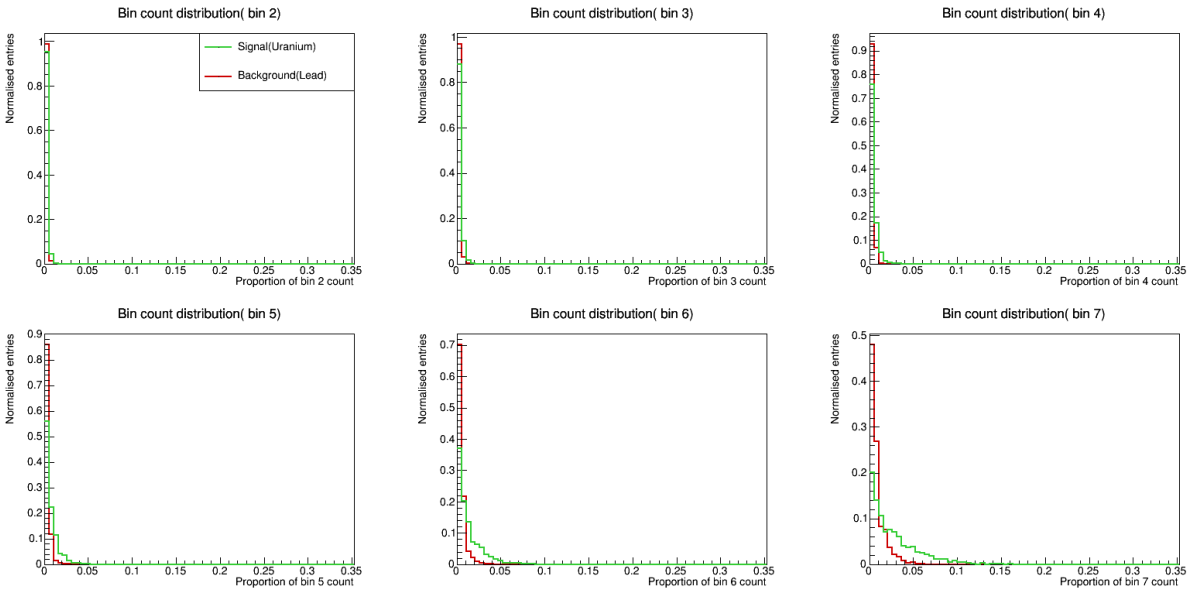

Figure 7.4: Comparison of some bin count distributions of the BC method used as input variables to train the MVA classifiers. The green line represents voxels containing a 20 cm uranium cube (set as a signal), and the red line represents voxels containing an equally sized lead cube (set as a background).

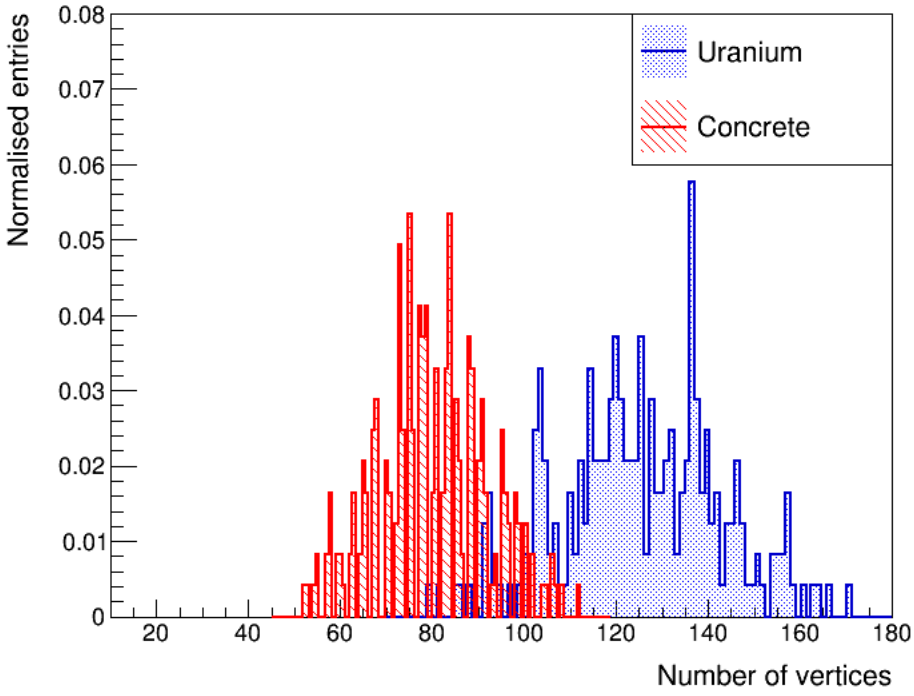

Figure 7.5: Comparison of distributions of the number of scattering vertices inside 10 cm cubes of uranium in blue, and inside equally-sized concrete matrix in red. Higher number of vertices corresponding to the vertices within the uranium cube.

Bibliography

[1] R. F. Mould. "The early history of X-ray diagnosis with emphasis on the contributions of physics 1895-1915". In: *Physics in Medicine & Biology* 40.11 (1995), p. 1741. DOI: 10.1088/0031-9155/40/11/001.

[2] K. Morishima et al. "Discovery of a big void in Khufu's Pyramid by observation of cosmic-ray muons". In: *Nature (London)* 552.7685 (2017), pp. 386–390. DOI: 10.1038/nature24647. arXiv: 1711.01576.

[3] H. K. M. Tanaka et al. "Development of a portable assembly-type cosmic-ray muon module for measuring the density structure of a column of magma". In: *Earth, Planets and Space* 62.2 (2010), pp. 119–129. DOI: 10.5047/EPS.2009.06.003.

[4] W. C. Priedhorsky, K. N. Borozdin, and G. E. Hogan. "Detection of high-Z objects using multiple scattering of cosmic ray muons ARTICLES YOU MAY BE INTERESTED IN". In: *Review of Scientific Instruments* 74 (2003), p. 4294. DOI: 10.1063/1.1606536.

[5] S. Pesente et al. "First results on material identification and imaging with a large-volume muon tomography prototype". In: *Nuclear Instruments and Methods in Physics Research, Section A: Accelerators, Spectrometers, Detectors and Associated Equipment* 604.3 (2009), pp. 738–746. DOI: 10.1016/J.NIMA.2009.03.017.

[6] A. Bettini. "Introduction to Elementary Particle Physics". In: *Introduction to Elementary Particle Physics* (2008), pp. 1–431. DOI: 10.1017/CBO9780511809019.

[7] C. Patrignani et al. "Review of Particle Physics". In: *Chinese Physics C* 40.10 (2016), p. 100001. DOI: 10.1088/1674-1137/40/10/100001.

[8] T. K. Gaisser, Ralph Engel, and Elisa Resconi. "Cosmic rays and particle physics". In: *Cosmic Rays and Particle Physics* (2016), pp. 1–444. DOI: 10.1017/CBO9781139192194.

[9] H. Jokisch et al. "Cosmic-ray muon spectrum up to 1 TeV at 75° zenith angle". In: *Physical Review D* 19.5 (1979), p. 1368. DOI: 10.1103/PhysRevD.19.1368.

[10] M. P. De Pascale et al. "Absolute spectrum and charge ratio of cosmic ray muons in the energy region from 0.2 GeV to 100 GeV at 600 m above sea level". In: *Journal of Geophysical Research: Space Physics* 98.A3 (1993), pp. 3501–3507. DOI: 10.1029/92JA02672.

[11] O. C. Allkofer, K. Carstensen, and W. D. Dau. "The absolute cosmic ray muon spectrum at sea level". In: *Physics Letters B* 36.4 (1971), pp. 425–427. DOI: 10.1016/0370-2693(71)90741-6.

[12] B. C. Rastin. "An accurate measurement of the sea-level muon spectrum within the range 4 to 3000 GeV/c". In: *Journal of Physics G: Nuclear Physics* 10.11 (1984), pp. 1609–1628. DOI: 10.1088/0305-4616/10/11/017.

[13] C. A. Ayre et al. "Precise measurement of the vertical muon spectrum in the range 20-500 GeV/c". In: *Journal of Physics G: Nuclear Physics* 1.5 (1975), p. 584. DOI: 10.1088/0305-4616/1/5/010.

[14] J. Kremer et al. "Measurements of Ground-Level Muons at Two Geomagnetic Locations" (1999).

[15] S. Haino et al. "Measurements of primary and atmospheric cosmic-ray spectra with the BESS-TeV spectrometer". In: *Physics Letters B* 594.1-2 (2004), pp. 35–46. DOI: 10.1016/J.PHYSLETB.2004.05.019. arXiv: 0403704 [astro-ph].

[16] P. Achard et al. "Measurement of the atmospheric muon spectrum from 20 to 3000 GeV". In: *Physics Letters B* 598.1-2 (2004), pp. 15–32. DOI: 10.1016/J.PHYSLETB.2004.08.003.

[17] P. H. Barrett et al. "Interpretation of cosmic-ray measurements far underground". In: *Reviews of Modern Physics* 24.3 (1952), pp. 133–178. DOI: 10.1103/REVMODPHYS.24.133.

[18] P. A. Zyla et al. "Review of Particle Physics". In: *Progress of Theoretical and Experimental Physics* 2020.8 (2020), pp. 1–2093. DOI: 10.1093/PTEP/PTAA104. URL: https://academic.oup.com/ptep/article/2020/8/083C01/5891211.

[19] E. P. George. "Cosmic rays measure overburden of tunnel". In: *Commonwealth Engineering* (1952), p. 455.

[20] L. W. Alvarez et al. "Search for hidden chambers in the pyramids". In: *Science* 167.3919 (1970), pp. 832–839. DOI: 10.1126/science.167.3919.832.

[21] K. N. Borozdin et al. "Radiographic imaging with cosmic-ray muons". In: *Nature* 422.6929 (2003), p. 277. DOI: 10.1038/422277A.

[22] S. Royan. "Oxford Handbook of Medical Imaging". In: *The British Journal of Radiology* 85.1018 (2012), e959–e959. DOI: 10.1259/BJR/91742999.

[23] H. K. M. Tanaka, Taro Kusagaya, and Hiroshi Shinohara. "Radiographic visualization of magma dynamics in an erupting volcano". In: *Nature communications* 5.1 (2014), pp. 3381–3381. DOI: 10.1038/ncomms4381.

[24] V. L. Highland. "Some practical remarks on multiple scattering". In: *Nuclear Instruments and Methods* 129.2 (1975), pp. 497–499. DOI: 10.1016/0029-554X(75)90743-0.

[25] G. R. Lynch and O. I. Dahl. "Approximations to multiple Coulomb scattering". In: *Nuclear Inst. and Methods in Physics Research, B* 58.1 (1991), pp. 6–10. DOI: 10.1016/0168-583X(91)95671-Y.

[26] *Particle Data Group. Atomic and nuclear properties of materials.* URL: https://pdg.lbl.gov/2020/AtomicNuclearProperties/index.html.

[27] E. Caffau, F. Coren, and G. Giannini. "Underground cosmic-ray measurement for morphological reconstruction of the "Grotta Gigante" natural cave". In: *Nuclear Instruments and Methods in Physics Research, Section A: Accelerators, Spectrometers, Detectors and Associated Equipment* 385.3 (1997), pp. 480–488. DOI: 10.1016/S0168-9002(96)01041-8.

[28] H. K. M. Tanaka et al. "Development of an emulsion imaging system for cosmic-ray muon radiography to explore the internal structure of a volcano, Mt. Asama". In: *Nuclear Instruments and Methods in Physics Research, Section A: Accelerators, Spectrometers, Detectors and Associated Equipment* 575.3 (2007), pp. 489–497. DOI: 10.1016/J.NIMA.2007.02.104.

[29] H. K. M. Tanaka and Izumi Yokoyama. "Muon radiography and deformation analysis of the lava dome formed by the 1944 eruption of Usu, Hokkaido —Contact between high-energy physics and volcano physics". In: *Proceedings of the Japan Academy. Series B. Physical and biological sciences* 84.4 (2008), pp. 107–116. DOI: 10.2183/pjab.84.107.

[30] H. K. M. Tanaka et al. "High resolution imaging in the inhomogeneous crust with cosmic-ray muon radiography: The density structure below the volcanic crater floor of Mt. Asama, Japan". In: *Earth and Planetary Science Letters* 263.1-2 (2007), pp. 104–113. DOI: 10.1016/J.EPSL.2007.09.001.

[31] J. Marteau et al. "DIAPHANE: Muon tomography applied to volcanoes, civil engineering, archaelogy". In: *Journal of Instrumentation* 12.2 (2017). DOI: 10.1088/1748-0221/12/02/C02008. arXiv: 1612.03905.

[32] S. Miyamoto et al. "A muographic study of a scoria cone from 11 directions using nuclear emulsion cloud chambers". In: *Geoscientific Instrumentation, Methods and Data Systems* 11.1 (2022), pp. 127–147. DOI: 10.5194/GI-11-127-2022.

[33] N. Lesparre et al. "Density muon radiography of La Soufrière of Guadeloupe volcano: Comparison with geological, electrical resistivity and gravity data". In: *Geophysical Journal International* 190.2 (2012), pp. 1008–1019. DOI: 10.1111/J.1365-246X.2012.05546.X.

[34] G. Gallo et al. "Three years of muography at Mount Etna: Results and perspectives". In: *Journal of Instrumentation* 17.2 (2022). DOI: 10.1088/1748-0221/17/02/C02003. arXiv: 2109.13125.

[35] S. Bouteille et al. “A Micromegas-based telescope for muon tomography: The WatTo experiment”. In: *Nuclear Instruments and Methods in Physics Research, Section A: Accelerators, Spectrometers, Detectors and Associated Equipment* 834 (2016), pp. 223–228. DOI: 10.1016/J.NIMA.2016.08.002.

[36] G. Baccani et al. “Muon radiography of ancient mines: The San silvestro archaeomining park (Campiglia marittima, Tuscany)”. In: *Universe* 5.1 (2019). DOI: 10.3390/UNIVERSE5010034.

[37] J. Gluyas et al. “Passive, continuous monitoring of carbon dioxide geostorage using muon tomography”. In: *Philosophical Transactions of the Royal Society A: Mathematical, Physical and Engineering Sciences* 377.2137 (2019). DOI: 10.1098/RSTA.2018.0059.

[38] L. F. Thompson et al. “Muon tomography for railway tunnel imaging”. In: *Physical Review Research* 2.2 (2020). DOI: 10.1103/PHYSREVRESEARCH.2.023017.

[39] IAEA. *Non-Proliferation of Nuclear Weapons and Nuclear Security*. 2011. URL: https://www.iaea.org/sites/default/files/safeguards0806.pdf.

[40] T. B. Blackwell and V. A. Kudryavtsev. “Development of a 3D muon disappearance algorithm for muon scattering tomography”. In: *Journal of Instrumentation* 10.5 (2015). DOI: 10.1088/1748-0221/10/05/T05006.

[41] A. Erlandson et al. “An analysis of pressurized heavy water reactor fuel for nuclear safeguards applications using muon scattering tomography”. In: *Journal of Instrumentation* 16.2 (2021). DOI: 10.1088/1748-0221/16/02/P02024.

[42] J. Bae and Stylianos Chatzidakis. “Momentum-Dependent Cosmic Ray Muon Computed Tomography Using a Fieldable Muon Spectrometer”. In: *Energies* 15.7 (2022), p. 2666. DOI: 10.3390/EN15072666.

[43] C. L. Morris et al. “Tomographic imaging with cosmic ray muons”. In: *Science and Global Security* 16.1-2 (2008), pp. 37–53. DOI: 10.1080/08929880802335758.

[44] L. J. Schultz et al. “Statistical Reconstruction for Cosmic Ray Muon Tomography”. In: *IEEE transactions on image processing* 16.8 (2007), pp. 1985–1993. DOI: 10.1109/TIP.2007.901239.

[45] F. Riggi et al. “The Muon Portal Project: Commissioning of the full detector and first results”. In: *Nuclear Instruments and Methods in Physics Research, Section A: Accelerators, Spectrometers, Detectors and Associated Equipment* 912 (2018), pp. 16–19. DOI: 10.1016/J.NIMA.2017.10.006.

[46] S. Laureti et al. “Detection of rebars in concrete using advanced ultrasonic pulse compression techniques”. In: *Ultrasonics* 85 (2018), pp. 31–38. DOI: 10.1016/j.ultras.2017.12.010.

[47] J. H. Bungey. “Sub-surface radar testing of concrete: A review”. In: *Construction and Building Materials* 18.1 (2004), pp. 1–8. DOI: 10.1016/S0950-0618(03)00093-X.

[48] M. Dobrowolska et al. “Towards an application of muon scattering tomography as a technique for detecting rebars in concrete”. In: *Smart Materials and Structures* 29.5 (2020). DOI: 10.1088/1361-665X/AB7A3F.

[49] S. Tripathy et al. “Numerical evaluation of a muon tomography system for imaging defects in concrete structures”. In: *European Physical Journal Plus* 136.8 (2021). DOI: 10.1140/EPJP/S13360-021-01809-X. arXiv: 2102.08913.

[50] IAEA. “Classification of Radioactive Waste”. In: *IAEA Safety Standards* No. GSG-1 (2009). URL: https://www-pub.iaea.org/MTCD/Publications/PDF/Pub1419_web.pdf.

[51] IAEA. “Interim Storage of Radioactive Waste Packages”. In: *TECHNICAL REPORTS SERIES* No. 390 (1998). URL: https://www-pub.iaea.org/MTCD/publications/PDF/TRS390_scr.pdf.

[52] IAEA. “IAEA”. In: *Storage of Spent Nuclear Fuel for protecting people and the environment* IAEA.SSG-15 (2012). URL: http://www-ns.iaea.org/standards/.

[53] J. Skrzyppek and J. D. Kim. “A Well Established System For The Dry Storage Of Spent Fuel”. In: *Transactions of the Korean Nuclear Society Spring Meeting Jeju* (2015). URL: https://www.kns.org/files/pre_paper/33/15S-134JuergenSkrzyppek.pdf.

[54] IAEA. *Retrieval and Conditioning of Solid Radioactive Waste from Old Facilities*. 2007. URL: https://www-pub.iaea.org/MTCD/Publications/PDF/TRS456_web.pdf.

[55] IAEA. *Strategy and Methodology for Radioactive Waste Characterization*. 2007. URL: https://www-pub.iaea.org/MTCD/publications/PDF/te_1537_web.pdf.

[56] N. Estre et al. “High-Energy X-Ray Imaging Applied to Nondestructive Characterization of Large Nuclear Waste Drums”. In: *IEEE Transactions on Nuclear Science* 62.6 (2015), pp. 3104–3109. DOI: 10.1109/TNS.2015.2498190.

[57] D. Mahon et al. “First-of-a-kind muography for nuclear waste characterization”. In: *Philosophical transactions of the Royal Society of London. Series A: Mathematical, physical, and engineering sciences* 377.2137 (2018), pp. 20180048–. DOI: 10.1098/rsta.2018.0048.

[58] C. Thomay et al. “Passive 3D imaging of nuclear waste containers with Muon Scattering Tomography”. In: *Journal of Instrumentation* 11.3 (2016). DOI: 10.1088/1748-0221/11/03/P03008.

[59] A. Danon, J. E. Koresh, and M. H. Mintz. “Temperature programmed desorption characterization of oxidized uranium surfaces: relation to some gas-uranium reactions”. In: *Langmuir* 15.18 (1999), pp. 5913–5920. DOI: 10.1021/LA981210G.

[60] M. Dobrowolska et al. “A novel technique for finding gas bubbles in the nuclear waste containers using Muon Scattering Tomography”. In: *Journal of Instrumentation* 13.5 (2018). DOI: 10.1088/1748-0221/13/05/P05015.

[61] CHANCE. *Characterization of conditioned radioactive waste.* URL: https://www.chance-h2020.eu/.

[62] J. Burns et al. “A drift chamber tracking system for muon scattering tomography applications”. In: *Journal of Instrumentation* 10.10 (2015). DOI: 10.1088/1748-0221/10/10/P10041.

[63] P. Baesso et al. “A high resolution resistive plate chamber tracking system developed for cosmic ray muon tomography”. In: *Journal of Instrumentation* 8.8 (2013). DOI: 10.1088/1748-0221/8/08/P08006.

[64] C. Steer, P. Stowell, and L.F. Thompson. *CRESTA:Cosmic rays for engineering, scientific, and technology applications.* URL: https://gitlab.com/cosmicraysim/cresta.

[65] S. Agostinelli et al. “Geant4—a simulation toolkit”. In: *Nuclear Instruments and Methods in Physics Research Section A: Accelerators, Spectrometers, Detectors and Associated Equipment* 506.3 (2003), pp. 250–303. DOI: 10.1016/S0168-9002(03)01368-8.

[66] C. Hagmann, D. Lange, and D. Wright. “Cosmic-ray shower generator (CRY) for Monte Carlo transport codes”. In: *IEEE Nuclear Science Symposium Conference Record* 2 (2007), pp. 1143–1146. DOI: 10.1109/NSSMIC.2007.4437209.

[67] L. S. Waters et al. “The MCNPX Monte Carlo radiation transport code”. In: *AIP Conference Proceedings* 896 (2007), pp. 81–90. DOI: 10.1063/1.2720459.

[68] R. Brun and F. Rademakers. “ROOT - An object oriented data analysis framework”. In: *Nuclear Instruments and Methods in Physics Research, Section A: Accelerators, Spectrometers, Detectors and Associated Equipment* 389.1-2 (1997), pp. 81–86. DOI: 10.1016/S0168-9002(97)00048-X.

[69] C. Thomay et al. “A binned clustering algorithm to detect high-Z material using cosmic muons”. In: *Journal of Instrumentation* 8.10 (2013). DOI: 10.1088/1748-0221/8/10/P10013.

[70] J. Bae and S. Chatzidakis. “Fieldable Muon Momentum Measurement using Coupled Pressurized Gaseous Cherenkov Detectors” (2022). DOI: 10.13182/T125-36581. arXiv: 2201.02591. URL: https://arxiv.org/abs/2201.02591v1.

[71] L. J. Schultz et al. “Image reconstruction and material Z discrimination via cosmic ray muon radiography”. In: *Nuclear Instruments and Methods in Physics Research, Section A: Accelerators, Spectrometers, Detectors and Associated Equipment* 519.3 (2004), pp. 687–694. DOI: 10.1016/J.NIMA.2003.11.035.

[72] J. L. Prince and J. M. Links. “Medical Imaging Signals and Systems, Second Edition”. In: *Upper Saddle River, New Jersey : Prentice Hall* 2 (2014).

[73] S. Riggi et al. “Muon tomography imaging algorithms for nuclear threat detection inside large volume containers with the Muon Portal detector”. In: *Nuclear Instruments and Methods in Physics Research, Section A: Accelerators, Spectrometers, Detectors and Associated Equipment* 728 (2013), pp. 59–68. DOI: 10.1016/J.NIMA.2013.06.040. arXiv: 1307.0714.

[74] M. Stapleton et al. “Angle Statistics Reconstruction: A robust reconstruction algorithm for Muon Scattering Tomography”. In: *Journal of Instrumentation* 9.11 (2014). DOI: 10.1088/1748-0221/9/11/P11019.

[75] A. Hoecker et al. “TMVA - Toolkit for Multivariate Data Analysis” (2007). arXiv: physics/0703039 [physics.data-an].

[76] L. Frazão et al. “Discrimination of high-Z materials in concrete-filled containers using muon scattering tomography”. In: *Journal of Instrumentation* 11.7 (2016). DOI: 10.1088/1748-0221/11/07/P07020.

[77] M. J. Weekes et al. “Material identification in nuclear waste drums using muon scattering tomography and multivariate analysis”. In: *Journal of Instrumentation* 16.5 (2021). DOI: 10.1088/1748-0221/16/05/P05007. arXiv: 2012.01554.

[78] J. A. Hanley and B. J. McNeil. “The meaning and use of the area under a receiver operating characteristic (ROC) curve.” In: *Radiology* 143.1 (1982), pp. 29–36. DOI: 10.1148/radiology.143.1.7063747.

[79] W. J. Youden. “INDEX FOR RATING DIAGNOSTIC TESTS”. In: *Cancer* 3.1 (1950), pp. 32–35. DOI: 10.1002/1097-0142.